



National Library
of Canada

Bibliothèque nationale
du Canada

Acquisitions and
Bibliographic Services Branch

Direction des acquisitions et
des services bibliographiques

395 Wellington Street
Ottawa, Ontario
K1A 0N4

395, rue Wellington
Ottawa (Ontario)
K1A 0N4

Your file *Votre référence*

Our file *Notre référence*

NOTICE

The quality of this microform is heavily dependent upon the quality of the original thesis submitted for microfilming. Every effort has been made to ensure the highest quality of reproduction possible.

If pages are missing, contact the university which granted the degree.

Some pages may have indistinct print especially if the original pages were typed with a poor typewriter ribbon or if the university sent us an inferior photocopy.

Reproduction in full or in part of this microform is governed by the Canadian Copyright Act, R.S.C. 1970, c. C-30, and subsequent amendments.

AVIS

La qualité de cette microforme dépend grandement de la qualité de la thèse soumise au microfilmage. Nous avons tout fait pour assurer une qualité supérieure de reproduction.

S'il manque des pages, veuillez communiquer avec l'université qui a conféré le grade.

La qualité d'impression de certaines pages peut laisser à désirer, surtout si les pages originales ont été dactylographiées à l'aide d'un ruban usé ou si l'université nous a fait parvenir une photocopie de qualité inférieure.

La reproduction, même partielle, de cette microforme est soumise à la Loi canadienne sur le droit d'auteur, SRC 1970, c. C-30, et ses amendements subséquents.

**PRECIPITATION BEHAVIOUR OF IF 409
FERRITIC STAINLESS STEELS**

by

Robert Moses

A Thesis Submitted to the Faculty of Graduate Studies and
Research in Partial Fulfillment of the Requirements
for the Degree of Master of Engineering

Department of Mining and Metallurgical Engineering
McGill University
Montreal, Canada

August 1994

©



National Library
of Canada

Acquisitions and
Bibliographic Services Branch

395 Wellington Street
Ottawa, Ontario
K1A 0N4

Bibliothèque nationale
du Canada

Direction des acquisitions et
des services bibliographiques

395, rue Wellington
Ottawa (Ontario)
K1A 0N4

Your file *Votre référence*

Our file *Notre référence*

THE AUTHOR HAS GRANTED AN IRREVOCABLE NON-EXCLUSIVE LICENCE ALLOWING THE NATIONAL LIBRARY OF CANADA TO REPRODUCE, LOAN, DISTRIBUTE OR SELL COPIES OF HIS/HER THESIS BY ANY MEANS AND IN ANY FORM OR FORMAT, MAKING THIS THESIS AVAILABLE TO INTERESTED PERSONS.

L'AUTEUR A ACCORDE UNE LICENCE IRREVOCABLE ET NON EXCLUSIVE PERMETTANT A LA BIBLIOTHEQUE NATIONALE DU CANADA DE REPRODUIRE, PRETER, DISTRIBUER OU VENDRE DES COPIES DE SA THESE DE QUELQUE MANIERE ET SOUS QUELQUE FORME QUE CE SOIT POUR METTRE DES EXEMPLAIRES DE CETTE THESE A LA DISPOSITION DES PERSONNE INTERESSEES.

THE AUTHOR RETAINS OWNERSHIP OF THE COPYRIGHT IN HIS/HER THESIS. NEITHER THE THESIS NOR SUBSTANTIAL EXTRACTS FROM IT MAY BE PRINTED OR OTHERWISE REPRODUCED WITHOUT HIS/HER PERMISSION.

L'AUTEUR CONSERVE LA PROPRIETE DU DROIT D'AUTEUR QUI PROTEGE SA THESE. NI LA THESE NI DES EXTRAITS SUBSTANTIELS DE CELLE-CI NE DOIVENT ETRE IMPRIMES OU AUTREMENT REPRODUITS SANS SON AUTORISATION.

ISBN 0-612-05464-0

Canada

To my love, Christina

ABSTRACT

Five slightly different IF 409 ferritic stainless steels were investigated by means of continuous cooling compression (CCC) testing. These compression test were performed at a constant strain rate of $1.8 \times 10^{-4} \text{ s}^{-1}$ over a 600°C temperature range (i.e. from 1200°C-600°C) at four different cooling rates (0.25, 0.5, 1.0 and 2.0°C/sec). The reheating temperature and time were varied and the effect of this on precipitation is discussed.

The analysis of the CCC test results, and the optical microscopy observations, indicated that neither solute drag nor phase transformation is responsible for the deviations observed in these flow curves. TEM bright field images were used to verify the presence of precipitates, and to calculate the strengthening influence of these particles on the flow curve. It is shown that, in the niobium bearing materials, the precipitation of carbonitrides is responsible for the increase in flow stress. Conversely, in the titanium bearing materials, the titanium carbonitride precipitates were determined to have no effect on the flow stress.

It was discovered that increasing the solution temperature and time resulted in the occurrence of precipitation at higher temperatures, and that these precipitates were coarsened to a greater extent. Also, when the holding temperature and/or the holding time was decreased, the amount of niobium put into solution decreased, which led to precipitation starting at lower temperatures.

A method was developed for determining the precipitation start and finish temperatures from the CCC results. These temperatures were converted to precipitation start and finish times for each of the four cooling rates. This revealed that the precipitation start and finish times increase with decreasing cooling rate in both the 0.2% Nb and 0.1% Nb + 0.1% Ti stainless steels. Finally, a continuous cooling precipitation diagram was constructed for the two niobium bearing materials using these start and finish times.

RESUME

Cinq aciers inoxydables ferritiques IF 409 différents ont été étudiés en utilisant des tests de compression en refroidissement continu. Ces tests de compression ont été faits à un taux de déformation constant de 1.8×10^{-4} à des températures supérieures à 600°C (1200°C à 600°C) à quatre taux de refroidissement (0.25, 0.5, 1.0 et 2.0°C/sec). La température et le temps de rechauffement ont été variés et leurs effets sur la précipitation ont été discutés.

L'analyse des résultats des tests de compression en refroidissement continu et des observations microscopiques ont indiqué que ni la traînée des solutés ni la transformation de phase ne sont responsables de la déviation observée sur les courbes d'écoulement. Les champs brillants des images de microscopie électronique à transmission ont été utilisés pour vérifier la présence de précipités et pour calculer l'influence de ces particules sur les courbes d'écoulement. Il a été démontré que, dans les matériaux contenant du niobium, la précipitation de ces nitrocarbures est responsable de l'augmentation de la contrainte d'écoulement. À l'opposé, il a été montré que, dans les matériaux contenant du titane, les précipités de nitrocarbures de titane n'ont aucun effet sur la contrainte d'écoulement.

Il a été découvert que l'augmentation du temps et de la température de mise en solution résulte en une précipitation à des températures plus élevées et au grossissement des précipités à des niveaux plus étendus. Aussi, quand la température de maintien et/ou le temps de maintien ont été réduits, la quantité de niobium mise en solution a diminué, ce qui a conduit à une précipitation à des températures plus basses.

Une méthode a été développée pour déterminer les températures de début et de fin de la précipitation à partir des résultats des courbes de compression en refroidissement continu. Ces températures ont été converties aux temps de début et de fin de la précipitation pour chacun des quatre taux de refroidissement. Ceci a révélé que les temps de début et de fin

de précipitation croissent avec l'augmentation du taux de refroidissement des alliages d'aciers inoxydables 0.2% Nb et 0.1% Nb + 0.1% Ti. Finalement, un diagramme de précipitation en refroidissement continue a été construit pour les deux matériaux contenant du niobium en utilisant les temps de début et de fin de précipitation.

ACKNOWLEDGMENTS

The author would like to express his sincere gratitude to his thesis supervisors, Professor J.J. Jonas and Professor S. Yue. The successful completion of this work is due to their guidance, constant encouragement, and stimulating discussions throughout the course of this research.

The author is deeply grateful to Bombardier Inc. and the Fonds pour la Formation de Chercheurs et l'Aide à la Recherche (Fonds FCAR) for their scholarship awards.

Special thanks are due to Dr. A. Zarei Hanzaki for his encouragement and advice, and Mr. Edwin Fernandez who, not only prepared specimens but was also greatly responsible for the excellent atmosphere prevailing in the group.

I am grateful to Lorraine Mello for her administrative and office assistance.

I would like to thank my fellow graduate students and friends, as well as the research associates and professors with whom I had the pleasure to work; special mention is made here of my good friend Gail Stephen.

Last, but not least, the love and encouragement of my fiancée Christina, my parents, and my brother and sisters are extremely appreciated.

TABLE OF CONTENTS

	Page
ABSTRACT	i
RESUME	ii
ACKNOWLEDGMENTS	iv
TABLE OF CONTENTS	v
LIST OF FIGURES	viii
LIST OF TABLES	xii
CHAPTER I	
INTRODUCTION	1
CHAPTER II	
LITERATURE REVIEW	3
<u>II. 1. History of the development of ferritic stainless steels</u>	3
<u>II. 2. Stainless steel metallurgy</u>	4
II. 2.1. Effects of carbon and nitrogen	7
<u>II. 3. Embrittling phenomena in ferritic stainless steels</u>	12
II. 3.1. Sigma phase	12
II. 3.2. 475°C embrittlement	15
II. 3.3. High temperature embrittlement and loss of corrosion resistance	17
<u>II. 4. Effects of microalloying elements</u>	19
II. 4.1. Titanium	19
II. 4.2. Niobium	20
II. 4.3. Molybdenum	24
<u>II. 5. Precipitation</u>	24
II. 5.1. Nucleation and growth	27
II. 5.1.1. Homogeneous nucleation	27
II. 5.1.2. Heterogeneous nucleation	28

II. 5.2. Ostwald ripening	31
II. 5.3. Static precipitation	34
II. 5.4. Strain induced precipitation	34
II. 5.5. Dynamic precipitation	35
<u>II. 6. Continuous cooling precipitation (CCP) diagrams</u>	36
II. 6.1. Current methods of predicting P_s times during isothermal holding	36
II. 6.2. Current method of predicting P_f times during isothermal holding	37
II. 6.3. Current method of modeling CCP diagrams based on P_s and P_f times	38

CHAPTER III

EXPERIMENTAL PROCEDURE	43
<u>III. 1. Stainless steel compositions</u>	43
<u>III. 2. Specimen preparation.</u>	43
<u>III. 3. Mechanical testing equipment</u>	44
III. 3.1. MTS automated testing equipment	44
III. 3.2. Load frame and hydraulic power supply	44
III. 3.3. Closed loop and outer loop system	44
III. 3.4. Furnace, temperature controller/programmer, and compression tools	46
<u>III. 4. Continuous cooling compression testing</u>	51
III. 4.1. Heating and deformation schedules	51
III. 4.2. Determination of tool length contraction	52
<u>III. 5. Micro and submicro-structural analysis</u>	52
III. 5.1. Metallography	52
III. 5.2. Thin foil preparation	56
III. 5.3. Transmission electron microscopy (TEM)	56

CHAPTER IV

RESULTS	57
<u>IV. 1. Anvil contraction</u>	57
IV. 1.1. Effect on strain and strain rate	57
IV. 1.2. Alumina correction	59

<u>IV. 2. Continuous cooling curves</u>	62
IV. 2.1. General interpretation	62
IV. 2.2. Standard schedule (an overview)	63
IV. 2.2.1. Calibration	69
IV. 2.3. High temperature solutionizing schedule	72
IV. 2.3.1. IF Nb stabilized	72
IV. 2.3.2. IF Ti stabilized	72
IV. 2.4. Low temperature and reduced time solutionizing schedule	75
IV. 2.4.1. IF Nb stabilized	75
CHAPTER V	
DISCUSSION	77
<u>V. 1. Solute drag</u>	77
<u>V. 2. Phase transformations</u>	81
<u>V. 3. Precipitation effects</u>	82
<u>V. 4. TEM examination</u>	85
V. 4.1. Thin foils	85
V. 4.2. Estimation of precipitation strengthening	86
<u>V. 5. Continuous Cooling Precipitation (CCP) Curves</u>	89
V. 5.1. P_s and P_f determination	89
V. 5.2. Varying cooling rate schedule for the Nb bearing stainless steels	90
CHAPTER VI	
CONCLUSIONS	100
REFERENCES	102

LIST OF FIGURES

Figure		Page
II-1	Iron-chromium phase diagram	5
II-2	Iron loop of iron-chromium phase diagram for alloys with 0.004% carbon and 0.002% nitrogen.	8
II-3	Shifting of the boundary line ($\gamma + \alpha$)/ α in the system iron-chromium through increasing additions of carbon and nitrogen.	9
II-4	Effects of nickel content on the stability of austenite in an iron alloy containing 18% chromium.	11
II-5	Compositions of iron-chromium-nickel alloys for which austenite persists at room temperature. Point P indicates the position of an alloy containing 18% chromium and 8% nickel.	11
II-6	Relative hardening of ferritic and martensitic iron-chromium alloys after water quenching from indicated temperatures.	13
II-7	Temperature versus time diagram outlining embrittlement conditions.	14
II-8	Iron-chromium phase diagram in binary high purity 25 to 76% chromium alloys.	16
II-9	Phase diagram of the iron-chromium system according to Williams [22].	18
II-10	Effects of carbon and nitrogen level and chromium content on as-welded ductility and intergranular corrosion resistance of chromium-iron ferritic stainless steels. Comparison to Binder's [36] limit for impact resistance of annealed specimens.	21
II-11	Transition temperatures for quarter-size Charpy V-notch specimens of air-melted commercial-purity 18Cr-2Mo steel water quenched from 1150°C (sensitized) and 815°C (annealed) as a function of titanium or niobium content.	23
II-12	Effects of molybdenum addition on impact transition temperature of annealed 25Cr-Fe stainless steels (a) vacuum melted and (b) air-melted. Quarter-size Charpy V-notch impact specimens.	25
II-13	Effect of weld ductilization additives on as-welded ductility and corrosion resistance of high chromium-iron stainless steels; additives, singly or in combination, include aluminum, copper, vanadium, platinum, palladium, and silver in a range 0.1 to 1.3%.	26

- List of figures -

II-14	Free energy of a precipitate particle as a function of its radius.	30
II-15	Model for heterogeneous nucleation on a flat surface; (a) cross-section through spherical cap; and (b) energy balance at the solid-liquid-surface junction [59].	30
II-16	Growth of precipitate particle. Small arrows at surfaces of particles indicate the net direction of the flow of solute atoms [58].	33
II-17	A diagrammatic representation of the additivity rule concept.	40
II-18	Calculated CCP behaviour from PTT data [86].	42
III-1	Compression specimen geometry and groove design.	45
III-2	An exterior view of the equipment setup: A) MTS load frame; B) MTS electronics; C) VT-240 graphics terminal and LA-50 printer; D) radiant furnace and compression tools; E) temperature controller/programmer; and F) argon gas supply.	45
III-3	Closed loop servohydraulic system.	47
III-4	Computerized outer loop system.	48
III-5	View of the radiant furnace and experimental setup: 1) radiant furnace; 2) Inconel anvils; 3) actuator; 4) load cell; 5) temperature controller, 6) quenching can.	49
III-6	Schematic drawing of the MTS load train.	50
III-7	Heating and deformation schedule for 1200°C CCC tests.	53
III-8	Heating and deformation schedule for 1300°C CCC tests.	53
III-9	Heating and deformation schedule for 1200, 1000 and 950°C CCC tests.	54
III-10	Heating and deformation schedule for CCC tests at a series of cooling rates.	54
III-11	Anvil contraction versus temperature for cooling rates of 0.25, 0.5, 1 and 2°C/sec.	55
IV-1	Standard stress-temperature behaviour expected in the absence of mechanism change for the CCC tests.	64
IV-2a	Superposition of the expected curve on the actual behaviour of the 0.2% Nb stainless steel.	65

- List of figures -

IV-2b	Superposition of the expected curve on the actual behaviour of the 0.2% Nb stainless steel; with the starting flow stress of the steady state flow curve corrected to match that of the actual test.	66
IV-3	True stress vs. temperature for all five steels, 1200-900°C ($\dot{\epsilon}=3 \times 10^{-4}$).	67
IV-4	True stress vs. temperature for all five steels, 1000-600°C ($\dot{\epsilon}=3 \times 10^{-4}$).	68
IV-5	True stress vs. temperature for all five steels, 1000-600°C ($\dot{\epsilon}=1.8 \times 10^{-4}$), taking contraction effects into account.	70
IV-6	Superposition of the expected curve on the actual behaviour of the 0.1% Nb + 0.1% Ti stainless steel; with the starting flow stress of the steady state flow curve corrected to match that of the actual test.	71
IV-7	True stress vs. temperature for the 0.2% Nb material after holding at different temperatures and times.	73
IV-8	True stress vs. temperature for the IF Ti stabilized material after holding at different temperatures and times compared to the standard curve.	74
IV-9	True stress vs. temperature for the 0.2% Nb material after holding at different temperatures and times.	76
V-1	Drag force vs. velocity profiles for various elements in γ -iron [100].	79
V-2	True stress vs. temperature for the 0.2% Nb, 0.1% Nb + 0.1% Ti, and 0.2% Ti steels, 1200-600°C ($\dot{\epsilon}=1.8 \times 10^{-4}$).	80
V-3	Microstructure of the 0.2% Nb material after a strain of 0.112 (100X).	83
V-4	Microstructure of the 0.2% Nb material after a strain of 0.135 (100X).	83
V-5	Microstructure of the 0.2% Nb material after a strain of 0.150 (100X).	84
V-6	Microstructure of the 0.2% Nb material after a strain of 0.185 (100X).	84
V-7	Bright field image of precipitates in the 0.2% Nb material, quenched at 920°C (100,000 X).	87
V-8	Bright field image of precipitates in the 0.2% Ti material, quenched at 920°C (100,000 X).	87
V-9	Log of true stress vs. temperature for the 0.2% Nb stainless steel, with the P_s and P_f temperatures indicated by the present selection criterion (1200°C-600°C, $\dot{\epsilon}=1.8 \times 10^{-4}$).	91

- List of figures -

- V-10 True stress vs. temperature for the 0.2% Nb material with the P_s and P_f temperatures determined from Figure V-9. 92
- V-11 True stress vs. temperature curves for the 0.2% Nb steel determined using different cooling rates (for 0.25 & 0.5°C/sec, $\dot{\epsilon} = 3 \times 10^{-4}$; for 1 & 2°C/sec, $\dot{\epsilon} = 6 \times 10^{-4}$). Note: after correcting for contraction, all strain rates were approximately $1.8 \times 10^{-4} \text{ s}^{-1}$. 93
- V-12 True stress vs. temperature curves for the 0.1% Nb + 0.1% Ti steel determined using different cooling rates (for 0.25 & 0.5°C/sec, $\dot{\epsilon} = 3 \times 10^{-4} \text{ s}^{-1}$ for 1 & 2°C/sec, $\dot{\epsilon} = 6 \times 10^{-4} \text{ s}^{-1}$). Note: after correcting for contraction, all strain rates were approximately $1.8 \times 10^{-4} \text{ s}^{-1}$. 94
- V-13 CCP curves for the 0.2% Nb and 0.1% Nb + 0.1% Ti stainless steels. 99

LIST OF TABLES

Table		Page
II-1	Solubilities of carbon and nitrogen in α - and γ -iron	10
II-2	Effect of stabilizer additions on the tensile ductility of annealed versus welded specimens containing 18% chromium-2% molybdenum.	22
II-3	Effect of titanium on the as-welded bend ductility for ferritic stainless steels containing 26 to 30% chromium.	22
III-1	Chemical compositions of the steels tested (wt.%)	43
IV-1	Percent decrease in anvil contraction due to increase in cooling rate.	60
IV-2	Δa and ΔA for all the cooling rates.	60
V-1	Theoretical flow strength increase due to the presence of precipitates.	89
V-2	P_s and P_f temperatures and times, determined from the flow curves of the 0.2% Nb and 0.1% Nb + 0.1% Ti materials, at various cooling rates.	97
V-3	Corrected P_s and P_f times, used for the construction of CCP curves.	98

CHAPTER I

INTRODUCTION

Ferritic stainless steels contain Cr levels as low as 11% and no added Ni, thus making them less expensive than austenitic stainless steels. However, they have lower yield strengths and less desirable formability properties, so that they must be used in less demanding applications, such as exhaust systems and catalytic converters in cars and trucks, in the web section of disc brakes and for chemical equipment and vessel containment. Dynamic recrystallization could refine the grain size (without the use of additional alloying elements) thereby improving the fatigue, fracture and yield strength properties and also decreasing the cost of fabrication. Unfortunately, one of the major limitations associated with the processing of ferritic stainless steels is their general inability to undergo grain refinement by dynamic recrystallization. This is due to their high stacking fault energies, which typically favor dynamic softening solely by recovery processes. By contrast, austenitic stainless steels have low stacking fault energies and, therefore, soften by dynamic recrystallization. In order for ferritic stainless steels to undergo dynamic recrystallization during processing, the precipitation of carbonitrides must be avoided, as they can inhibit the nucleation and growth of new grains.

Previous research at McGill, on conventional interstitial free (IF) steels, demonstrated that strain accumulation during warm rolling in a tandem mill can lead to dynamic recrystallization (in the ferrite region) at relatively low finishing temperatures. The current work was initiated to examine the possibility that IF 409 ferritic stainless steels can also undergo dynamic recrystallization. Five different grades of IF 409 stainless were studied. One each was stabilized with either titanium or niobium, one was stabilized with both niobium and titanium, one was free of these stabilizing elements, and the fifth was titanium stabilized, with twice the carbon and nitrogen levels of the other four. Since dynamic recrystallization is retarded, or can even be prevented, by the occurrence of strain induced precipitation, the kinetics of precipitation in the ferrite phase

were of interest in these steels. Consequently, the focus of this work shifted to investigating the possibility of carbonitride precipitation. For this, continuous cooling compression (CCC) tests were used to search for the characteristic inflections or deviations in the flow curve, which are indicative of such precipitates. By using different cooling rates, it was possible to deduce approximate CCP (continuous-cooling-precipitation) curves from these tests. These curves can then be used in industry to improve the properties of these stainless steels.

In the pursuance of the above objectives, this thesis was divided into the following chapters:

Chapter II is a literature review of the pertinent information related to ferritic stainless steels, with emphasis placed on precipitation and on traditional methods used in the construction of CCP diagrams.

Chapter III describes the experimental method and equipment used to perform the CCC tests. Included in this chapter are the specimen preparation methods that were used for the microstructural and TEM evaluations.

Chapter IV sets forth the foundations for interpreting CCC curves. Most of the results are shown here, along with an evaluation of each curve.

Chapter V demonstrates that the flow curve behaviour is indicative of precipitation, by means of: 1) eliminating all other possibilities, 2) showing the actual precipitates found during the TEM examinations, and 3) evaluating the strengthening effect of these precipitates. This chapter also presents a new method for the determination of precipitation start and finish temperatures. From this, a CCP diagram is constructed, using the results from CCC tests that were performed at a series of different cooling rates.

Finally, in Chapter VI, the general conclusions are drawn from the work described herein.

CHAPTER II

LITERATURE REVIEW

II. 1. History of the development of ferritic stainless steels

During the period between 1900 and 1915, several metallurgical questions related to the behaviour of steels were resolved: the puzzling allotropy of iron; the major effects that carbon has on the properties of iron; and the natures of the transformation mechanisms [1]. In Europe, just before the start of World War 1, ferritic and austenitic stainless steels were developed. The first stainless steels used industrially were 17% Cr ferritic, 12 % Cr martensitic and 18Cr-8Ni austenitic grades. Modifications of these three basic chemistries were developed as production methods and fabrication techniques improved and as demand increased into diverse fields of applications. Austenitic stainlesses became increasingly more popular because they exhibit excellent fabricating properties, they are quite weldable and they have superior mechanical and corrosion resistant properties over a broad temperature range, as compared to ferritic and martensitic stainless steels [2]. Because of this, the ferritic and martensitic stainlesses acquired a more restricted field of application. Martensitic stainless steels contain 11 - 15% Cr, and therefore exhibit a lower corrosion resistance. However, they display a very useful combination of strength, ductility, and toughness, and are consequently used mainly for structural components in power plants, steam and gas turbines, in the petrochemical industry, and for surgical tools.

Ferritic stainless steels have properties between those of austenitic and martensitic stainlesses. They contain 11 - 30% Cr, and, with the addition of molybdenum, their corrosion resistance can reach equivalent levels to that of austenitic steels. Note that, as a rule of thumb, the corrosion and oxidation resistance of ferritic steels are directly related to their chromium content. Some of the ferritic steels, such as Type 446 and those with

aluminum and rare earths added, exhibit very good oxidation resistance. Even though these steels can have equivalent corrosion resistance and lower-cost alloying elements, they were surpassed by their austenitic counterparts. This is predominantly due to their lower formability and toughness, and reduced weldability [3]. However, these drawbacks are minimized in light gages and, as a result, ferritic stainless steels are used chiefly in light-gage sheet form applications, such as automotive exhaust systems, automotive trim, and in cooking utensils [1, 2]. Since the advent of OAD (oxygen decarburization) and VOD (vacuum decarburization), which can produce steels with less than 0.05% carbon and nitrogen combined, new ferritic stainless steels have been produced with improved toughness and weldability.

II. 2. Stainless steel metallurgy

Ferritic stainless steels are microstructurally simple. At room temperature, they consist of a substitutional solid solution of an iron-chromium alpha phase (α -ferrite), having a body-centered-cubic (bcc) crystal structure. Upon heating, and up to the melting point, they remain essentially ferritic. A typical iron-chromium phase diagram, as published by the American Society for Metals [3], is shown in Figure II-1. There are two very important features that are seen in this phase diagram. First is the gamma (γ) loop that is situated at the lower chromium end of the phase diagram at the region of intermediate temperatures. The second is the area in the center of the diagram that shows a pure sigma and a duplex sigma-alpha zone (this area will be discussed in the embrittlement section). There are several points about the γ -loop that will now be stated.

Chromium, which is a ferrite former, extends the α -phase field and suppresses the gamma (γ)-phase field. As a result of this, there is the formation of the so-called γ loop existing between the temperature range from 850°C to 1400°C and the compositional range of 0 to about 13% Cr.

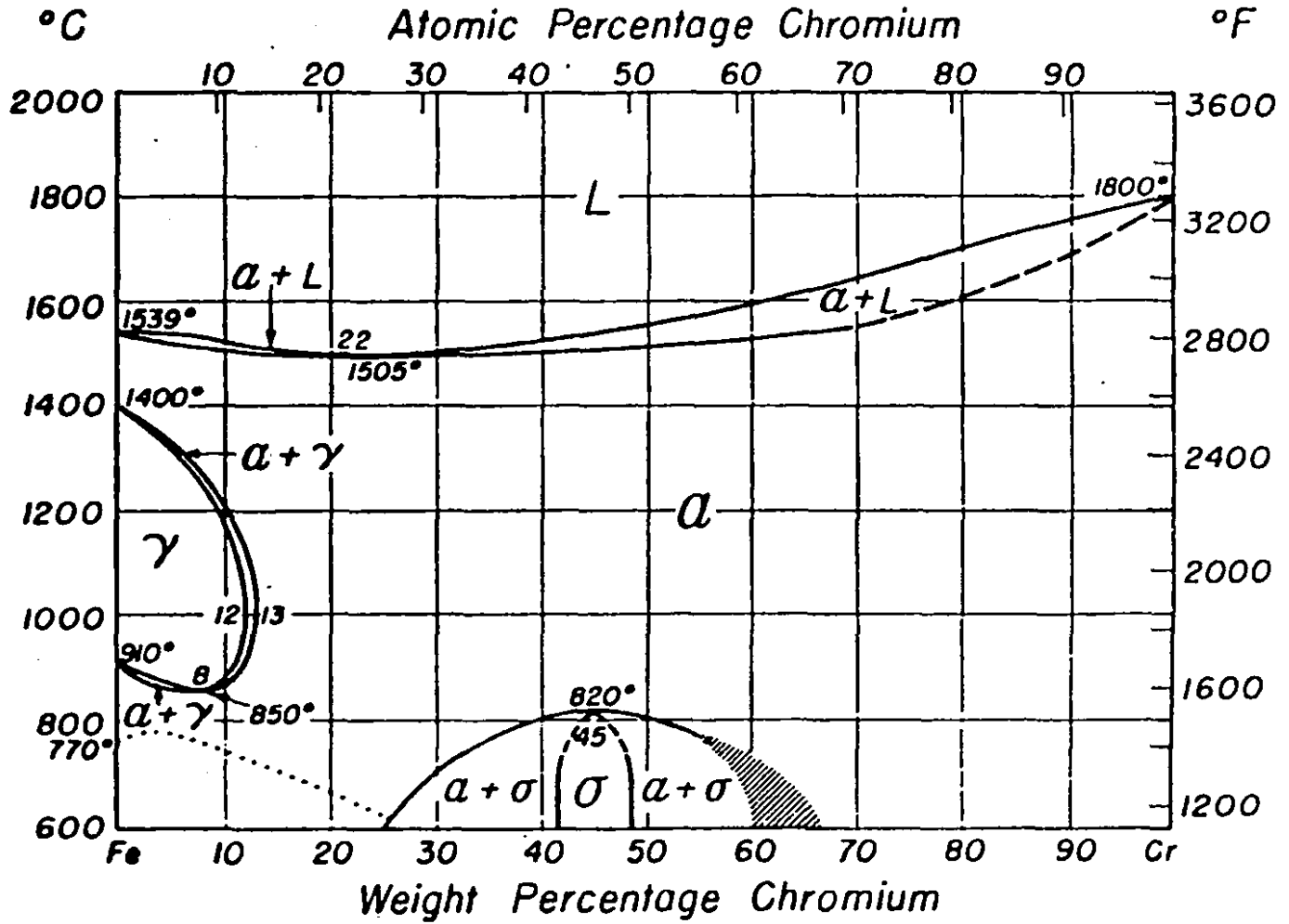


Figure II-1: Iron-chromium phase diagram

5

Chapter II - Literature Review -

Initially, upon heating from room temperature with 0% chromium, the transformation from α to γ occurs at 910°C (i.e. the equilibrium allotropic pure iron transformation temperature or the Ae_3 temperature). This transformation temperature is shown to decrease with increasing chromium down to 850°C at 8% chromium. Then there is a rapid increase with increasing chromium content, to about 12 - 13% Cr, at which point the transformation occurs at 1000°C.

On cooling, in pure iron, from the liquidus temperature of 1539°C, the transformation from α to γ occurs at 1400°C (known as the Ae_4 temperature). The Ae_4 temperature is depressed with increasing chromium content up to 12 - 13% Cr, at which point, the transformation temperature is 1000°C. This is the point at which the upper and lower transformation temperature curves meet to close off and form the γ -loop. Clearly, above 12 - 13% Cr, there is no transformation upon heating or cooling of the ferrite. Consequently, the material is completely ferritic until its melting point.

The maximum chromium limit at which a transformation to γ is possible is a very strong function of the austenitizing elements present, such as substitutional nickel, and interstitial carbon and nitrogen. The result of these additions is to increase the chromium levels at which the γ phase can exist.

Typically, under equilibrium conditions, alloys with less than about 12% Cr, such as martensitic stainless steels, undergo an α - to - γ transformation on heating into the γ temperature range, thus, allowing for the possibility of heat treatments for specific property requirements. Conversely, ferritic stainless steels cannot undergo this transformation upon heating or cooling.

Finally, between the γ -loop and the α -phase field, there exists a dual phase ($\alpha + \gamma$) region. The presence of carbon and nitrogen increases the chromium range of this dual phase region (this will be shown in the next section). By utilizing specific quenching

rates, it is possible to retain the dual phase at room temperature, creating the so-called 'Duplex Stainless Steels'.

II. 2.1. Effects of carbon and nitrogen

As mentioned earlier, carbon and nitrogen affect the location of the γ -loop in the Fe - Cr phase diagram. The effect of carbon, nitrogen and nickel on the transformation of austenite was extensively studied by Baerlecken, Fischer and Lorenz [4] using magnetic measurement testing at elevated temperatures. Figure II-2 shows the detailed α plus γ region developed by these researchers for pure Fe and Fe - Cr alloys with 0.004% (40 ppm) carbon and 0.002% (20 ppm) nitrogen. Baerlecken et al. [4] showed that austenitizing elements, particularly carbon and nitrogen, cause the outer boundary of the $\alpha + \gamma$ phase field to shift to the right (i.e., to higher chromium levels), as shown in Fig. II-3. This figure shows two distinct but additive effects for both increases in carbon and/or nitrogen, on the two-phase region, as indicated by the following observations:

- i) Both carbon and nitrogen expand the two-phase region to higher chromium contents. and,
- ii) An increase in carbon and/or nitrogen shifts the maximum extension of the $\gamma + \alpha$ phase fields to higher temperatures.

The maximum extension of the two-phase region due to increases in carbon and/or nitrogen is limited by the solidus temperature of the alloy.

Table II-1 shows that the solubility for carbon and nitrogen is greater in austenite than in ferrite. The reason for this is the larger interstitial sites that are available in austenite [1]. At any given temperature, say for example 723°C, the solubility of carbon in γ -iron (0.8 wt%) is higher than in α -iron (0.02 wt%). This same trend is true for nitrogen. However, nitrogen has a higher solubility because of its slightly smaller atomic

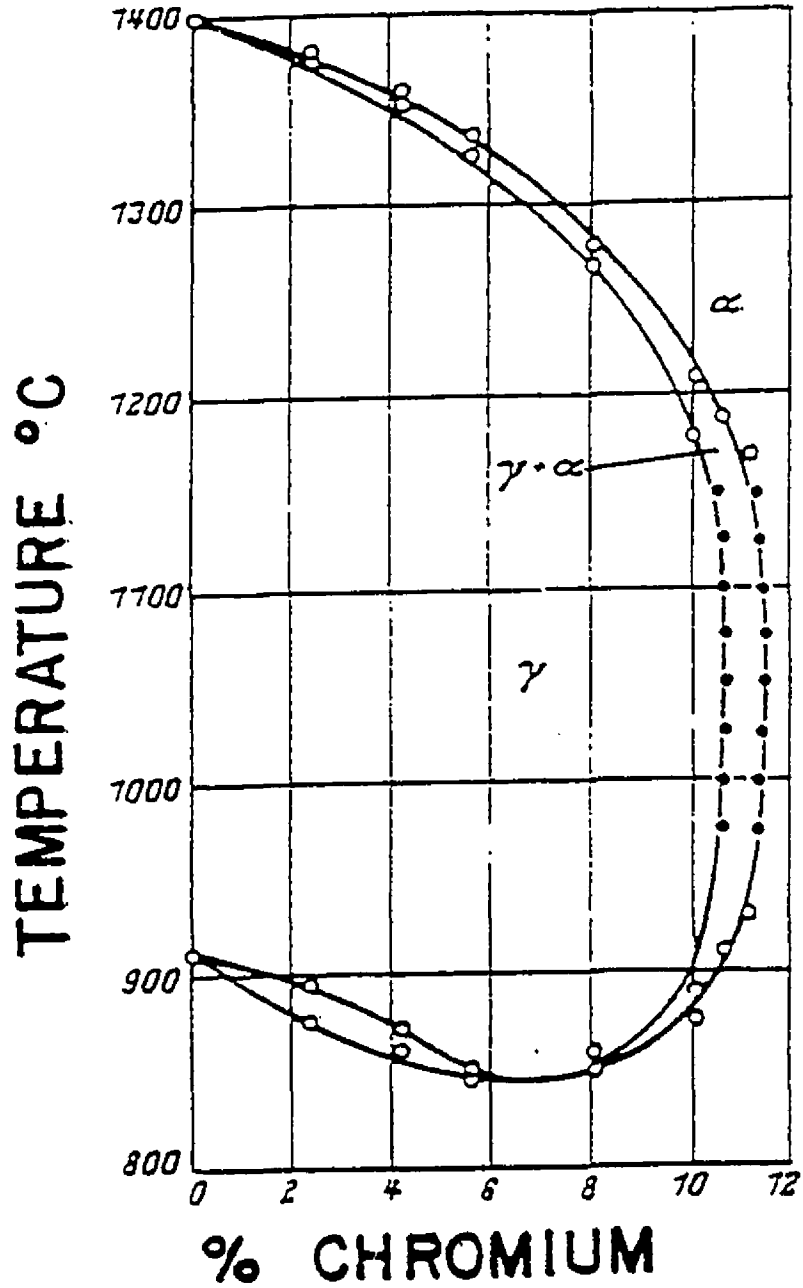


Figure II-2: Iron loop of iron-chromium phase diagram for alloys with 0.004% carbon and 0.002% nitrogen.

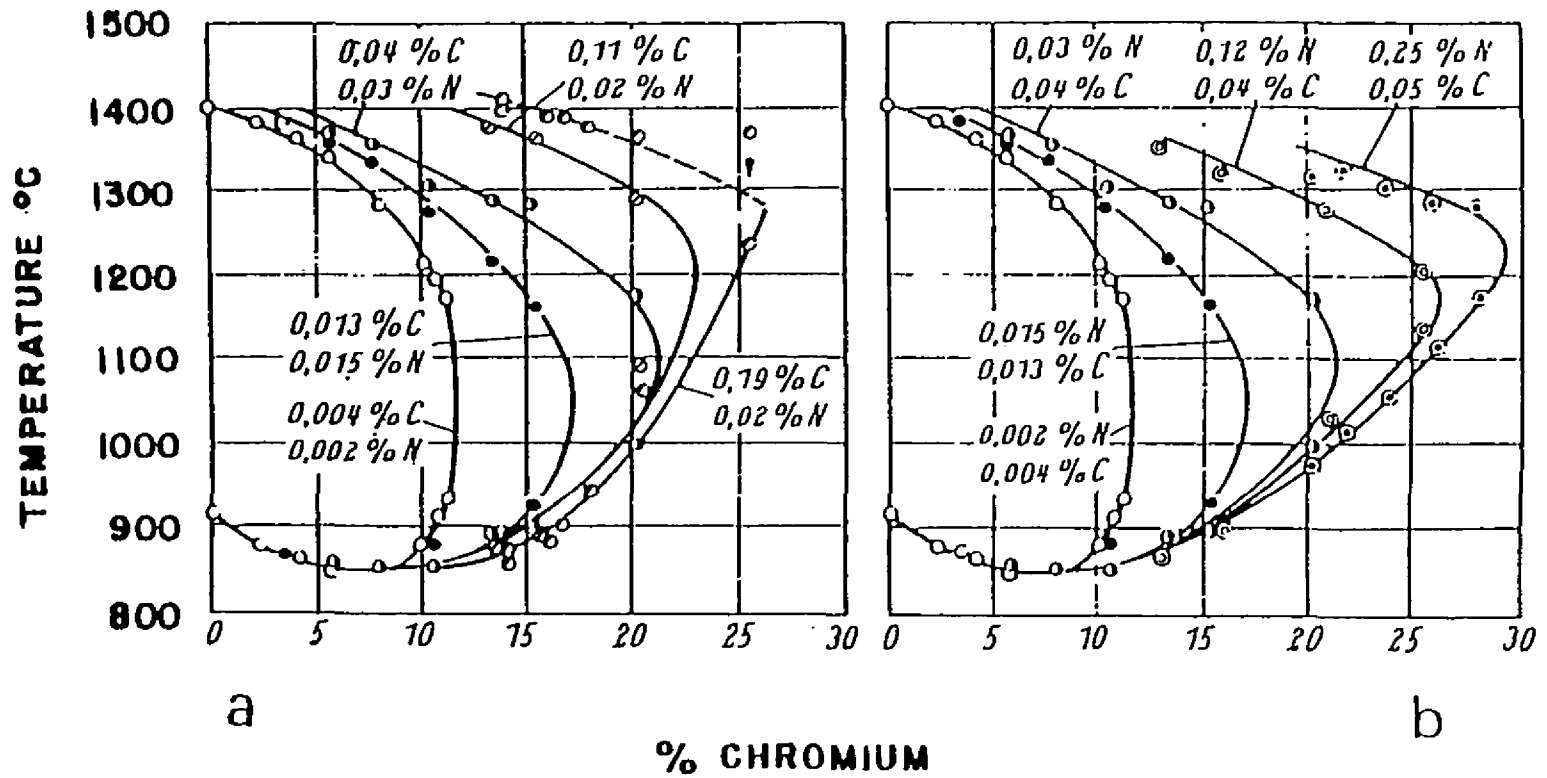


Figure II-3: Shifting of the boundary line $(\gamma + \alpha)/\alpha$ in the system iron-chromium through increasing additions of carbon and nitrogen.

radius. The outcome of this drop in solubility between γ -iron and α -iron, is the rejection of carbon (or nitrogen) from solid solution as complex carbides, $(Cr, Fe)_7C_3$ and $(Cr, Fe)_{23}C_6$, which precipitate predominantly at grain boundaries [5, 6]. These complex carbides drastically alter the properties of the alloy.

Table II-1: Solubilities of carbon and nitrogen in α - and γ -iron

	Temperature (°C)	Solubility (wt%)
Carbon in α -iron	723	0.02
	20	<0.00005
Carbon in γ -iron	1150	2.04
	723	0.80
Nitrogen in α -iron	590	0.10
	20	<0.0001
Nitrogen in γ -iron	650	2.8
	590	2.35

It is quite clear that low chromium (12 - 14%) ferritic stainless steels require low interstitial levels of both carbon and nitrogen in order to avoid the formation of a dual $\gamma + \alpha$ phase. Other austenitizing elements will promote the formation of a dual $\gamma + \alpha$ phase or a completely γ -phase, as is the case for nickel. Generally, nickel is added to stabilize austenite at room temperature. Figure II-4 shows how the nickel content affects the stability of austenite in an iron alloy containing 18% Cr. This figure suggests that, even at low temperatures and high nickel contents, the alloy would transform to ferrite. However, the transformation is sluggish enough for the austenite to persist when cooling from the γ region to room temperature or below. This is the fundamental physical metallurgy behind the production of austenitic stainless steels. The compositions of iron-chromium-nickel alloys (with no carbon) for which austenite is present at room temperature is shown in Figure II-5.

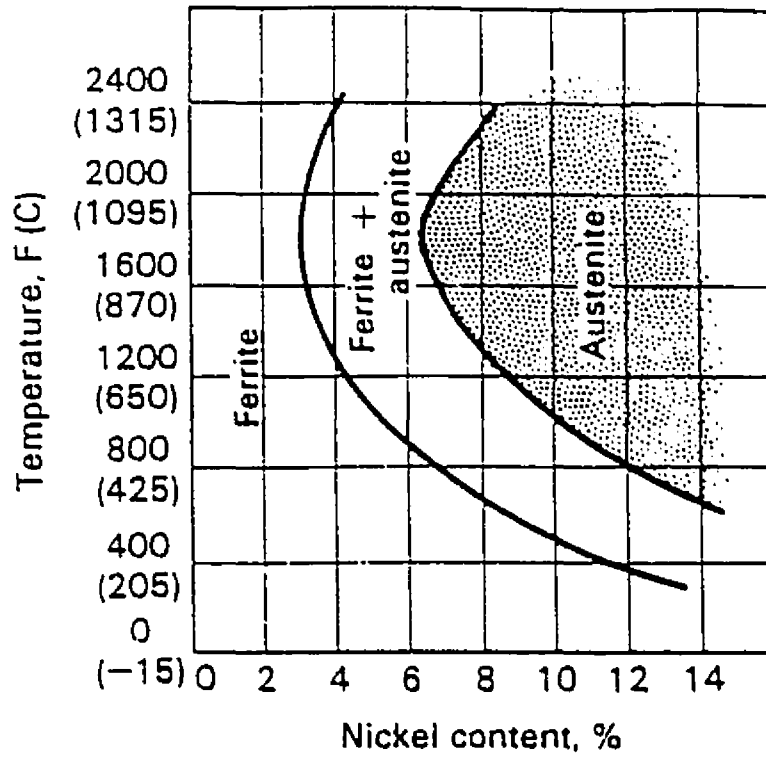


Figure II-4: Effects of nickel content on the stability of austenite in an iron alloy containing 18% chromium.

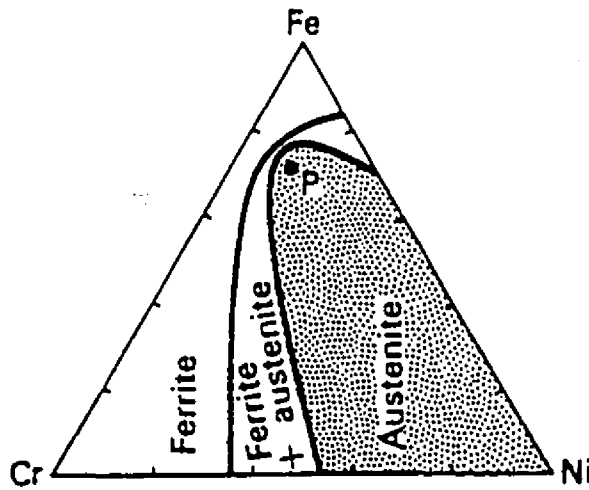


Figure II-5: Compositions of iron-chromium-nickel alloys for which austenite persists at room temperature. Point P indicates the position of an alloy containing 18% chromium and 8% nickel.

II. 3. Embrittling phenomena in ferritic stainless steels

The usual hardening and strengthening procedure for carbon and low to medium alloy steels begins by heating to the γ region and then quenching to form martensite. This will not occur in ferritic stainless steels because of the absence of an α to γ transition upon heating. An example of the effects of heat treatment on two ferritic stainless steels compared to a martensitic stainless steel is shown in Figure II-6 [7, 8]. It can be seen that there is very little variation in hardness of the 18 and 27% Cr, as compared to the 13% martensitic grade, which undergoes an α - to - γ to - martensite transition. The slight hardening is due to increases in grain size when heated above 850°C, and to small amounts of austenite formed upon heating that transform to martensite upon cooling. This essentially illustrates the inability of ferritic stainless steels to be strengthened by heating to high temperatures and then quenching. However, these alloys can be significantly strengthened by heat treatment. Unfortunately, such treatments lead to embrittlement, i.e. dramatic decreases in ductility and room temperature toughness. There are three distinctly separate forms of embrittlement: (1) sigma (σ)-phase precipitation, (2) 475°C embrittlement, and (3) high temperature embrittlement. The temperature-time diagram shown in Figure II-7 summarizes the conditions leading to the formation of the three embrittling phenomena (which are discussed in the following sections).

II. 3.1. Sigma phase

As mentioned earlier, examination of the iron-chromium phase diagram in Figure II-1 shows a second zone at lower temperatures centered about 45% Cr in addition to the γ -loop. Cook and Jones [9] produced (Figure II-8) a detailed description of the Fe-Cr phase diagram depicting the σ portion only. This diagram shows that pure σ forms between 42 and 50 % chromium, while a duplex structure of both α and σ phases forms with alloys containing as little as 20% chromium and with as much as 70% chromium, when heated to temperatures between 500 and 800°C. This phase was first detected in

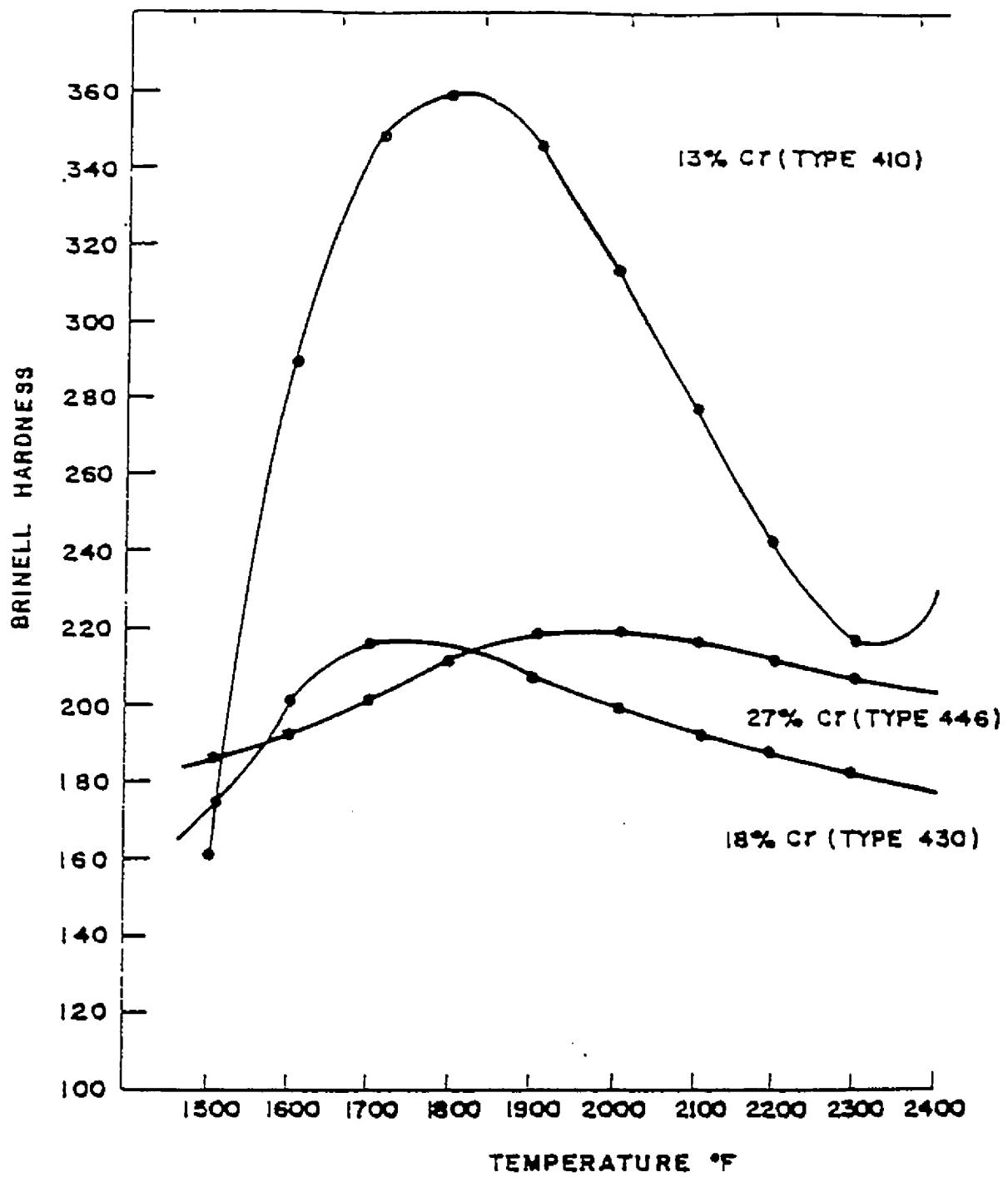


Figure II-6: Relative hardening of ferritic and martensitic iron-chromium alloys after water quenching from indicated temperatures.

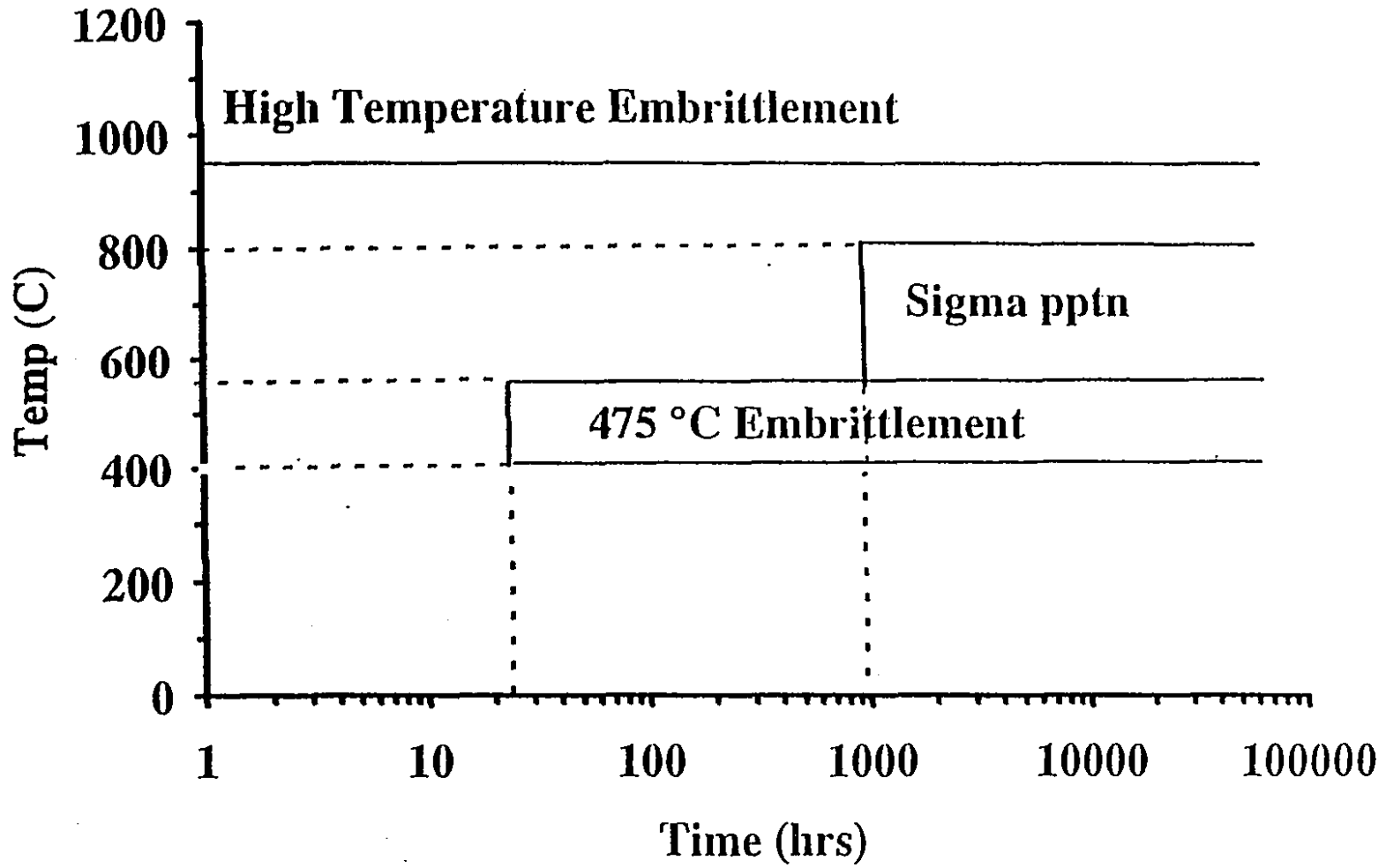


Figure II-7: Temperature versus time diagram outlining embrittlement conditions.

1927 [10, 11], and then in 1936 it was definitively identified as an intermetallic phase containing one iron atom with one chromium atom [12, 13]. This compound is hard, brittle and nonmagnetic with a tetragonal crystal structure. Sigma-phase is identifiable under the microscope and by x-ray diffraction.

Sigma-phase forms very slowly (requiring several hundreds of hours) at temperatures within the region shown on the phase diagram of Figure II-8 (i.e., 500°C to 800°C). Sigma-phase precipitates as essentially a continuous stream of 'islands' around the ferrite grain boundaries. Although the diagram indicates that σ -phase should not occur in alloys with less than 20% chromium, it has been shown [5, 12, 13, 14, 15] that elements such as, molybdenum, titanium, niobium, silicon, nickel and manganese shift the σ -forming range to lower chromium levels. Cold working also enhances the kinetics of the occurrence of σ -phase precipitation [13, 15, 16, 17, 18, 19]. The formation of this σ phase increases the hardness and results in a severe reduction in ductility and toughness [20]. Also, under some conditions, the σ -phase islands are preferentially attacked, resulting in a detrimental decrease in the corrosion resistance of the alloy. Sigma-phase, if it occurs, can be dissolved by heating to temperatures above 900°C, holding there for an hour or more, then rapidly cooling, in order to avoid 475°C embrittlement [8].

II. 3.2. 475°C embrittlement

When ferritic stainless steels containing 15 to 70% chromium are heated between 400°C and 550°C, or slowly cooled through this range, they will show a pronounced increase in hardness with a corresponding decrease in ductility, toughness and corrosion resistance [19, 20]. The severity of this embrittlement increases with chromium content. It is now generally accepted that 475°C embrittlement is due to the formation of a coherent precipitate, which occurs because of a miscibility gap in the iron-chromium system below 550°C. By extracting fine particles (200 Å in diameter) from a 28.5% Cr alloy aged for 1 to 3 years at 475°C, Fisher, Dulis, and Carroll [21] showed that the presence of a coherent precipitate exists. It was found that this precipitate has between 61

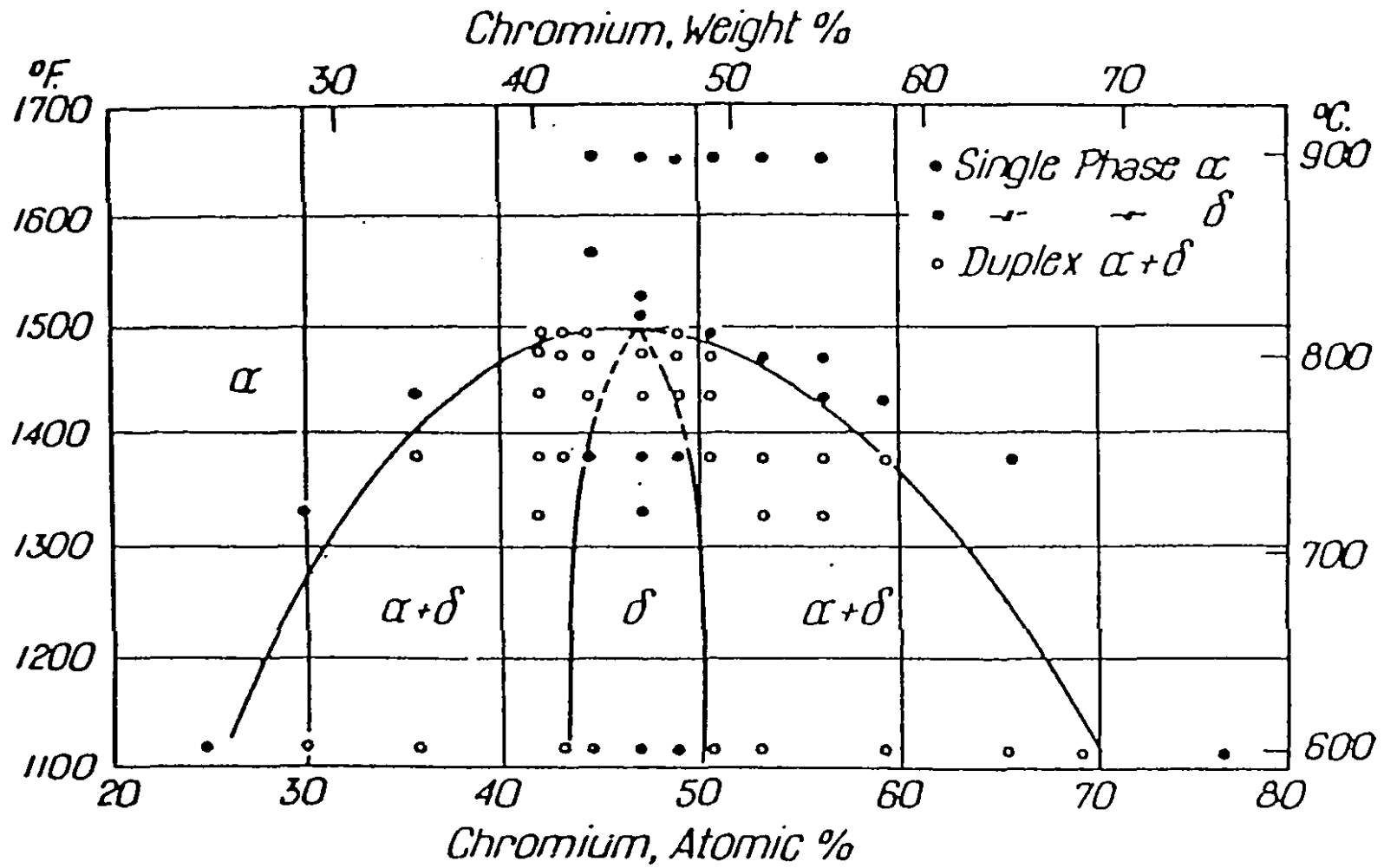


Figure II-8: Iron-chromium phase diagram in binary high purity 25 to 76% chromium alloys.

and 83% chromium, is nonmagnetic and has a bcc crystal structure with a lattice parameter, a , of 2.877 Å, between that of iron and chromium. Figure II-9 shows the extent of the miscibility gap as published by Williams [22]. This figure shows that alloys which are aged in this gap would separate into a chromium-rich ferrite (α^1) and an iron-rich ferrite (α). Additives have been shown to have little or no effect on 475°C embrittlement in ferritic stainlesses [5, 6, 23, 24, 25, 26]. However, cold working intensifies the rate of embrittlement [6].

It is possible to remove 475°C embrittlement and regain the toughness and corrosion resistance, by heating an embrittled alloy to temperatures above 550°C for long enough times. Newell [19] showed that 1 hour is sufficient at 593°C while it takes over 1000 h at 538°C to remove the embrittlement. Therefore, by heating an alloy above 800°C (thus avoiding σ -formation) and then rapidly cooling, 475°C embrittlement can be eliminated [6]. Neither 475°C nor σ -phase embrittlement is generally produced during welding or annealing at high temperatures. This makes both these embrittling problems less serious than high temperature embrittlement.

II. 3.3. High temperature embrittlement and loss of corrosion resistance

High temperature embrittlement, or sensitization, occurs in high chromium ferritic stainless steels containing moderate to high interstitial levels that are heated to above 925°C and then rapidly cooled. It commonly occurs during welding, in regions immediately adjacent to the welds. The result is an alloy with extreme losses in toughness and ductility and unacceptable reduction in corrosion resistance. This phenomenon has been studied by Demo [27], Baerlecken et al. [4], Semchyshen et al. [28], and Plumtree et al. [29]. The general conclusion is that this phenomenon is caused by precipitation of chromium-rich carbides and nitrides that result from the relief of supersaturation when the alloys are exposed to high temperatures. Semchyshen et al. and Baerlecken et al. agree that the chromium-rich precipitate forms on the grain boundaries. However, Demo and Plumtree presented the alternative postulate that there are finely

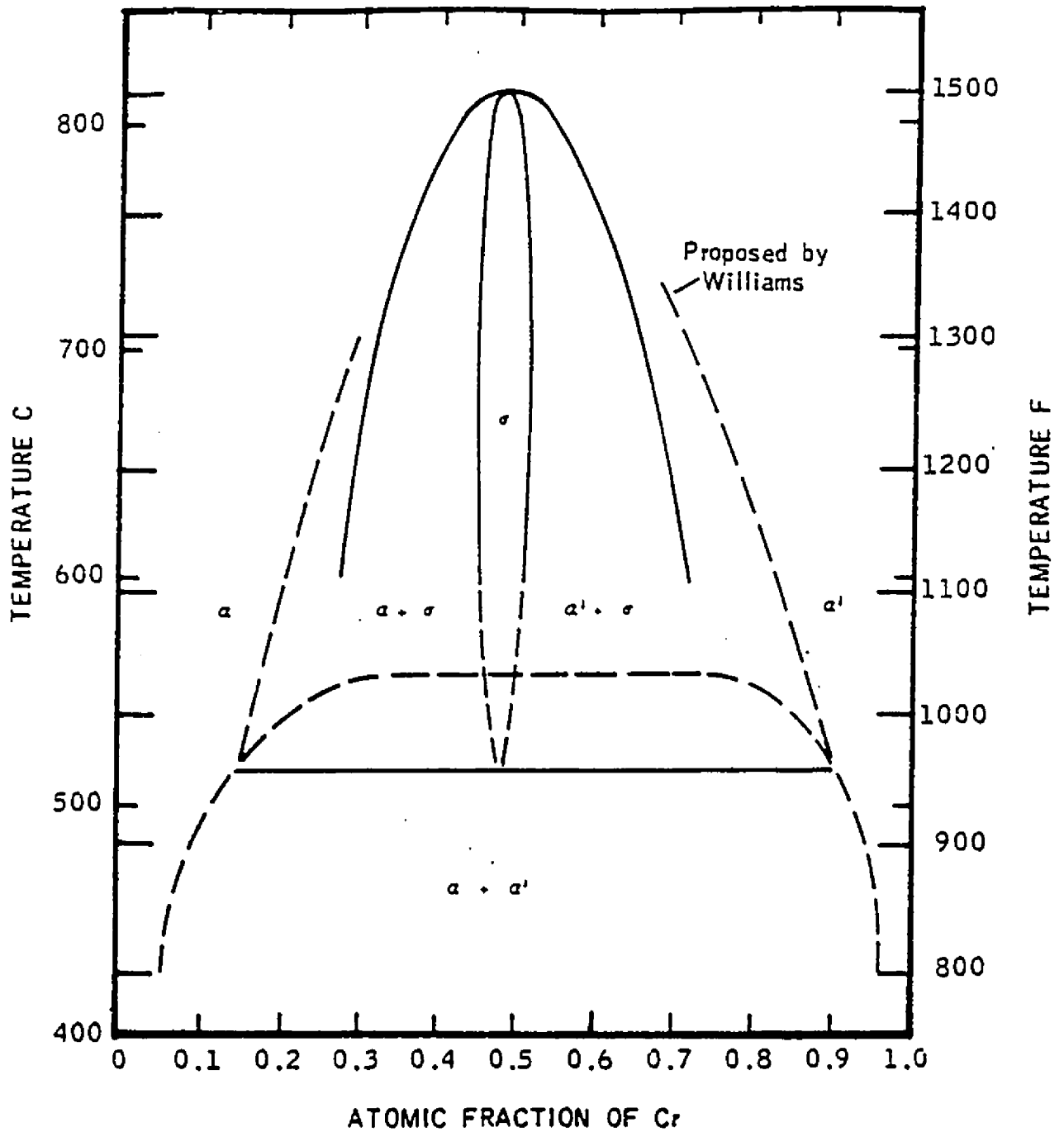


Figure II-9: Phase diagram of the iron-chromium system according to Williams [22].

dispersed precipitates in the grain matrix hindering dislocation motion. Regardless of these varying theories, the consensus is that high temperature embrittlement and loss of corrosion resistance is largely influenced by the carbon and nitrogen levels.

It is possible to eliminate the sensitization effects by heating the steel to about 750°C for an hour or so followed by air cooling. The relatively short time span is sufficient to avoid σ -phase precipitation, and the air cooling rate is great enough to avoid 475°C embrittlement. Fortunately, for the sake of usefulness of ferritic stainless steels at elevated temperatures, sufficient additions of titanium or titanium-plus-niobium are required to prevent sensitization.

II. 4. Effects of microalloying elements

It has been shown by Bond [30], Demo [31], Hochmann [32], Hodges [33, 34], and Streicher [35], that reductions in the interstitial (carbon + nitrogen) levels below certain minimum values are required for the production of highly weldable and corrosion resistant alloys. Figure II-10 [31], shows the maximum acceptable interstitial levels for as-welded ductility and intergranular corrosion resistance. The amount of tolerable interstitial levels drastically decreases with increasing chromium content. These extremely low interstitial levels (e.g., 100 ppm (C + N) in a 28% Cr alloy) are not yet economically produced commercially, even with VOD technology. However, with the additions of titanium, niobium, zirconium, and tantalum, carbonitrides are formed, thus effectively controlling the interstitial levels (as will be shown in the following sections).

II. 4.1. Titanium

The addition of titanium, in the order of about six to ten times the combined carbon and nitrogen content, has been shown [37, 38, 39, 40] to effectively prevent high temperature embrittlement (sensitization). Demo [39, 40] studied the relationship

between interstitial carbon, chromium level, and titanium level for intergranular corrosion and ductility after welding. His and other [37, 38, 41, 42, 43] research results showed that, under exposure to highly oxidizing solutions, such as boiling nitric acid, titanium stabilized alloys display intergranular attack, due to dissolution of the carbonitrides. As shown in Tables II-2 and II-3, Demo [39, 40] and Wright [44] have summarized the effects of additions of titanium and niobium on the weld ductility of ferritic stainless steels. These findings indicate that significant increases in interstitial level can be tolerated without adversely affecting the as-welded ductility of the steel. Table II-2 displays tensile ductility measurements, while in Table II-3 the results were obtained from 'slow bend tests'. The interstitials are effectively stabilized through the precipitation of stable carbides and nitrides, thus reducing the level of interstitials in solid solution. Not all stabilization effects are constructive. Semchyshen et al [28], and Wright [44] showed that the impact resistance of annealed specimens with and without titanium additions is equivalent. However, specimens, with up to 0.5% titanium, when heated to high temperatures by welding or isothermal heat treatments showed improved (lower) impact transition temperature (when quenched from 1150°C) (see Figure II-11). Also, it can be seen that that beyond 0.5% titanium, there is an increase in the transition temperature. This was shown by Semchyshen [28] to be due to a precipitation of an intermetallic phase.

II. 4.2. Niobium

Niobium has similar effects as titanium (see Table II-2 and Figure II-11). There are some differences. First, about eight to eleven times the carbon and nitrogen wt% level is required for stabilization of the interstitials [37, 38, 39, 40]. Second, niobium stabilized alloys are highly resistive to intergranular attack from extremely oxidizing solutions. Third, in the annealed condition, niobium stabilization is actually harmful to the impact resistance of an alloy (as shown in Figure II-11 above). Overall, however, the effects of interstitial stabilization on alloys with moderate amounts of carbon and nitrogen may improve the as-welded ductility and corrosion resistance tremendously, but will not

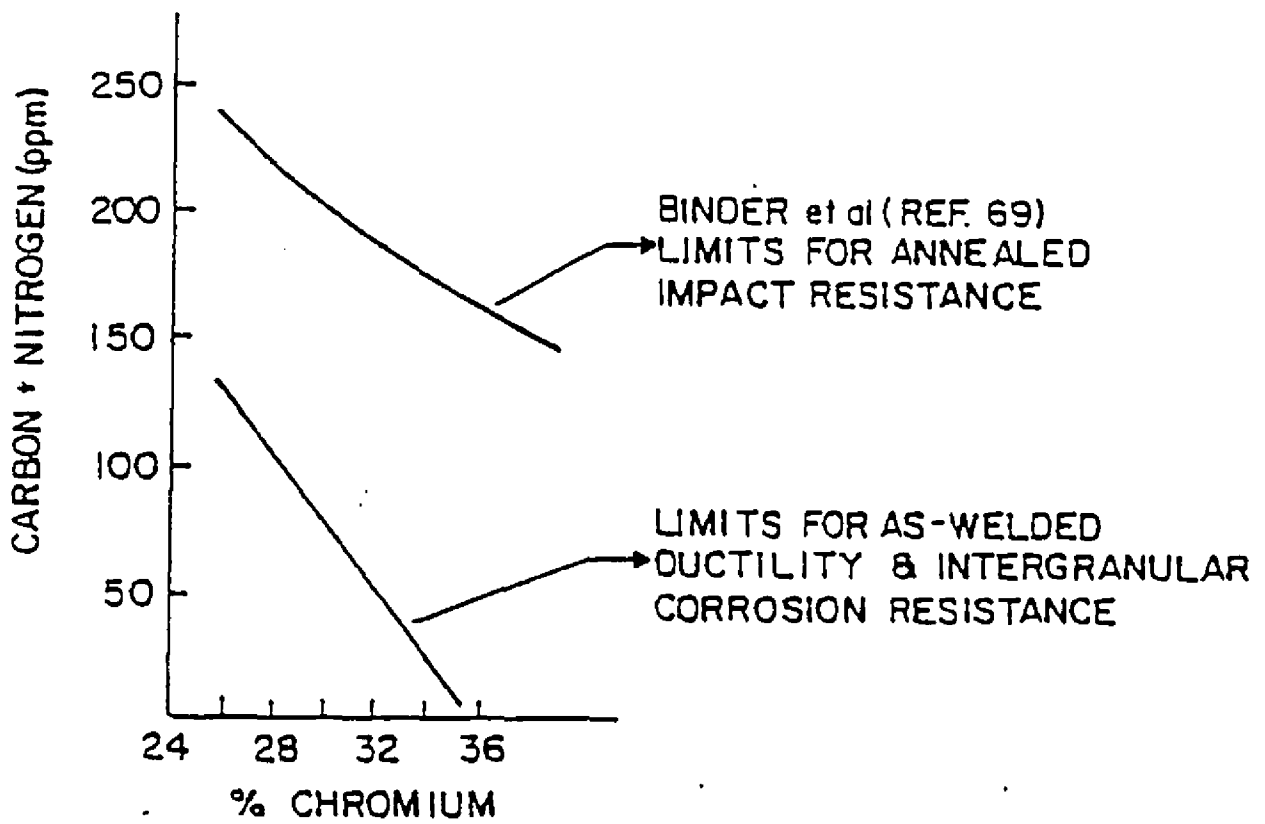


Figure II-10: Effects of carbon and nitrogen level and chromium content on as-welded ductility and intergranular corrosion resistance of chromium-iron ferritic stainless steels.

Chapter II - Literature Review -

Table II-2: Effect of stabilizer additions on the tensile ductility of annealed versus welded specimens containing 18% chromium-2% molybdenum.

C + N, wt.%	Ti or Nb, wt.%	Elongation in 50 mm, %	
		Annealed	As-Welded
0.005	0	33	31
0.03	0	31	8
0.07	0.5	34	30
0.06	0.6	28	21

Table II-3: Effect of titanium on the as-welded bend ductility for ferritic stainless steels containing 26 to 30% chromium.

C + N, ppm	Ti, wt.%	Bend Test
		Ductility As-Welded
113	0	passed 180°
310	0	passed 180°
362	0	failed 90°
450	0	failed 90°
900	0	failed 135°
300	0.22	passed 180°
387	0.24	passed 180°
488	0.47	passed 180°
850	0.45	passed 180°

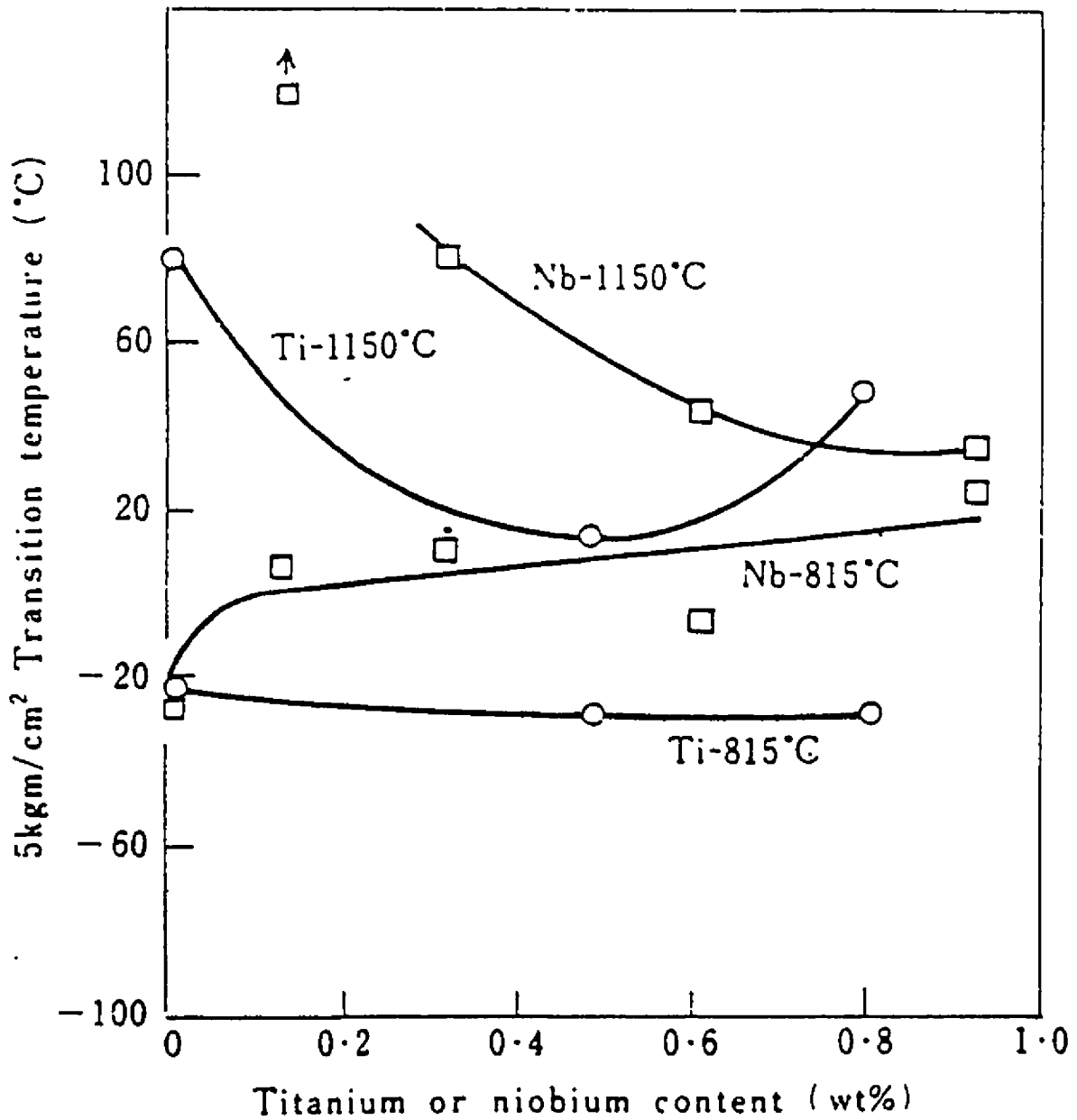


Figure II-11: Impact Transition temperatures for quarter-size Charpy V-notch specimens air-melted commercial-purity 18Cr-2Mo steel water quenched from 1150°C (sensitized) and 815°C (annealed) as a function of titanium or niobium content.

improve the annealed impact behaviour significantly. It is now generally accepted that a high-purity material will have excellent toughness and as-welded corrosion resistance and ductility. Whereas, a stabilized material might also display remarkable as-welded corrosion resistance and ductility, it may not have adequate room temperature impact resistance.

II. 4.3. Molybdenum

The addition of molybdenum has been known to improve the corrosion and pitting resistance of ferritic stainless steels. However, molybdenum can cause embrittlement of iron-chromium stainless steels, as well as having a detrimental effect on its impact transition temperature. Semchyshen et al. [28] summarized these results in Figure II-12. This figure indicates that additions of up to 2 to 3% have little effect on toughness but adverse effects are prevalent at higher molybdenum levels (3 to 5%).

Finally, improvement in as-welded ductility can be achieved by adding low concentrations of selected elements with atomic radii within 15% of the α matrix. Steigerwald et al. [45] showed that elements such as copper, aluminum and vanadium meet the above requirements and are quite effective (see Figure II-13).

II. 5. Precipitation

Precipitates in HSLA (High Strength Low Alloy) steels are known to affect the TMP and room temperature mechanical properties of these steels significantly [46, 47, 48, 49, 50]. Moreover, the basic requirement for conventional controlled rolling (CCR) is the formation of strain induced carbonitride precipitates [51]. It is believed that the mechanisms of precipitation in austenitic and precipitation hardening stainless steels are similar to that in HSLA steels [1, 52]. However, there has been little research on precipitation (other than those causing embrittlement [3]) in ferritic stainless steels. The

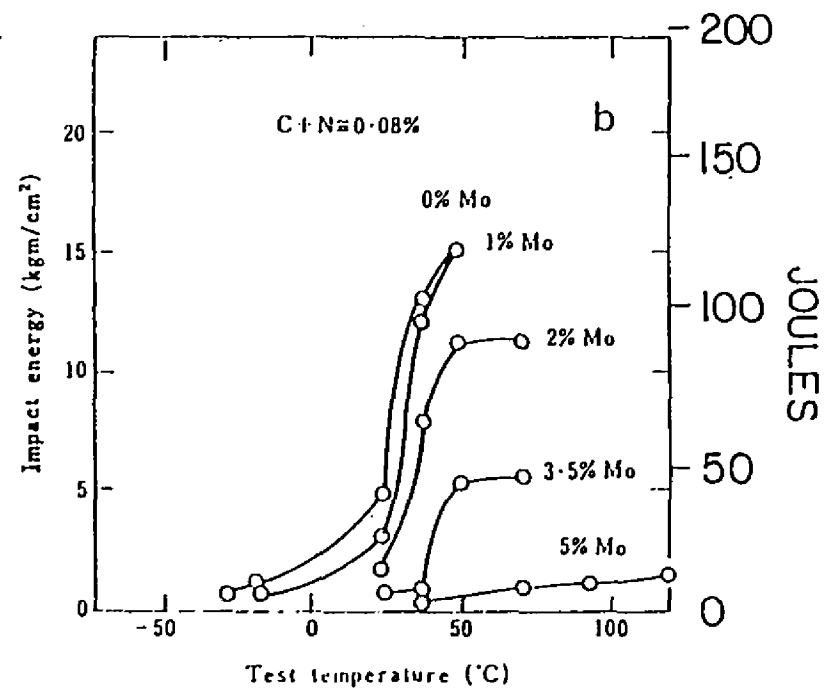
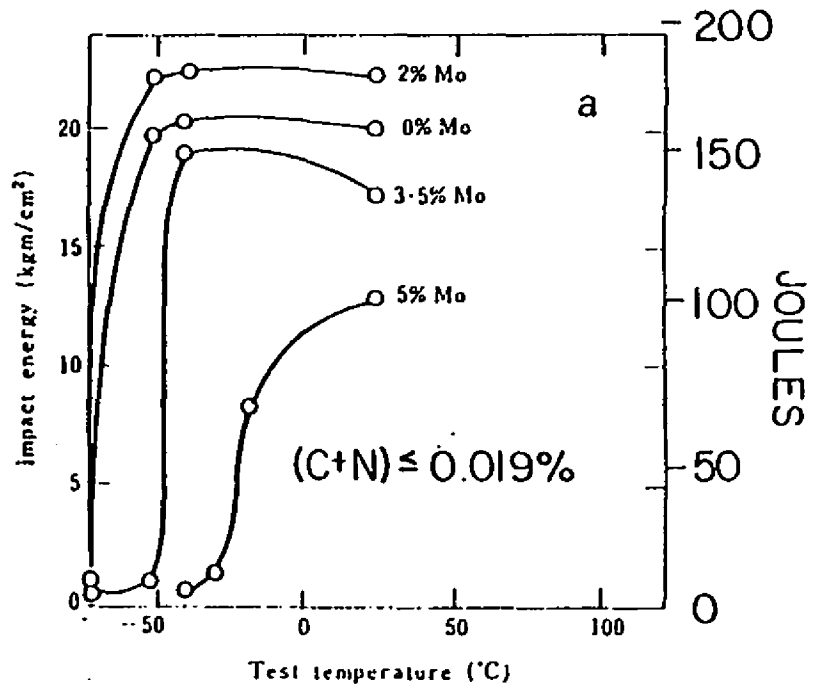


Figure II-12: Effects of molybdenum addition on impact transition temperature of annealed 25Cr-Fe stainless steels, (a) vacuum melted and (b) air-melted. Quarter-size Charpy V-notch impact specimens.

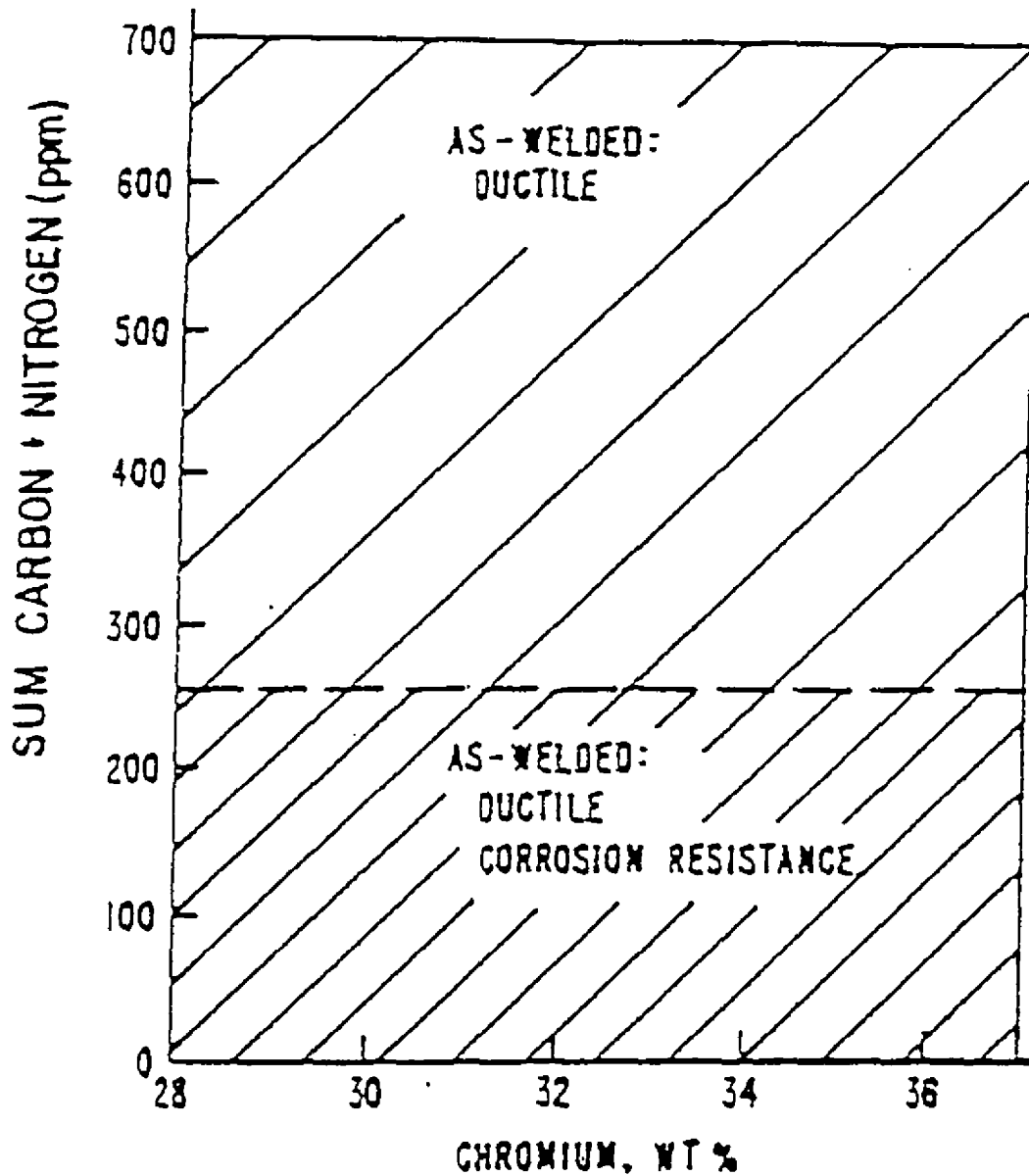


Figure II-13: Effect of weld ductilization additives on as-welded ductility and corrosion resistance of high chromium-iron stainless steels; additives, singly or in combination, include aluminum, copper, vanadium, platinum, palladium, and silver in a range 0.1 to 1.3%.

reason for this lack of research activity was that, in the past, conventional wisdom was reluctant to embrace the possibility of dynamic recrystallization due to the inherently high stacking fault energies in ferrite [53]. Also, since there is no γ to α transformation in ferritic stainless steels, grain boundary precipitates are not crucial (other than their slight effect on slowing grain growth [1, 54]).

The present work suggests that precipitation in ferritic stainless steels can lead to significant increases in high temperature flow stress and possibly to the prevention of dynamic recrystallization [51, 55]. Therefore, this section is included for a general understanding of the effect of precipitates on the TMP of ferritic stainless steels.

II. 5.1. Nucleation and growth

According to Christian [56] a particle can nucleate in two basic ways: (i) *heterogeneously*, at lattice defects such as (in increasing order of preference [57, 58]): vacancies, dislocations, dislocation nodes (i.e. the intersection of two or more dislocations), stacking faults, impurity particles, grain boundary discontinuities or at free surfaces. (ii) *homogeneously*, where nuclei are spontaneously formed through compositional fluctuations of the solute (i.e. within the matrix). Heterogeneous nucleation is much more prevalent.

II. 5.1.1. Homogeneous nucleation

Homogeneous nucleation occurs with a great deal of difficulty in a supersaturated liquid or solid solution. In fact, even in the freezing of ultra pure water, homogeneous nucleation requires substantial supercooling ($\approx -40^\circ\text{C}$). Thermodynamics describes the possibility of forming a stable nucleus, and kinetics describes the rate of the nucleation and growth reactions. By considering an equilibrium situation, where a new phase (β) nucleates in a single (α) phase, the transformation is extremely sluggish at the equilibrium transformation temperature (T_E). An increase in the cooling rate results in an increase in

supercooling, which leads to a faster nucleation rate. It has been shown [57] that the total free energy change, ΔG , associated with nucleation (i.e. the formation of a β embryo) can be written as follows:

$$\Delta G = -V\Delta G_v + AY + V\Delta G_e \quad (2.1)$$

where,

- V = volume of nucleus (or β embryo),
- ΔG_v = volume free energy change between the nucleus and solute atoms,
- A = interface area of the nucleus,
- Y = interface energy, and
- ΔG_e = misfit or elastic strain energy per unit volume.

By assuming that the nucleus is a sphere with radius r , and using the free energy diagram in Figure II-14, it is possible to determine a critical stable nucleus radius, r^* :

$$r^* = -2Y / (\Delta G_v + \Delta G_e) \quad (2.2)$$

and, the critical free homogeneous nucleation energy, ΔG^*_{Hom} :

$$\Delta G^*_{Hom} = 16\pi Y^3 / 3(\Delta G_v + \Delta G_e) \quad (2.3)$$

II. 5.1.2. Heterogeneous nucleation

As mentioned earlier, nucleation is almost always heterogeneous in nature [57, 58]. This is because nucleation sites (mentioned earlier) are nearly always present. The formation of nuclei can result in the release of free energy by the destruction of a defect, thus, effectively reducing the activation energy barrier.

Chapter II - Literature Review -

Heterogeneous nucleation can be described, for example, by considering the formation of a spherical β embryo on a flat surface (Figure II-15).

Equation (2.4) below gives the free heterogeneous nucleation energy for a β embryo, ΔG_{Hct} (assuming $\sigma_{\alpha\beta}$ to be constant):

$$\Delta G_{\text{Hct}} = V_s (\Delta G_v + \Delta G_e) + A_{\alpha\beta} \sigma_{\alpha\beta} + A_{\beta S} \sigma_{\beta S} - A_{\beta S} \sigma_{\alpha S} \quad (2.4)$$

where V_s is the volume of the embryo, $A_{\alpha\beta}$ and $A_{\beta S}$ are the areas of the α/β and $\beta/\text{surface}$ interfaces, and $\sigma_{\alpha\beta}$, $\sigma_{\beta S}$, and $\sigma_{\alpha S}$ are the surface energies per unit area. A modification of the above equation (2.4) can be made in terms of contact angle (θ) and spherical-cap radius (r):

$$\Delta G_{\text{Hct}} = \left[\frac{4}{3} \pi r_{\alpha\beta}^3 (\Delta G_v + \Delta G_e) + 4 \pi r_{\alpha\beta}^2 \sigma_{\alpha\beta} \right] S(\theta) \quad (2.5)$$

where

$$S(\theta) = \frac{2 - 3 \cos \theta + \cos^3 \theta}{4} \quad (2.6)$$

Now the critical radius $r_{\alpha\beta}^*$ can be obtained:

$$r_{\alpha\beta}^* = - \frac{2 \sigma_{\alpha\beta}}{\Delta G_v} \quad (2.7)$$

Also, for the same ΔG_e :

$$\Delta G_{\text{Hct}}^* = \Delta G_{\text{Hom}}^* \cdot S(\theta) \quad (2.8)$$

Since $S(\theta)$ is between 0 and 1, the energy barrier for heterogeneous nucleation, ΔG_{Hct} , is lower than for homogeneous nucleation, ΔG_{Hom} (see Figure II-14).

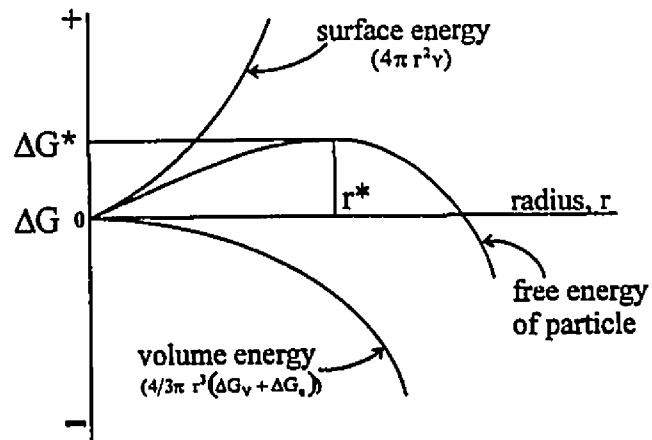


Figure II-14: Free energy of a precipitate particle as a function of its radius.

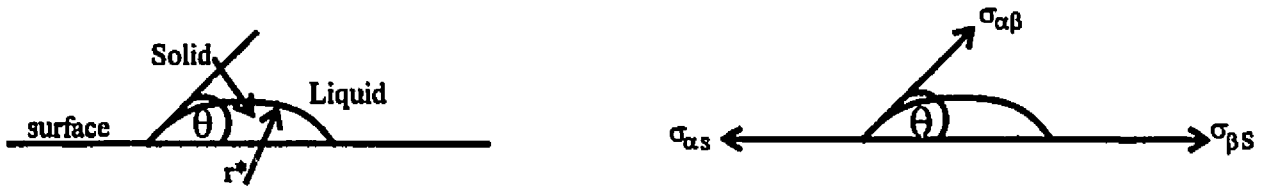


Figure II-15: Model for heterogeneous nucleation on a flat surface; (a) cross-section through spherical cap; and (b) energy balance at the solid-liquid-surface junction [59].

II. 5.2. Ostwald ripening

The general consensus [1, 46, 47, 48, 50, 58, 60, 61, 62] regarding precipitation hardening is that the smaller and more numerous (large volume fraction and/or small interparticle distance) the precipitates, the greater the strengthening effect. The relationship between strength and precipitate size distribution has been analyzed by Gladman et al. [63], and their findings are expressed in equation (2.9) below:

$$\sigma (MPa) = \frac{5.9 f_v^{1/2}}{\bar{L}} \ln \left(\frac{\bar{L}}{2.5 \times 10^{-4}} \right) \quad (2.9)$$

where f_v is the particle volume fraction and \bar{L} is the mean planar intercept length of the precipitates. According to this equation (2.9), precipitation hardening increases with decreasing particle size and increasing volume fraction. It has been shown [46] that, because of their low solubilities, niobium and titanium carbonitrides are among the most effective precipitates for strengthening [46].

The previous section described the nucleation and growth of precipitates. The volume fraction of precipitates continues to rise until equilibrium is reached. Then precipitate coarsening, or Ostwald ripening, occurs. That is, large precipitates grow at the expense of small ones, without an increase in volume fraction. This results in a decrease, or even the elimination, of the strengthening effect of the precipitates [46, 50, 60]. Note that for isothermal precipitation, there is an “incubation time”, P_s , associated with nucleation, i.e. the start of precipitation, and the onset of Ostwald ripening is associated with the end of precipitation, which occurs after a time P_f . Why and how precipitates coarsen is explained as follows.

Chapter II - Literature Review -

First, consider two differently sized spherical precipitates (see Figure II-16). The free energy of a particle, ΔF , can be expressed as follows:

$$\Delta F = -A_1 r^3 + A_2 r^2 \quad (2.10)$$

where A_1 and A_2 are constants.

The total free energy per unit volume of a precipitate, $\Delta F'$, can be obtained by dividing equation (2.10) by the volume of the precipitate:

$$\Delta F' = \frac{\Delta F}{\frac{4}{3}\pi r^3} = -A_1' + \frac{A_2'}{r} \quad (2.11)$$

where,

$$A_1' = A_1 / \frac{4}{3}\pi \quad \text{and} \quad A_2' = A_2 / \frac{4}{3}\pi \quad (2.12)$$

Since $\Delta F'$ is proportional to the free energy per atom, F_a , we can express F_a as:

$$F_a \approx -A_1'' + \frac{A_2''}{r} \quad (2.13)$$

Where $A'' = A' \cdot \Omega / N_0$, Ω is the molar volume of a precipitate, and N_0 is avogadro number

This expression states the free energy per atom is inversely proportional to the particle radius. Therefore the larger the radius the more stable the precipitate. Conversely, the smaller the radius, the less stable it is. Moreover, solute atoms leave the smaller particles and enter the matrix, while simultaneously, they leave the matrix to enter the larger particles. This is now a diffusion controlled process through the matrix.

The rates or kinetics of Ostwald ripening have been analyzed by various researchers [64, 65, 66, 67], leading to kinetic equations of the form:

$$\bar{d}_v - \bar{d}_0 = K_c (t - t_0)^{1/2} \quad (2.14)$$

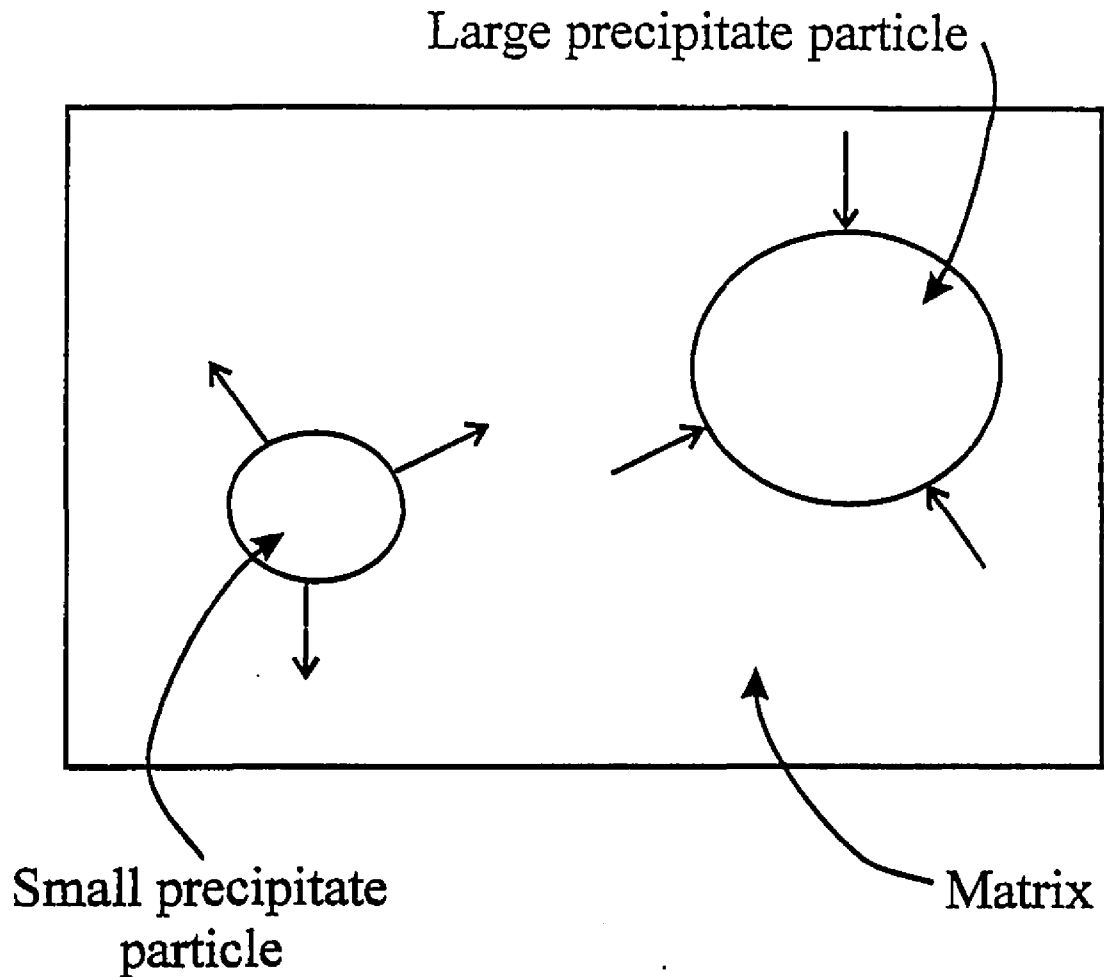


Figure II-16: Growth of precipitate particle. Small arrows at surfaces of particles indicate the net direction of the flow of solute atoms [58].

where, \bar{d}_v and \bar{d}_0 are the mean volumetric diameters of the particles at time t and t_0 respectively, K_c is the coarsening parameter, and n equals 3, 4 or 5 depending on the rate limiting mechanism. That is, $n = 3$ when coarsening is controlled by bulk diffusion [64, 64], $n = 4$ if controlled by grain boundary diffusion [66, 67] and $n = 5$ if controlled by pipe diffusion [68, 69].

II. 5.3. Static precipitation

Static precipitation is considered here to be that which occurs in undeformed microstructures. In most cases, since it is impossible to have a dislocation or grain boundary free structure, static precipitation will be heterogeneous. However, the kinetics of static precipitation are very sluggish.

II. 5.4. Strain induced precipitation

Strain induced precipitation can only occur after the microstructure has been deformed (i.e. after straining). This type of precipitation has been extensively investigated [e.g. 51, 57]. The precipitation rate and extent is increased because of the increased number of dislocations and therefore nucleation sites. Dislocations effectively reduce the critical free energy for nucleation, ΔG^* . Also, solute atom segregation around dislocations is possible, which leads to supersaturation, and therefore to the initiation of local precipitation.

Today, the conventional controlled rolling (CCR) process relies on strain-induced precipitation for two reasons. Firstly, the strain-induced precipitation of niobium or titanium carbonitrides can prevent the occurrence of static recrystallization during the interpass intervals [51, 70] via pinning of the grain and sub-grain boundaries and also of

individual dislocations. Secondly, it prevents the nucleation of dynamic recrystallization [51], which, due to the large accumulation of strain, would otherwise take place.

Studies [71, 72, 73] have been carried out to investigate the effect of deformation on the precipitation kinetics in niobium bearing steels. The results indicate that the kinetics of static precipitation in deformed (5% strained) austenite are approximately one order of magnitude faster than in undeformed austenite. Such an increase in the kinetics is also likely to be valid in ferrite.

II. 5.5. Dynamic precipitation

Unlike the previous forms of precipitation, dynamic precipitation occurs while the material is being deformed. Deformation has been found to increase, by up to 10,000 times, the coarsening rate of iron-carbide particles [74]. This was accounted for by dislocation climb around the precipitates, and 'sweeping' of the solutes by moving dislocations, thus allowing for continuous coarsening. Recently, there has been growing interest in the nucleation and growth mechanisms of dynamic precipitation, because of its ability to effectively inhibit dynamic recrystallization during rolling. However, under creep conditions (i.e. very slow strain rates) precipitation and coarsening can occur much earlier than dynamic recrystallization. Thus, dynamic recrystallization is not retarded by the presence of these precipitates [73]

The nucleation model proposed by Liu [75] stated that since the mismatch between Ti(CN) precipitates and the austenite matrix is approximately 18%, precipitation usually occurs on lattice defects (i.e. heterogeneous nucleation). Moreover, mobile dislocations can be converted into interface dislocations, by dynamic nucleation on the dislocation. This compensates for the lattice mismatch, and results in the pinning of the dislocations. Similarly, during particle growth, a vacancy poor zone is created, dislocations glide into this zone and act as vacancy sources. The net result of this 'vacancy emission' is dislocation climb towards the growing particle, where some

segments of the dislocation contact the particle and become part of the interface dislocations. Thus, they are pinned. It has also been shown [76, 77] that the generation of vacancies (by deformation) accelerates the nucleation and growth of precipitates. Furthermore, the kinetics of dynamic precipitation have been reported [71] to be one order of magnitude faster than strain-induced precipitation.

II. 6. Continuous cooling precipitation (CCP) diagrams

There have been many research studies performed [63, 70, 71, 73, 78, 79, 80, 81, 82, 83, 84] to produce PTT diagrams, to generate the relationship between precipitation, time and temperature. The main limitation of precipitation-time-temperature (PTT) diagrams is that they refer to isothermal precipitation. Thus, they cannot be used to accurately predict precipitation under industrial hot rolling conditions, which involve continuous cooling. However, there have been several successful attempts to use the isothermal P_s (precipitation start) and P_f (precipitation finish) times to calculate continuous cooling precipitation (CCP) [72, 85, 86] diagrams, thus creating the ability to model industrial hot rolling parameters with respect to precipitation.

II. 6.1. Current methods of predicting P_s times during isothermal holding

The first thermodynamic model to predict the P_s times of niobium carbonitride precipitation was developed by Dutta and Sellars [72] in 1987 (the D-S model). This model was modified by Russell [87], and now the P_s time in the D-S model is expressed as:

$$P_s = C [X_{Nb}]^1 \exp\left(\frac{27000}{RT}\right) \exp\left(\frac{B}{T^3 (\ln K_s)^2}\right) \quad (2.15)$$

where,

$$C = \frac{N_c}{a} \quad \text{and} \quad B = \frac{16\pi\gamma^3 V_m^2 N_a}{3R^3} \quad (2.16)$$

Here, X is the concentration of the element that controls the rate of the nucleation process, N_c is the critical number of nuclei per unit volume, a is the lattice parameter, and V_m is the molar volume $e^{Nb(CN)}$.

It was discovered by Liu and Jonas [85] that the D-S model did not satisfactorily predict the precipitation start time of titanium carbonitrides. They developed an alternative model (L-J model) for the prediction of P_s times in a titanium microalloyed steel:

$$P_s = H(\rho X_{Ti})^{-1} \exp\left(\frac{Q}{RT}\right) \exp\left(\frac{\Delta G^*}{kT}\right) \quad (2.17)$$

where,

$$H = N_c a^3 / D_0 \quad (2.18)$$

Here, D_0 is a frequency, k is Boltzmann's constant, and Q is the activation energy for the diffusion of solute atoms. The two main differences between the L-J model and the D-S model are: the second exponential term, and the fact that all the terms in the L-J model have a clear physical and thermodynamic meaning.

Most of the above variables can be determined [86] with the exception of the critical number of nuclei (N_c) and the dislocation density (ρ). However, it is still possible to calculate P_s times by assuming that the ratio, N_c/ρ , is constant in the test temperature range. Therefore, this ratio can be obtained by using experimental data from appropriate PTT diagrams.

II. 6.2. Current method of predicting P_f times during isothermal holding

A method for predicting P_f times was recently developed by Park [86]. This method employed the original Johnson-Mehl-Avrami (J-M-A) equation:

$$Y = 1 - \exp(-bt^n) \quad (2.19)$$

where, 'Y' is the fraction precipitated, 'b' is the rate constant, 'n' is the time exponent and 't' is the precipitation time.

Park [86] showed that the rate constant (b) can be expressed, as a complex equation, in terms of solute concentration, precipitate radius, lattice parameter, activation energy, frequency factor, critical free energy, and R, k, and T. He also showed that the time exponent (n) varies between 0.7 and 2.5 depending on the temperature and the fraction precipitated. However, there is a lack of accurate kinetic data for precipitation which makes it almost impossible to determine the exact values of 'n' and 'b', unless at least two boundary conditions are assumed (e.g. growth only, and nucleation and growth, each having its own time exponent and rate constant).

Again, as was the case for the P_s times, both the critical number of nuclei (N_c) (for the growth model) and the dislocation density (ρ) (for the nucleation and growth model) are still unknown. Therefore, these have to be determined from the rate constant of each experimental PTT data set.

II. 6.3. Current method of modeling CCP diagrams based on P_s and P_f times

Continuous cooling precipitation diagrams can be used to help model industrial hot rolling processes. There are two methods of constructing CCP diagrams. The more common method is to determine P_s and P_f times during isothermal holding and then use the additivity rule [88]. Alternatively, CCP diagrams can be constructed by means of a newly developed compression technique. The former method will be described in this section, and the latter (which is the focus of this work) will be introduced and developed in the remaining chapters.

The previous subsections outlined the equations used to determine both the P_s and P_f times with the aid of PTT diagrams. In order to predict (or construct) a CCP diagram, one must use the additivity rule developed by Scheil [88] in 1935 to predict phase transformation behaviour during continuous cooling from isothermal data [89, 90, 91, 92, 93, 94].

The concept of the additivity rule is shown in Figure II-17. This figure shows that the cooling curve is divided into several steps: $\tau_x(T_i)$ is the time required for the reaction to reach $x\%$ at temperature T_i , and ΔT_i is the incremental hold time at the T_i^{th} temperature.

It was proposed by Scheil [88] that the reaction begins when the sum of the ratios of the reaction time to reaction start time reaches unity. Umemoto et al. [89, 90, 91, 92, 93, 94] extended this to predict the time when the reaction reaches $x\%$:

$$\sum_{i=1}^n \frac{\Delta t_i}{\tau_x(T_i)} = \sum_{i=1}^n \frac{1}{\tau_x(T_i)} \frac{\Delta t_i}{\Delta T_i} \Delta T_i = 1 \quad (2.20)$$

Here, the first part of the equation was proposed by Scheil and the term $\Delta t_i/\Delta T_i$, in the second part (Umemoto et al.) is the inverse of the cooling rate. By dividing the cooling curve into increasingly smaller steps, the above equation can be expressed as:

$$\int_{T_c}^T \frac{1}{\tau_x(T)} \frac{dt}{dT} dT = 1 \quad (2.21)$$

where, for precipitation reactions, T_c is the solution temperature at which the precipitation time is more than 10^{25} sec (note: at the actual equilibrium solution temperature, the P_s and P_f times are essentially infinite).

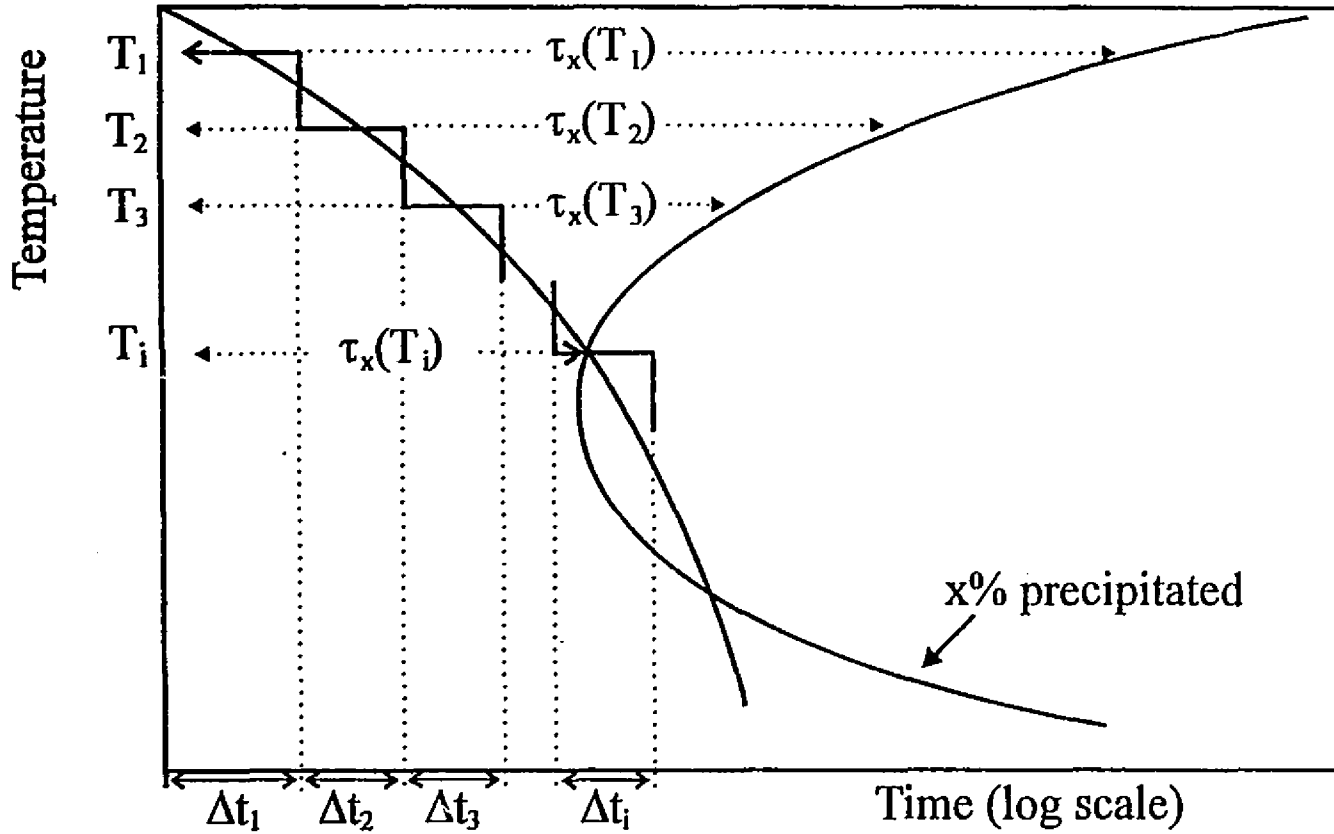


Figure II-17: A diagrammatic representation of the additivity rule concept.

For practical purposes, the cooling curve is divided into 1 °C increments and, at each temperature, τ_x is calculated using the isothermal P_s and P_f times, and Δt_i is also calculated. The continuous cooling precipitation start and finish times can then be determined from the time when the sum of the ratio of each reaction time (Δt_i) to τ_x reaches unity. An example of one such CCP diagram with its corresponding PTT diagram is shown in Figure II-18, as calculated by Park using isothermal data. This figure shows that precipitation is delayed during continuous cooling, since, the CCP curve is shifted down and to the right (i.e. to lower temperatures and longer times) as compared to the PTT curves. The reason for this is that, during continuous cooling, much higher degrees of supercooling are needed to initiate precipitation. As a first approximation, it is reasonable to assume that the degree of supercooling is directly proportional to the cooling rate. This implies that there will be a larger deviation (both horizontally and vertically) between CCP behaviour and isothermal behaviour in a high cooling rate region than in a lower cooling rate region.

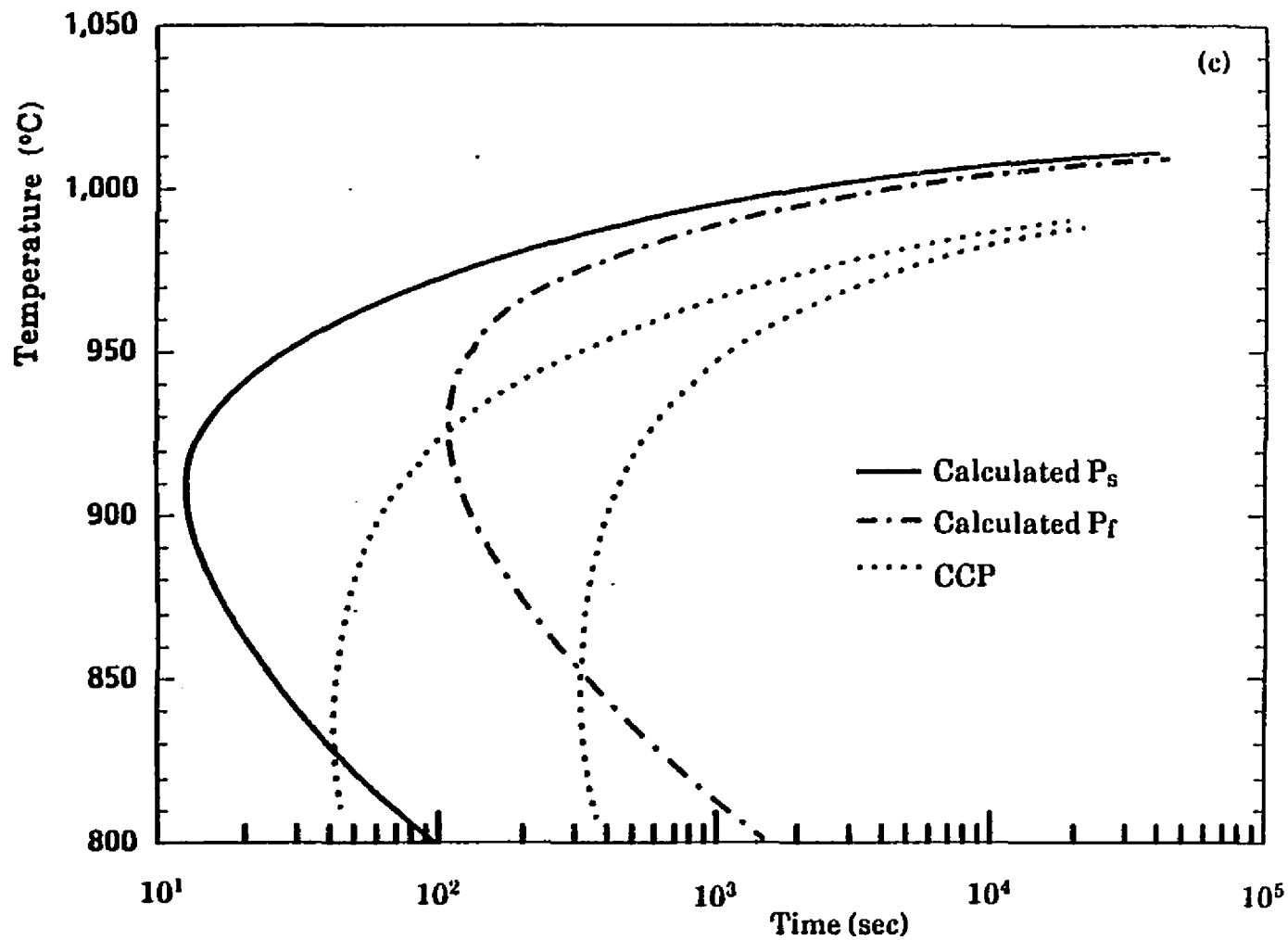


Figure II-18: Calculated CCP behaviour from PTT data [86].

CHAPTER III

EXPERIMENTAL PROCEDURE

III. 1. Stainless steel compositions

The chemical compositions of the steels investigated in this work, for the purpose of determining the CCP behaviour, are given in Table III-1. The unstabilized steel, designated here as - IF Reference mat'l, was initially used for reference purposes. These steels were kindly prepared and donated by Armco Research as 13 mm thick hot rolled plates.

Table III-1: Chemical compositions of the steels tested (wt.%)

Stainless Steel	C	N	Nb	Ti	Cr
A- Std. Ti Stab.	0.006	0.013	<.01	0.25	11.1
B- IF Nb Stab.	0.003	0.005	0.2	0.006	11.1
C- IF Reference mat'l	0.002	0.004	<.01	<.006	11.2
D- IF Ti Stab.	0.002	0.005	<.01	0.23	11.1
E- IF Ti & Nb Stab.	0.003	0.004	0.1	0.09	11.1

with: 0.5%Si, 0.2%Ni, 0.04%Mo, 0.02%P, 0.003%S, 0.3%Mn, 0.06%Cu, 0.01%Al

III. 2. Specimen preparation

Compression specimens, 11.4 mm in height and 7.6 mm in diameter, were machined from the as-received plates with their cylindrical axes aligned along the rolling direction. Thin sheets of mica covered with boronitride lubricant were placed on the end faces of the specimen to reduce friction at the specimen/tool interfaces, thus reducing bulging and facilitating quenching of the specimen at the end of the test. Shallow

bulging and facilitating quenching of the specimen at the end of the test. Shallow concentric grooves were machined into the specimen ends to help retain the lubricant [95] (see Figure III-1).

III. 3. Mechanical testing equipment

All the tests were performed on a high temperature, servo-hydraulic, computer controlled MTS machine. The external view of the setup is shown in Figure III-2.

III. 3.1. MTS automated testing equipment

The continuous cooling compression behaviour was measured using a model 810 MTS machine. The setup consisted of a load frame and hydraulic power supply, a closed loop servohydraulic system and computerized outer loop system, and a radiant furnace and temperature controller/programmer. These components are described in the following sections.

III. 3.2. Load frame and hydraulic power supply

The maximum capacity of the load frame is rated at 25kN (under static loading). A hydraulic power supply is used to supply hydraulic fluid at a pressure of 20 MPa to the servovalve and the hydraulic service manifold for actuator motion.

III. 3.3. Closed loop and outer loop system

The closed loop servohydraulic system is shown in Figure III-3. This schematic diagram reveals a continuous path that compares the differences between the command signal and the feedback signal (i.e. a comparison of what the actuator was instructed to do, to what the actuator is actually doing), and this difference is the DC error. Both the polarity and the magnitude of the DC error are used to determine the direction and the

Chapter III - Experimental Procedure

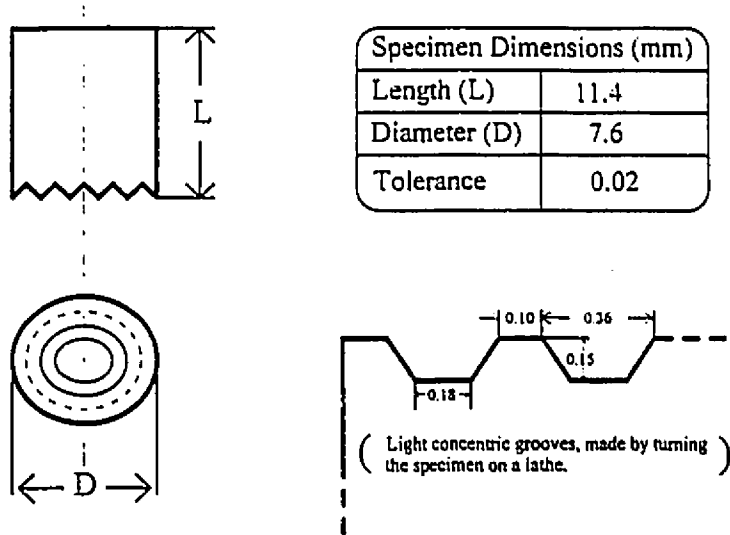


Figure III-1: Compression specimen geometry and groove design.



Figure III-2: An exterior view of the equipment setup: A) MTS load frame; B) MTS electronics; C) VT-240 graphics terminal and LA-50 printer; D) radiant furnace and compression tools; E) temperature controller/programmer; and F) argon gas supply.

amount that the servovalve spool opens, which then controls the direction and the flow rate of the hydraulic fluid through this servovalve. Thus, the actuator moves until the feedback signal reaches the command signal (i.e. when the DC error is zero, the servovalve spool stops moving). The force and displacement of the actuator are then measured by the load cell and the linear variable differential transformer (LDVT) (note: the operating range of these transducers can be controlled to accommodate different testing requirements). These transducers supply the excitation voltage to their respective conditioners, and also a control mode feedback signal is generated. This signal and the command signal are compared at the summing junction, where the resulting DC error is applied to the valve controller to become the control signal.

The computerized outer loop system is shown in Figure III-4. This MTS system is interfaced with a Digital Equipment Corporation PDP-11 microcomputer, a VT-240 graphics terminal, a LA-50 printer, and the electronic controls, via a Series 468 processor unit.

III. 3.4. Furnace, temperature controller/programmer, and compression tools

For continuous cooling compression testing, a radiant furnace (model E4-10, manufacture by Research Inc.) with a power rating of 16 kW, utilizing four equispaced tungsten filament lamps, was used. The water cooled furnace was mounted on the columns of the MTS load frame (to ensure that the specimen and the compression tools were coaxial with the central axis of the furnace), and interfaced with the Micristar Digital controller/programmer (Figure III-5). The temperature was measured and controlled by a K-type (closed ended) chromel/alumel thermocouple in contact with the compression specimen. The anvils and the specimen were enclosed in a transparent quartz tube with an argon atmosphere, in order to prevent high temperature oxidation.

The compression tools (or anvils), used in these experiments, were made of Inconel. These anvils were 130 mm in length and 32 mm in diameter, and were

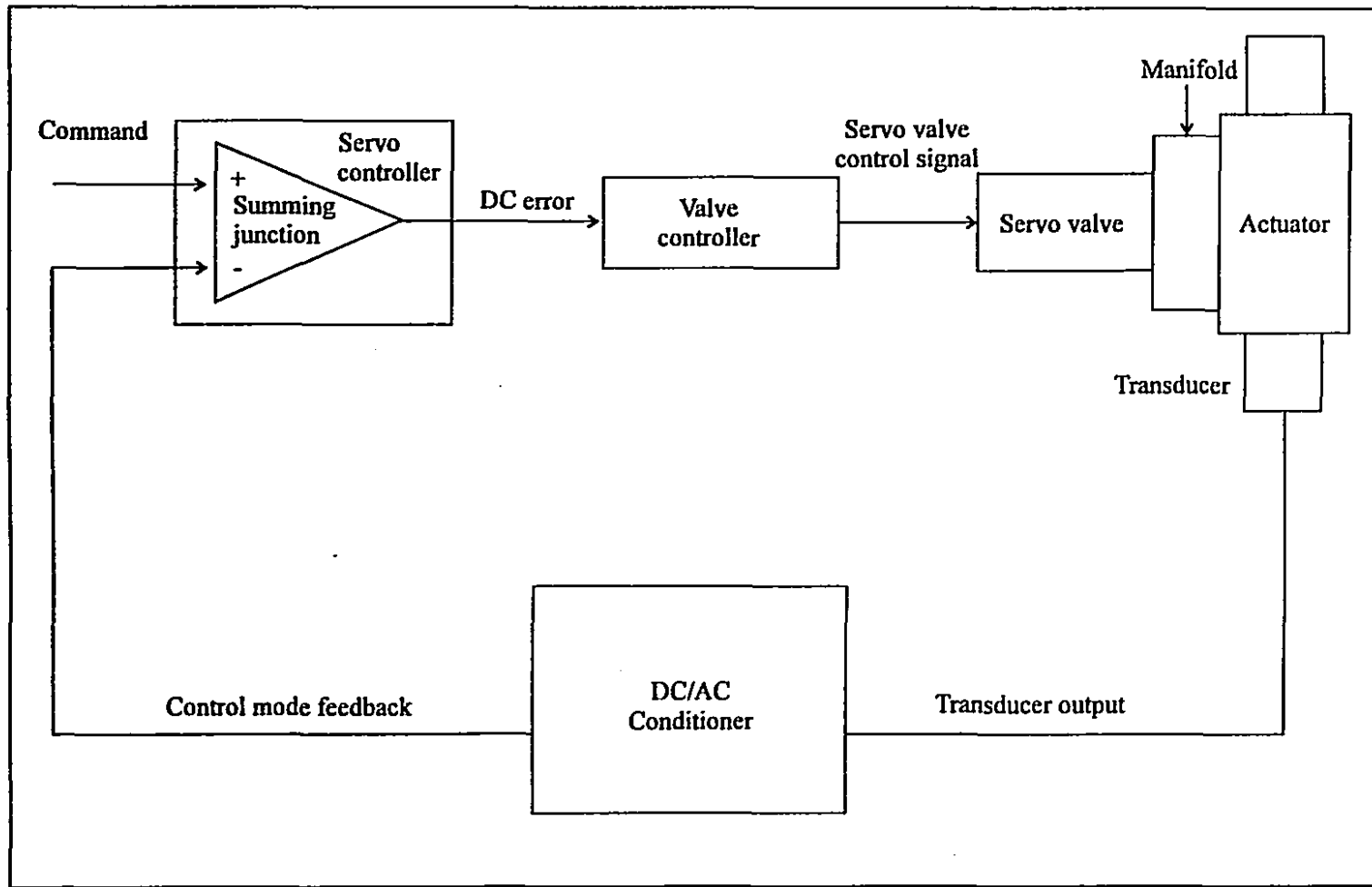


Figure III-3: Closed loop servohydraulic system.

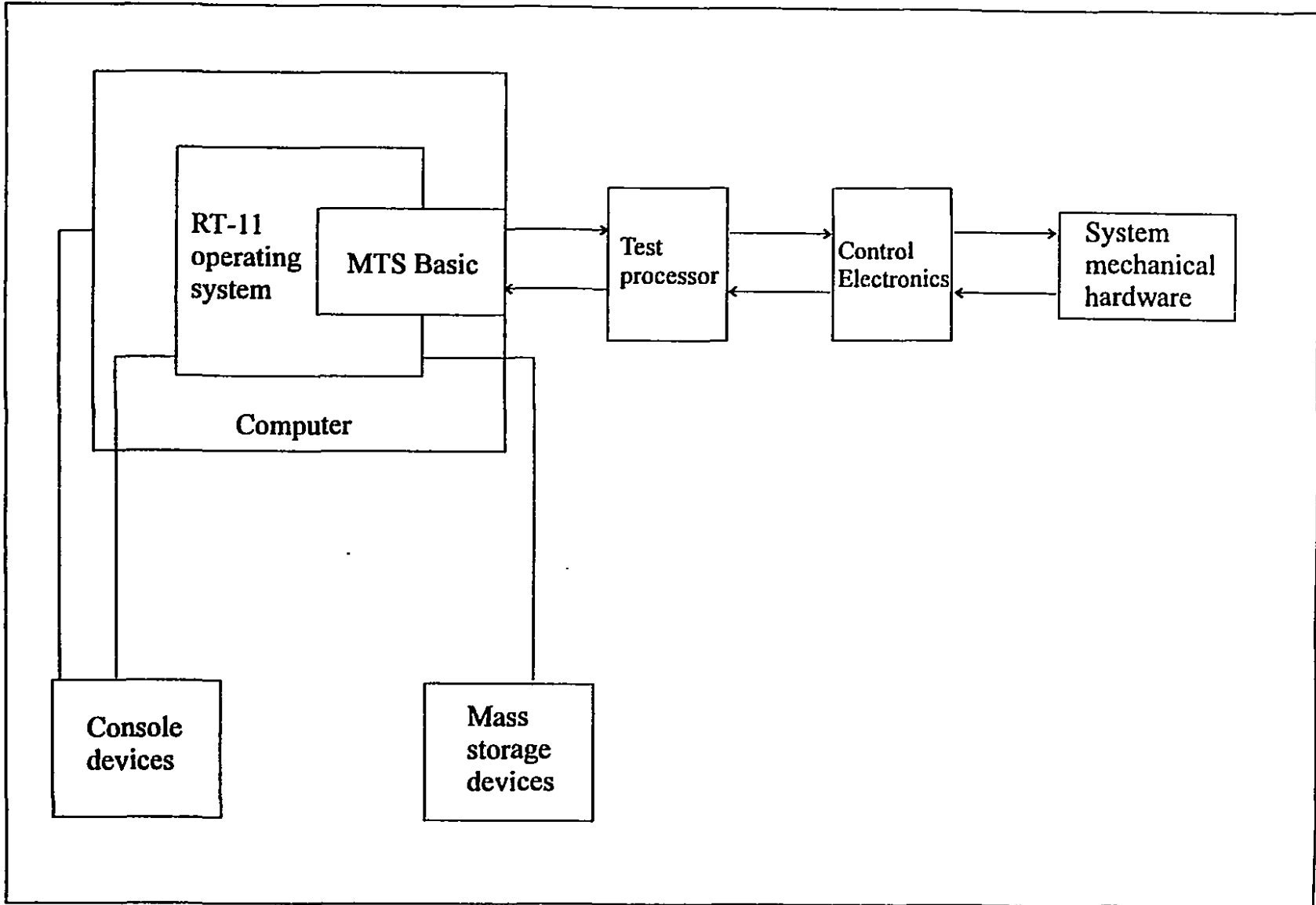


Figure III-4: Computerized outer loop system.



Figure III-5: View of the radiant furnace and experimental setup: 1) radiant furnace; 2) Inconel anvils; 3) actuator; 4) load cell; 5) temperature controller; 6) quenching can.

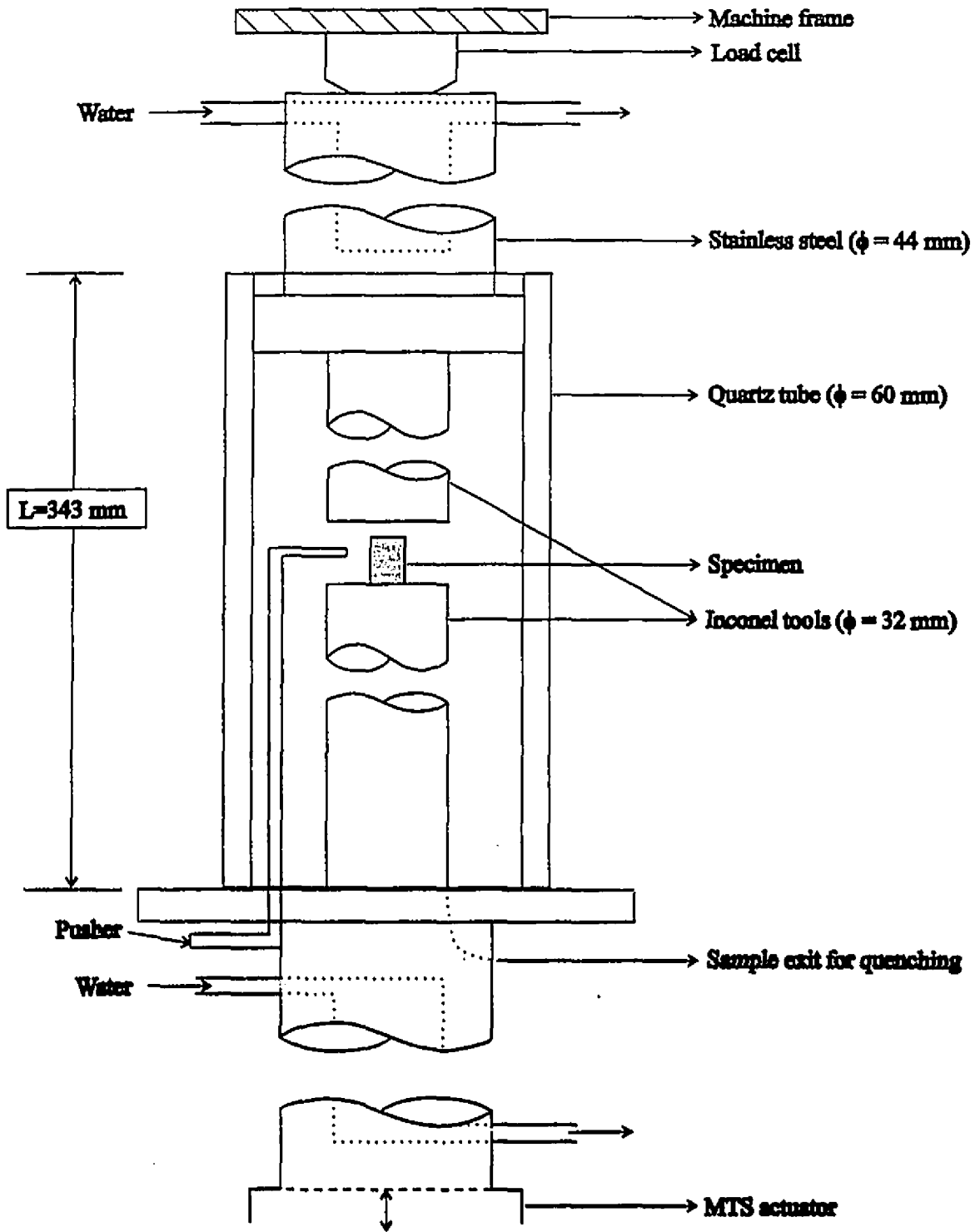


Figure III-6: Schematic drawing of the MTS load train.

connected to upper and lower water cooled stainless steel tubes, which in turn, were connected to the load cell and to the actuator, respectively. This is shown in Figure III-6. In order to interrupt and quench the specimens, a high carbon steel lever was used. The specimen fell through a hole made in the lower support between the inside wall of the quartz tube and the lower tool. After falling, the specimen was caught and quenched in a container of cold water.

III. 4. Continuous cooling compression testing

The test method employed for determination of the CCP behaviour is that of continuous cooling compression testing. These tests have recently been refined by Zarei Hanzaki et al. [96] for determining any microstructural changes that take place during cooling. The following sections outline the heating and deformation schedules utilized, and the anvil contraction rate. The rationale behind these tests will be discussed in the Results section.

III. 4.1. Heating and deformation schedules

For all of the continuous cooling compression (CCC) tests, the samples were heated and deformed in an argon atmosphere according to one of the schedules shown in Figs. III-7,8,9 or 10. Figure III-7 illustrates the most commonly used schedule for the CCC tests. Here the sample was heated from room temperature to 1200°C at 2°C/sec, held for 10 minutes and then cooled at 0.5°C/sec while being compressed at a constant strain rate of $\dot{\epsilon} = 3 \times 10^{-4} \text{ s}^{-1}$. In the schedule shown in Figure III-8, the only difference was that the sample was heated to 1300°C at 2°C/sec, and then held for 15 minutes. The heating and deformation schedule shown in Figure III-9 is similar to that of Figure III-7, with the exception that the sample was heated to 1200°C, 1000°C or 950°C and then held for 1 minute instead of 10 minutes. Figure III-10 represents a heating and deformation schedule which employs different cooling rates for continuous compression. This

schedule was used for the construction of continuous-cooling precipitation (CCP) curves, which will be discussed in more detail later in this thesis.

III. 4.2. Determination of tool length contraction

During CCC testing, the Inconel anvils undergo contraction. This contraction affects both the strain rate and the true stresses exerted on the sample, which, in turn, changes the deviations observed in the flow curves. Therefore, it was necessary to determine the contraction behaviour of the anvils, in the test temperature range (1200°C - 600°C), for the different cooling rates used. An alumina sample was used for a continuous-cooling test under a constant load of 5 kg, whereby no deformation occurs. The changes in apparent strain can be directly related to anvil contraction (this is shown in the Results section IV. 1.). The anvil contraction with temperature is shown in Figure III-11 for the four cooling rates employed (0.25, 0.5, 1 and 2°C/sec). As was expected, this figure shows that the anvil contraction is linear and the contraction rate increases with increasing cooling rate. The contraction rate was determined for each cooling rate, and the raw data of the CCC tests were normalized, thus filtering out the erroneous contraction effects (the exact calculations used are outlined in the Results section).

III. 5. Micro and submicro-structural analysis

III. 5.1. Metallography

The quenched compression specimens were sectioned in half parallel to the deformation axis. One half was mounted in bakelite, and then ground using 120-600 grit grinding paper followed by polishing with a suspension of 0.03µm alumina powder in water. At this point the specimen was etched for 1 min. using a ferritic stainless steel etchant to reveal the grain boundary constituents (etchant [97]: $\frac{1}{3}$ water + $\frac{1}{3}$ nitric acid +

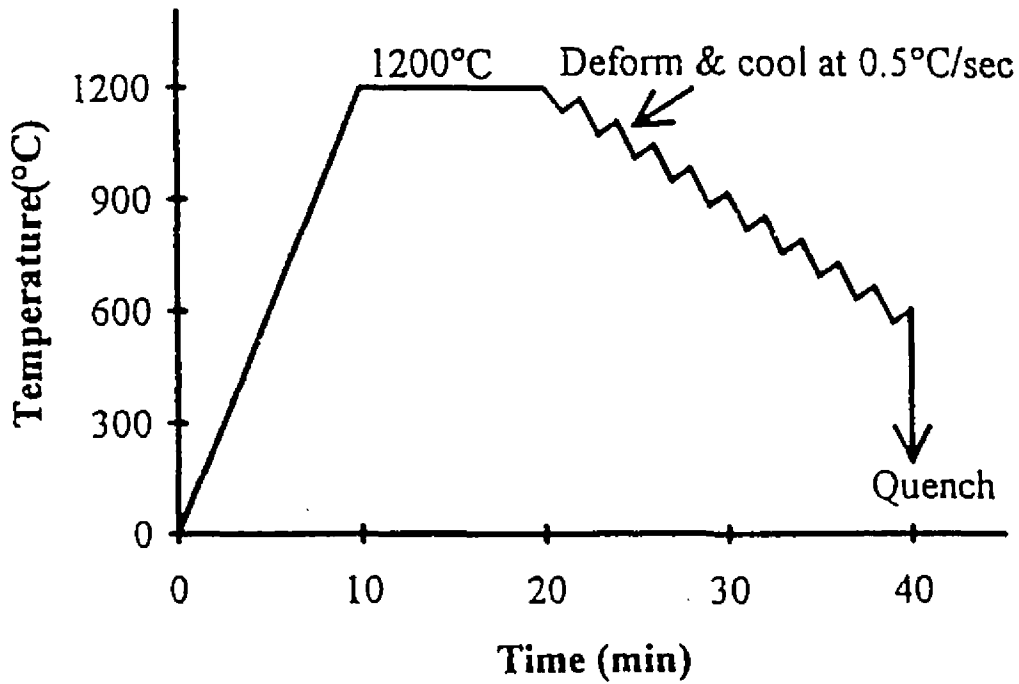


Figure III-7: Heating and deformation schedule for 1200°C CCC tests.

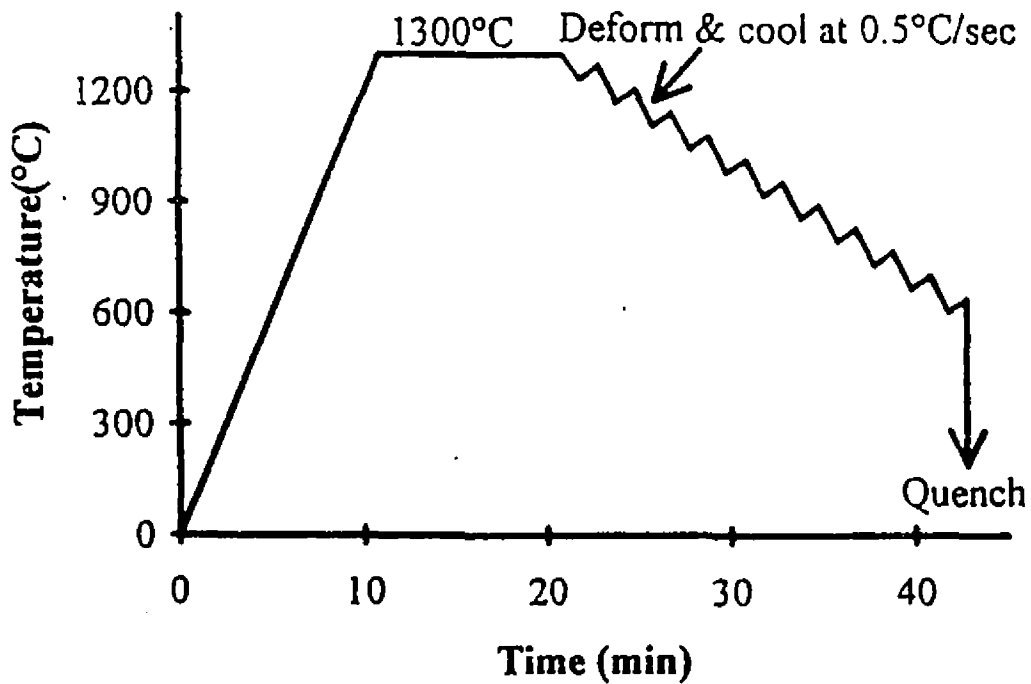


Figure III-8: Heating and deformation schedule for 1300°C CCC tests.

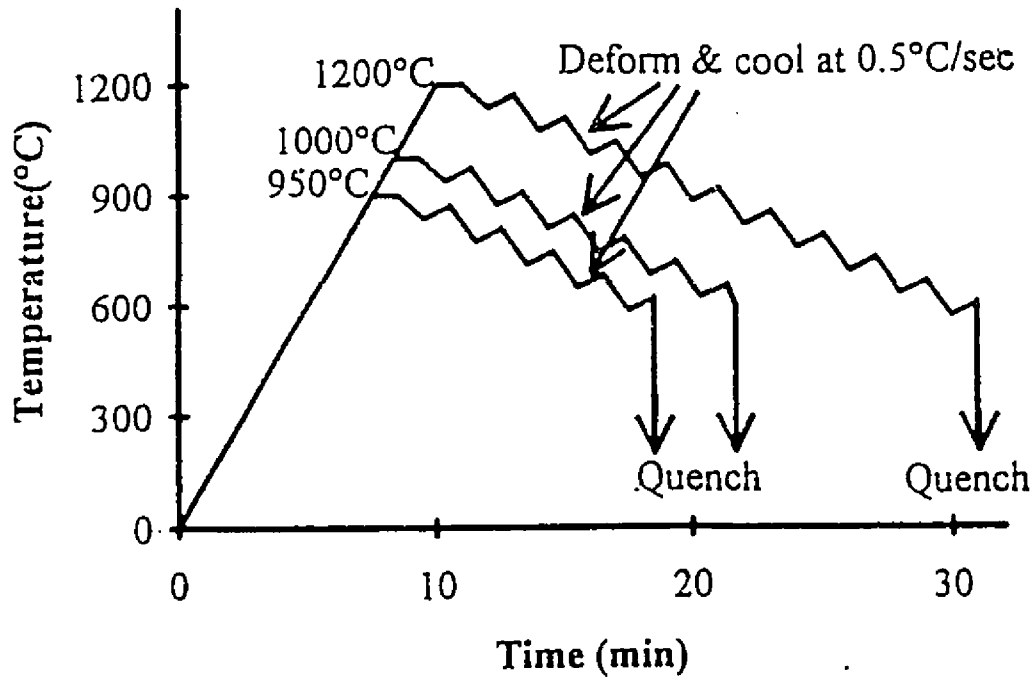


Figure III-9: Heating and deformation schedule for 1200, 1000 and 950°C CCC tests.

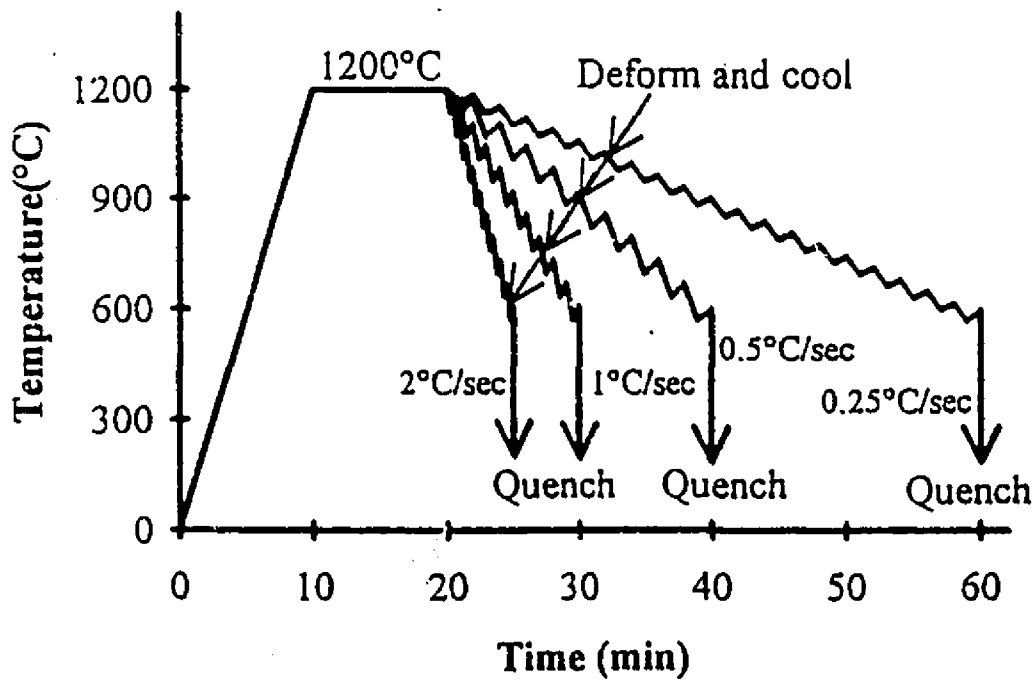


Figure III-10: Heating and deformation schedule for CCC tests at a series of cooling rates.

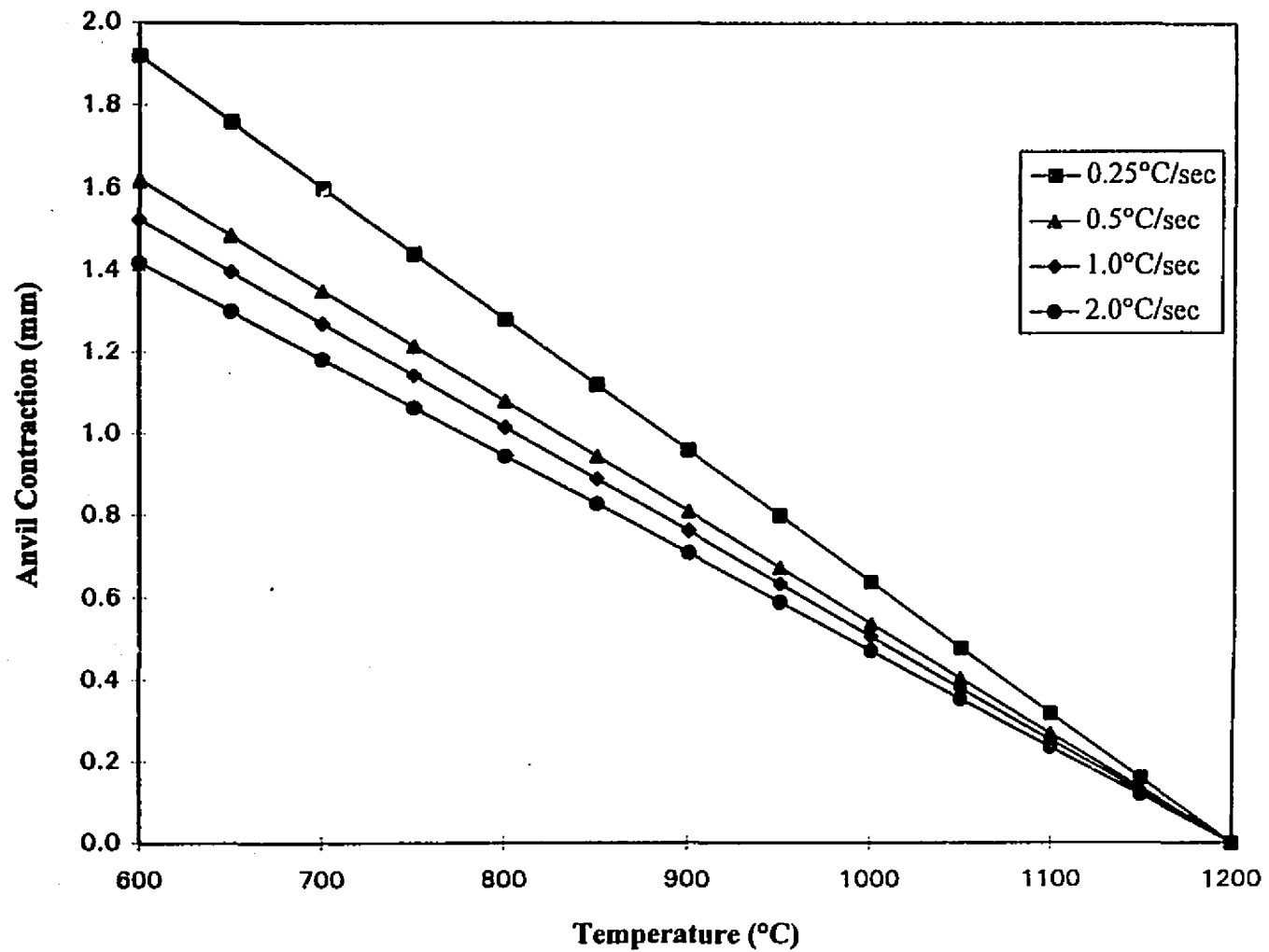


Figure III-11: Anvil contraction versus temperature for cooling rates of 0.25, 0.5, 1 and 2°C/sec.

$\frac{1}{3}$ hydrochloric acid). The microstructure was then photographed using a Neophot 21 optical microscope.

III. 5.2. Thin foil preparation

Several of the quenched specimens were used to make thin foils for examination under the TEM. Thin slices of the material were cut lengthwise along the centerline using a low speed diamond saw, to approximately 2mm thick. These samples were glued to Plexiglass and then mechanically ground down, on silicon carbide grinding paper, to a final thickness of less than 100 microns. In order to remove the samples from the Plexiglass they were immersed into an ultrasonic bath. With the aid of a punch, a three millimeter disk was produced.

The disks were placed in a sample holder, and then inserted into a Struers-Tenupol-3 jet electropolisher. Electropolishing proceeded until perforation, which was detected by a photocell, which sounded an alarm. The electrolyte bath was a mixture of 20% perchloric acid in methanol, which was cooled, using liquid nitrogen, to -20°C (or lower). The electropolishing took about 30 sec for each disk at an intermediate jet flow rate (7-8 setting on the Tenupol), a current density of 3 mA/cm^2 , and a voltage of about 15V. Immediately after perforation was detected, the samples and sample holder were removed from the bath, and placed in successive baths of alcohol and then water. The discs were then rinsed with methanol and subsequently dried on filter paper. Finally, the discs were examined under an optical microscope to ensure that both sides of the sample were polished and that the hole was jagged. After these operations, the discs were placed in separate protective plastic capsules.

III. 5.3. Transmission electron microscopy (TEM)

The thin foils were examined in a JEOL 100CX transmission electron microscope operating at 80kV or 100kV.

CHAPTER IV

RESULTS

IV. 1. Anvil contraction

IV. 1.1. Effect on strain and strain rate

The experimental data are acquired and converted to true stress and true strain via the initial length and diameter and the final length. The initial dimensions, strain and strain rate are entered into the program before the tests starts. Once the test starts, the actuator position is set to 'zero'; therefore at the end of the test the displacement of the actuator effectively indicates the final specimen length, and by conservation of volume, the final diameter can be determined. This 'back' calculation method is incorrect inasmuch as the specimen and the anvils are contracting during the test (due to continuous cooling). This results in lower true stresses and lower overall strains and strain rates. The following is a derivation of this effect.

Consider a compression test with initial (room temperature) height H_0 and diameter d_0 , with a requested strain (ϵ_r) and strain rate ($\dot{\epsilon}_r$) of X and Y sec^{-1} , respectively (i.e. the strain and strain rate entered into the program, that determines the amount and rate at which the actuator moves). Let ΔA and ΔL equal the total contraction of the anvils and the specimen, respectively. Then, the equivalent strain due to ΔA is:

$$\epsilon_{\Delta A} = \Delta A / H_0 \quad (4.1)$$

and the equivalent strain due to ΔL is:

$$\epsilon_{\Delta L} = \Delta L / H_0 \quad (4.2)$$

Now, by taking into account contraction effects, the actual applied strain rate is:

$$\dot{\epsilon}_a = \dot{\epsilon}_r - (\epsilon_{\Delta A} + \epsilon_{\Delta L}) / t = \dot{\epsilon}_r - \left[\frac{(\Delta A + \Delta L)}{H_0 t} \right] \quad (4.3)$$

where t is the time of the test in seconds.

Equation (4.3) shows that the actual total strain on the specimen (ϵ_{total}) is diminished by the contraction effects:

$$\epsilon_{total} = \dot{\epsilon}_a t = \dot{\epsilon}_r t - \left[\frac{(\Delta A + \Delta L)}{H_0} \right] \quad (4.4)$$

and the total true strain is:

$$\epsilon_T = \ln(\epsilon_{total} + 1) \quad (4.5)$$

Also, the instantaneous specimen height, H_i , is related to the instantaneous strain, ϵ_i , during compression, as follows:

$$H_i = H_0(1 - \epsilon_i) \quad (4.6)$$

Since, ϵ_i is lower than the requested strain at any given point during the test (as shown in equation (4.4)), the cross-sectional area is not increasing as fast as expected (i.e. without considering contraction), and this results in a true stress, σ_T , that is higher than calculated by the program (σ_{Tc}), and displayed as the output. Equation (4.7) shows how to calculate the actual true stress, σ_T , on the specimen, from the initial parameters and the calculated total strain, ϵ_{total} .

$$\sigma_T = \frac{F}{A_0} \cdot (\epsilon_{total} + 1) \quad (4.7)$$

Therefore, this derivation proves that the effect of contraction is to lower the true stress (as displayed in the output), and lower the actual true strain and strain rate. The next section describes how the σ_T , ε_T and $\dot{\varepsilon}_a$ were determined.

IV. 1.2. Alumina correction

Since the temperature of a particular point along an anvil depends on its axial displacement relative to the specimen (i.e. the anvil is hottest at the point of contact with the specimen and its temperature decreases with increasing distance away from the specimen), it is mathematically complex to determine the actual contraction rate of the anvils. Therefore, an alumina dummy specimen was used to monitor their total shrinkage. This test is described in section III.4.2, and the results were illustrated graphically in Figure III-11. It can be shown that the total anvil contraction (ΔA) is related to this test via the following equation:

$$\Delta A = \Delta A_{\text{test}} - \Delta a = \Delta A_{\text{test}} - \alpha_{\text{al}} H_{\text{o,al}} \Delta T \quad (4.9)$$

where ΔA_{test} is the total contraction measured during the alumina test for a particular cooling rate, Δa is the change in length of the alumina specimen due to contraction, α is the coefficient of thermal expansion, and $H_{\text{o,al}}$ is the initial height of the alumina specimen. The alumina specimen actually contracts at different rates, depending on the cooling rate employed. However, this aspect is not taken into account in the above equation. Nonetheless, this equation is still useful, since the alumina contraction is negligible (as will be shown below).

Chapter IV - Results

Figure III-11 shows that, as the cooling rate increases, the total contraction over the same temperature range decreases. This indicates that the contraction rate is slower than the cooling rate. Table IV-1 shows the percent decrease in total contraction as the cooling rate is increased over the range 0.25 to 2.0 °C/sec.

Table IV-1: Percent decrease in anvil contraction due to increase in cooling rate.

Cooling rate (°C/sec)	Total contraction (mm)	% decrease, in contraction, due to cooling rate increase:
0.25	$\Delta A_{\text{test}} = 1.92$	(0.25-0.5) = 15.6 %
0.5	$\Delta A_{\text{test}} = 1.62$	(0.5-1.0) = 6.8 %
1.0	$\Delta A_{\text{test}} = 1.51$	(1.0-2.0) = 6.0 %
2.0	$\Delta A_{\text{test}} = 1.42$	

This table shows that the total contraction, anvils plus alumina specimen, for the slowest cooling rate (0.25°C/sec) is the largest, and that the difference in contraction decreases as the cooling rate increases. Therefore, the contraction of the anvil at 0.25°C/sec is greater than that achieved at higher cooling rates. In a similar way, the maximum contraction of the alumina specimen is also assumed to take place at a cooling rate of 0.25°C/sec. That is, the amount of contraction by the alumina specimen, during cooling at rates of 0.5, 1.0 and 2°C/sec, is taken to be less than or equal to the contraction at 0.25°C/sec.

The following table summarizes the maximum possible contraction of the alumina specimen for all the cooling rates employed; it also contains ΔA :

Table IV-2: Δa and ΔA for all the cooling rates.

Cooling rate (°C/sec)	$\Delta a = \alpha_{\text{al}} H_{\text{o,al}} \Delta T$	Δa (mm)	ΔA (mm) ($\Delta A_{\text{test}} - \Delta a$)
0.25	$\Delta a_{0.25^\circ\text{C}}$	0.06	1.86
0.5	$\Delta a_{0.5^\circ\text{C}} \leq \Delta a_{0.25^\circ\text{C}}$	<0.06	≈1.56
1.0	$\Delta a_{1.0^\circ\text{C}} \leq \Delta a_{0.5^\circ\text{C}} \leq \Delta a_{0.25^\circ\text{C}}$	<0.06	≈1.45
2.0	$\Delta a_{2.0^\circ\text{C}} \leq \Delta a_{1.0^\circ\text{C}} \leq \Delta a_{0.5^\circ\text{C}} \leq \Delta a_{0.25^\circ\text{C}}$	<0.06	≈1.36

note: $\alpha_{\text{al}} = 8.8 \times 10^{-6} / ^\circ\text{C}$, $H_{\text{o,al}} = 11.4$ mm, and $\Delta T = 600^\circ\text{C}$.

Now, since the alumina specimen had the same dimensions as the actual compression specimens (i.e. 11.4 x 7.6 mm) and α_{al} is close to $\alpha_{f.s.s.}$ (8.8×10^{-6} & $10.4 \times 10^{-6}/^{\circ}\text{C}$ respectively), there is only a slight percent difference between ΔL and Δa ; that is:

$$\%diff = \left(\frac{\Delta L - \Delta a}{\Delta L} \right) = \left(\frac{L_i \Delta T (\alpha_{f.s.s.} - \alpha_{al})}{L_i \Delta T (\alpha_{f.s.s.})} \right) \quad (4.10)$$

$$\%diff = \left(\frac{10.4 \times 10^{-6} - 8.8 \times 10^{-6}}{10.4 \times 10^{-6}} \times 100\% \right) = 15.4\%$$

therefore,

$$\Delta L = 115.4\% \Delta a \quad (4.11)$$

The difference between ΔL and Δa is negligible, since Δa is on average only 3.8% of ΔA_{test} . Therefore, ΔL will increase the 3.8% correction by 15.4% (i.e. up to 4.4% of ΔA_{test}).

So, now:

$$\begin{aligned} (\Delta A + \Delta L) &= \Delta A_{test} - \Delta a + \Delta L & (4.12) \\ &= \Delta A_{test} - 3.8\% \Delta A_{test} + 4.4\% \Delta A_{test} \\ &= \Delta A_{test} - 0.6\% \Delta A_{test} \\ &\approx \Delta A_{test} \text{ (i.e. within experimental error.)} \end{aligned}$$

Therefore, equations (4.5) and (4.7) can be solved, using equation (4.13) and (4.14) below. In this way, the experimental data can be corrected to take into account tooling and specimen contraction effects.

$$\dot{\epsilon}_a = \dot{\epsilon}_r - \left[\frac{(\Delta A_{test})}{H_o t} \right] \quad (4.13)$$

$$\varepsilon_{\text{total}} = \dot{\varepsilon}_a t = \dot{\varepsilon}_r t - \left[\frac{(\Delta A_{\text{test}})}{H_0} \right] \quad (4.14)$$

IV. 2. Continuous cooling curves

IV. 2.1. General interpretation

The data obtained from the CCC tests concern the variation of flow stress with temperature. The basic idea is to relate changes in the flow stress behaviour to changes in the microstructure. Thus, before a CCC test can be interpreted, the expected effect of temperature on flow stress (in the absence of recrystallization or precipitation) is required as a reference to compare with the actual tests. The expected stress vs temperature curve for a CCC test can be obtained from the constitutive equation for the steady state stress [98], shown below.

$$\dot{\varepsilon} = A [\sinh(\alpha\sigma)]^{n'} \exp\left(-\frac{Q}{RT}\right) \quad (4.15)$$

or rearranging:

$$\sigma = \frac{\sinh^{-1}(X)}{\alpha}, \text{ where } X = \left[\frac{(\dot{\varepsilon} \exp(Q/RT))}{A} \right]^{1/n'} \quad (4.16)$$

Here σ and $\dot{\varepsilon}$ are the steady state stress and strain rate, respectively, A , n' , α and Q are empirical constants for a given composition, and R is the universal gas constant.

A plot of the stress versus temperature relation between 1200°C and 600°C obtained using the above equation with a constant strain rate of $\dot{\varepsilon} = 3 \times 10^{-4} \text{ s}^{-1}$ is presented in Figure IV-1. The values of the constants for the reference steel in Table III-1 are given

in Ref. [99]. This figure shows that the increase in stress in response to a decrease in temperature is expected to be smooth as long as no new microstructural mechanism intervenes. Therefore, any deviation from this flow behaviour during a CCC test is indicative of the occurrence of a microstructural change. This is the rationale behind the analysis of the CCC tests.

The expected flow curve described above is not really what is expected during a CCC test. This is because the curve described by equation (4.16) is a steady state flow curve. Thus, when comparing this 'expected' curve to an actual CCC curve, the former should start off with a higher flow stress (because there is actually very little strain accumulation at the beginning of a CCC test). Then, when the strain accumulation during the test begins to approach that approximated by the steady state equation (4.16), the steady state curve will serve as an asymptote to the actual test flow curve (see Figure IV-2a, which will be discussed later in section IV. 2.2.1.). In order to use the steady state curve as a 'base' curve, the starting stress value must therefore be lowered to that of the actual starting test value, as shown in Figure IV-2b. From this point onward, all references to the expected flow curve are made in the light of the aforementioned adjustment.

IV. 2.2. Standard schedule (an overview)

True-stress vs. temperature CCC curves are presented in Figures IV-3 and IV-4 for the five stainless steels tested. The cooling temperature range for these tests ran from 1200°C to 600°C at 0.5°C/sec, and a strain rate of $3 \times 10^{-4} \text{ s}^{-1}$ was employed (Figure III-7). While cooling from 1200°C to about 900°C, four of the steels displayed similar, nearly parallel, increases in flow stress, see Figure IV-3. These were the two Nb-modified grades (B containing 0.2% Nb, and E with 0.1% Nb + 0.1% Ti) and the two Ti-stabilized grades (A - the standard commercial alloy and D - the modified version containing half the concentration of interstitials). The two former materials display distinctly higher flow stresses because of the strengthening influence of the Nb additions. The fifth steel, which

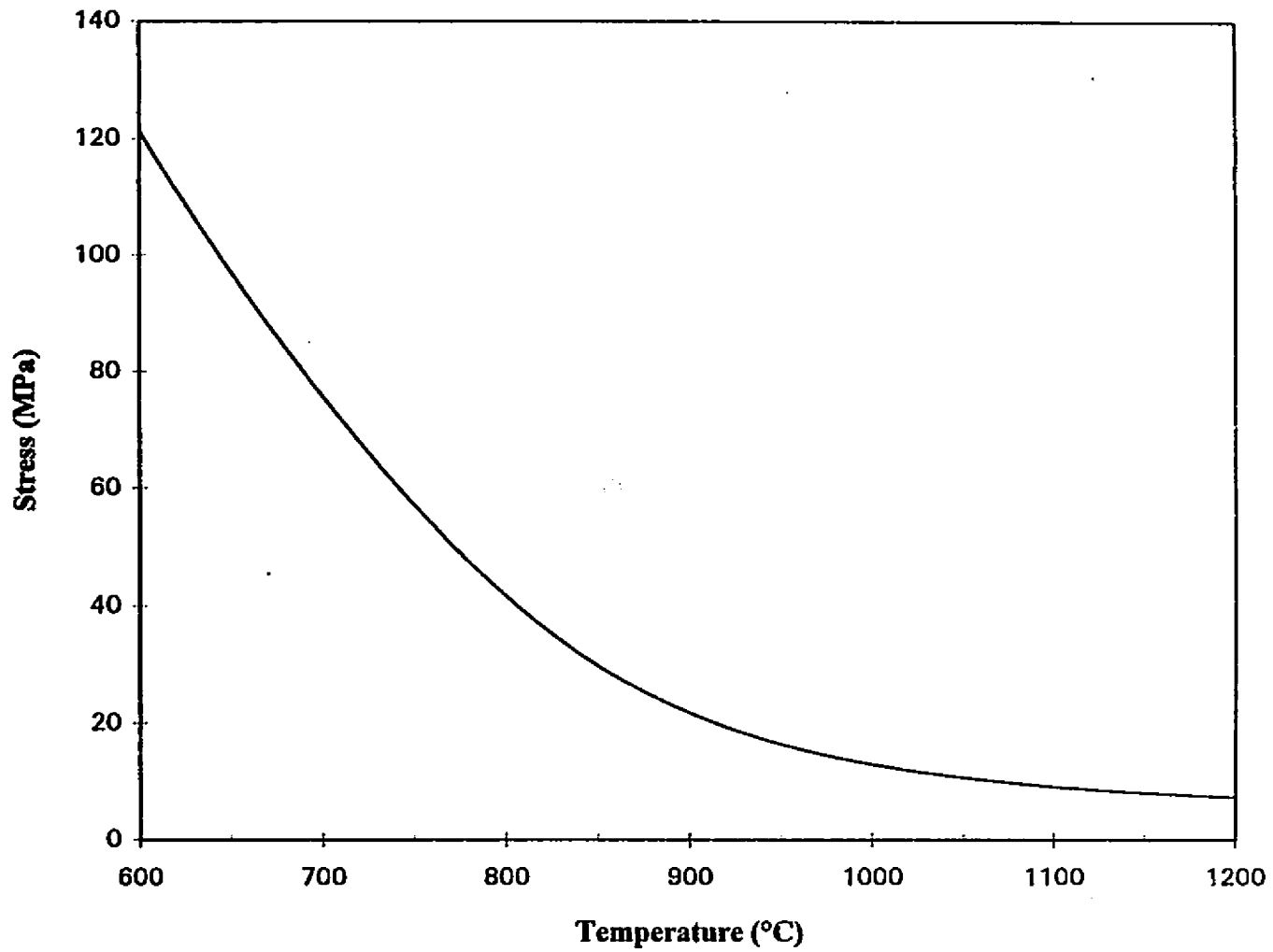


Figure IV-1: Standard stress-temperature behaviour expected in the absence of mechanism change for the CCC tests.

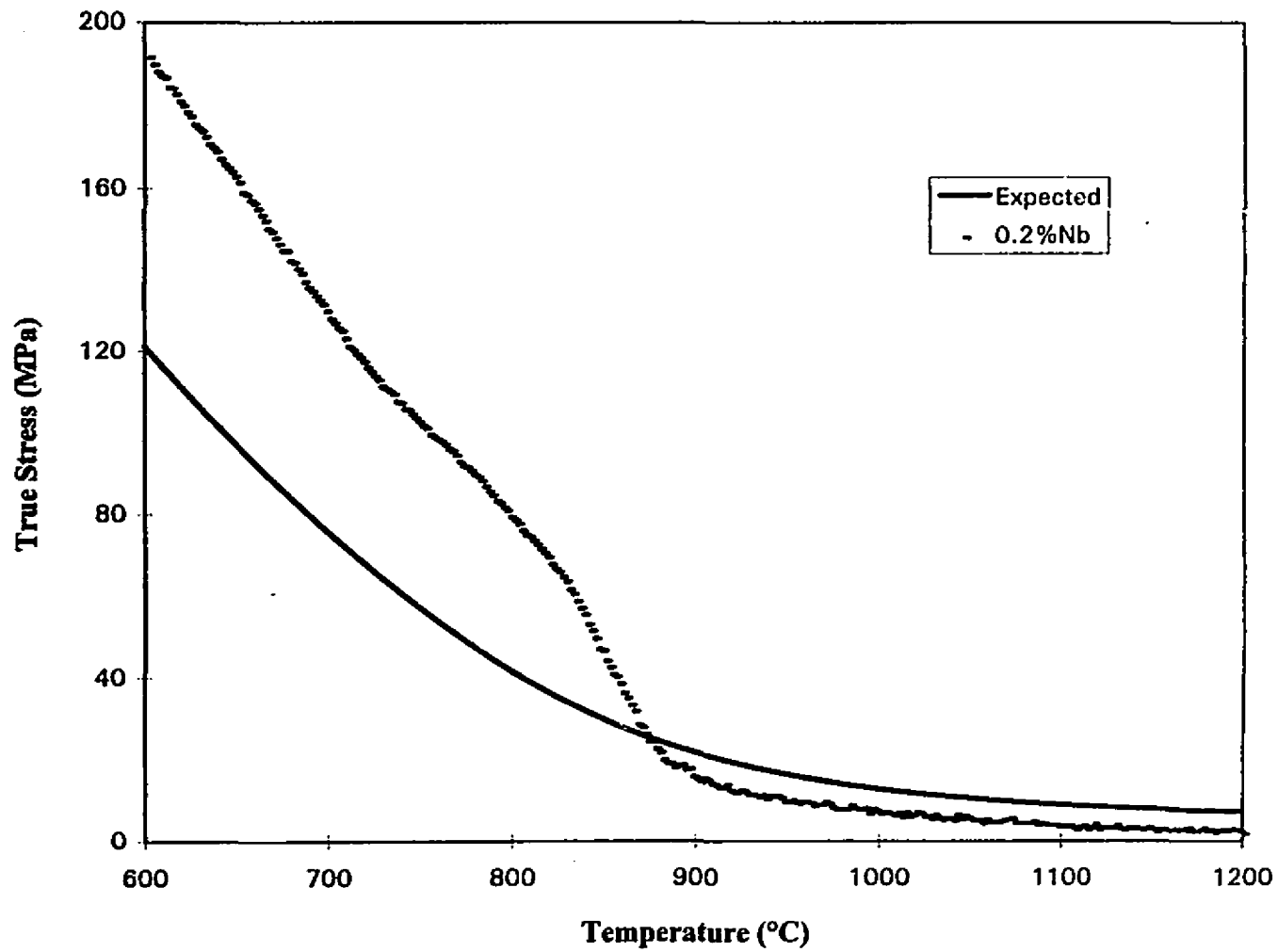


Figure IV-2a: Superposition of the expected curve on the actual behaviour of the 0.2% Nb stainless steel.

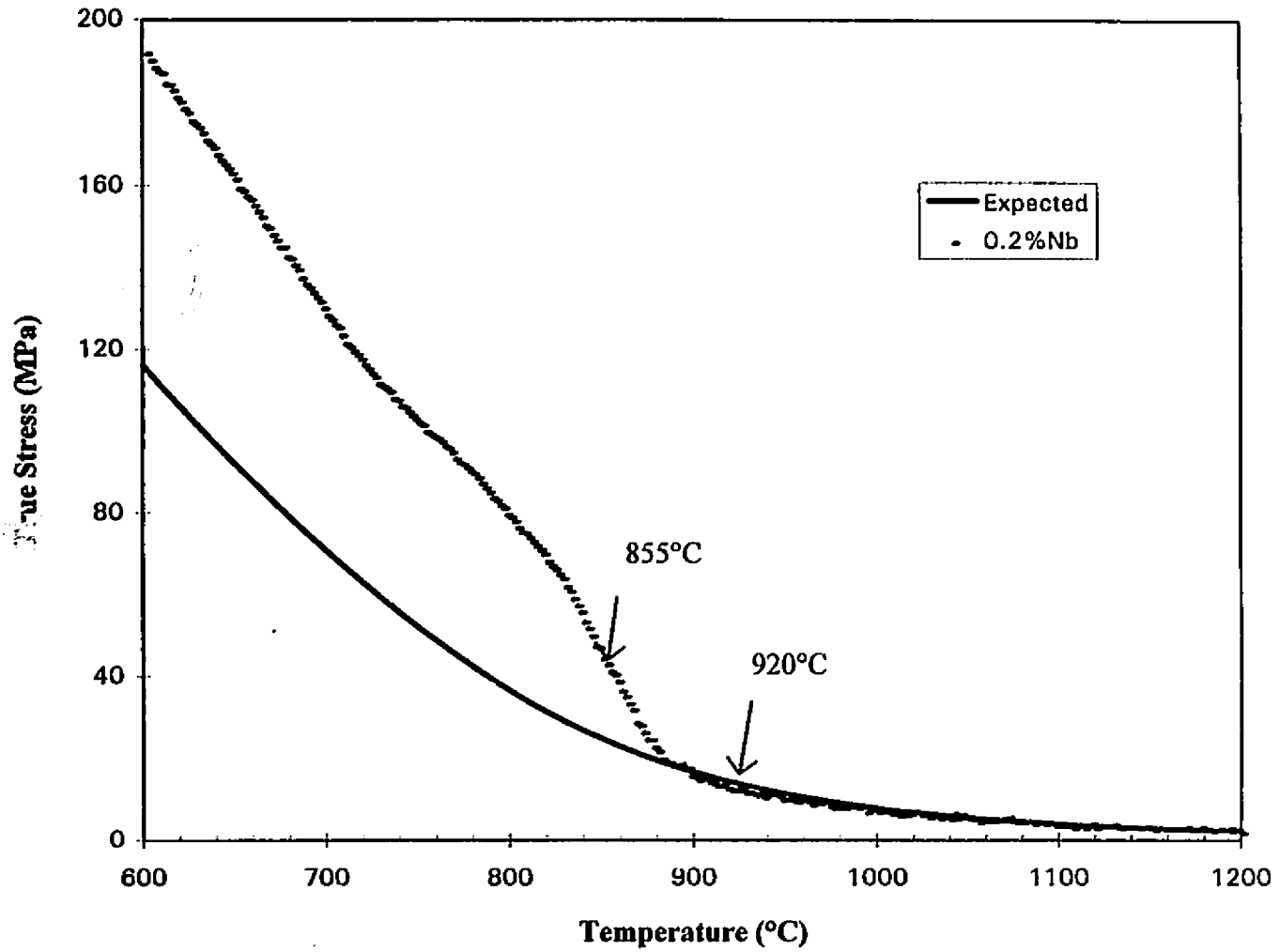


Figure IV-2b: Superposition of the expected curve on the actual behaviour of the 0.2% Nb stainless steel; with the starting flow stress of the steady state flow curve corrected to match that of the actual test.

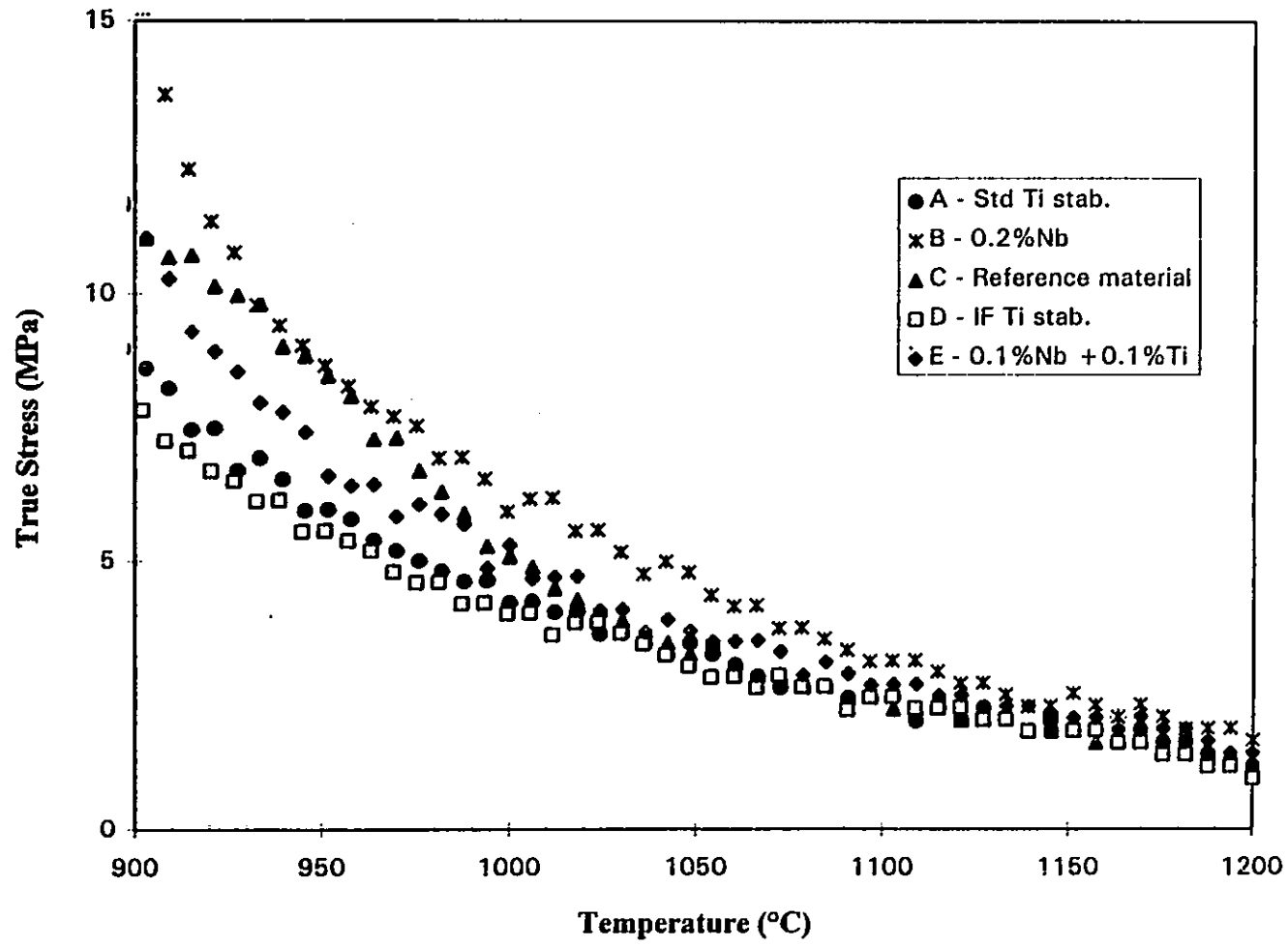


Figure IV-3: True stress vs. temperature for all five steels, 1200-900°C ($\epsilon = 3 \times 10^{-4}$).

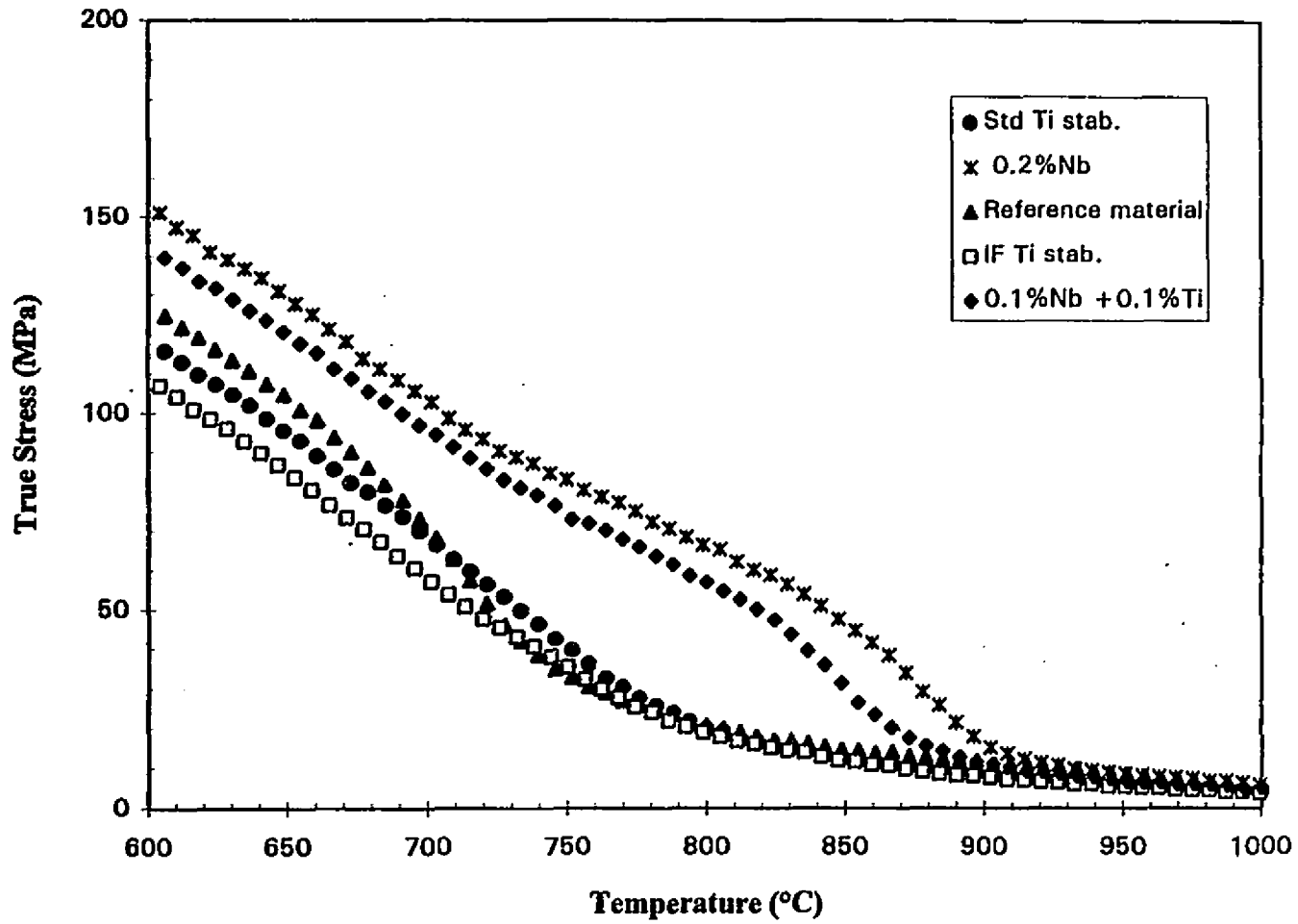


Figure IV-4: True stress vs. temperature for all five steels, 1000-600°C ($\epsilon = 3 \times 10^{-4}$).

increase with decreasing temperature in the temperature range from 1000°C down to about 800°C. The principal difference in composition between this material and the other three IF grades is that neither Nb nor Ti had been added to the reference alloy. The absence of Nb and/or Ti addition allows the carbon and nitrogen to precipitate out at lower temperatures as different species, which may be the cause of this increase in flow stress.

IV. 2.2.1. Calibration

The flow curves presented in Figures IV-3 and IV-4 have not yet been corrected for contraction effects - i.e. they have not been 'normalized'. By applying the equations derived in the previous section to the flow curves of Figure IV-4, the effect of contraction was 'filtered' out. The result of this procedure is shown in Figure IV-5 below. Here we see that the flow stress is higher and the total strain and strain rates are lower (i.e. $\epsilon = 0.22$ and $\dot{\epsilon} = 1.8 \times 10^{-4} \text{ s}^{-1}$ instead of $\epsilon = 0.36$ and $\dot{\epsilon} = 3 \times 10^{-4} \text{ s}^{-1}$, respectively). Since these flow curves are plotted against temperature and not strain, there is no physical shift in the inflection points with respect to temperature. Nonetheless, the total strain at any point has changed. From this point onward, all the flow curves are normalized with respect to contraction.

The flow stress behaviours of the five experimental steels over the temperature range from 1000°C down to 600°C are illustrated in Figure IV-5. Here, the distinct behaviour of the two Nb - containing grades is of particular interest. By superimposing the expected flow curve onto the one for the higher Nb (0.2%) material, see Figure IV-2b, it is apparent that this steel begins to deviate from the expected curve at about 920°C, which is a slightly higher temperature than that displayed by the lower Nb (0.1%) material (900°C, shown here in Figure IV-6). By contrast, the Ti addition of 0.1% seems to have much less influence on the flow behaviour than the comparable Nb addition. The flow stresses in the Nb containing materials increase relatively rapidly down to about

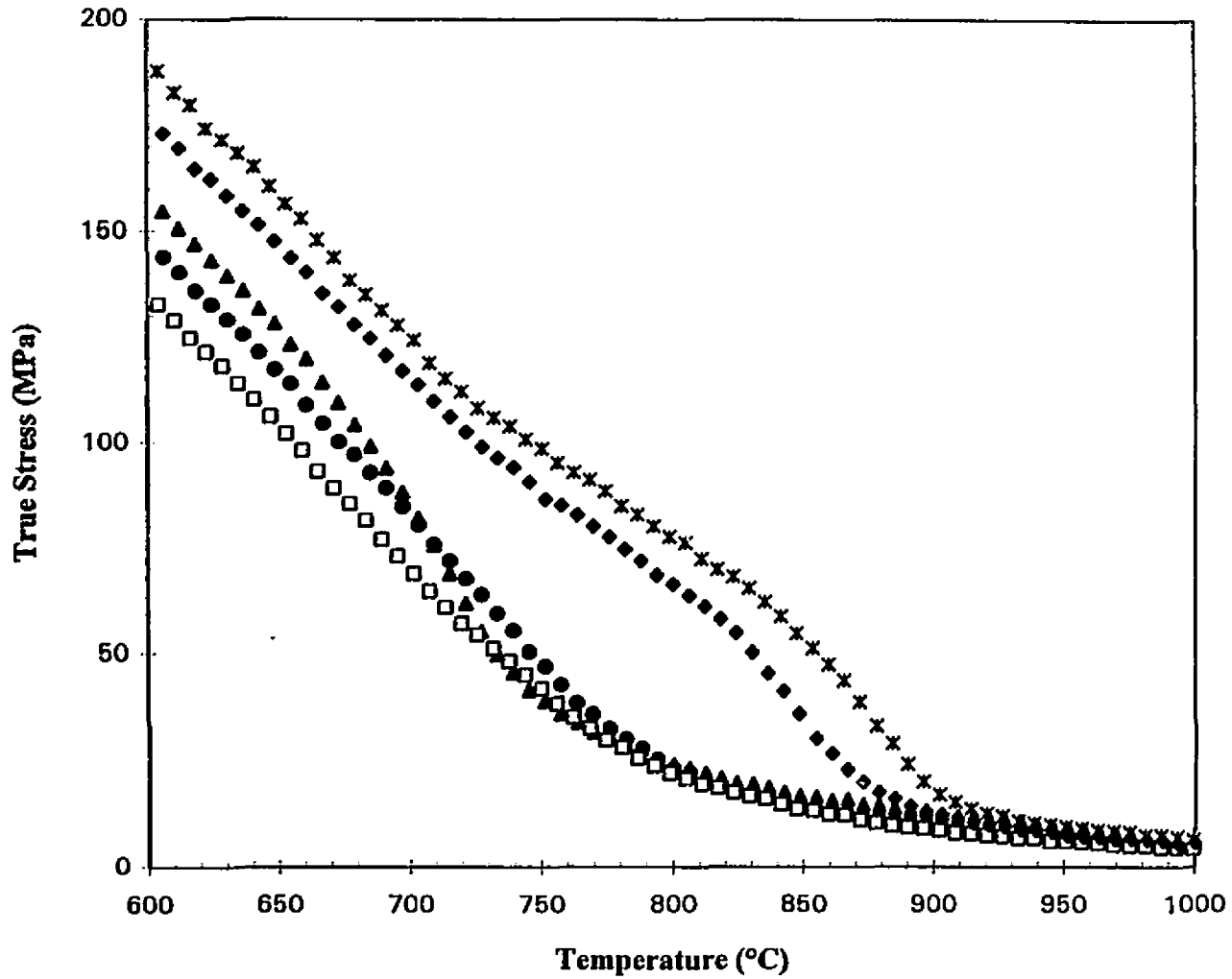


Figure IV-5: True stress vs. temperature for all five steels, 1000-600°C($\dot{\epsilon}=1.8 \times 10^{-4}$), taking contraction effects into account.

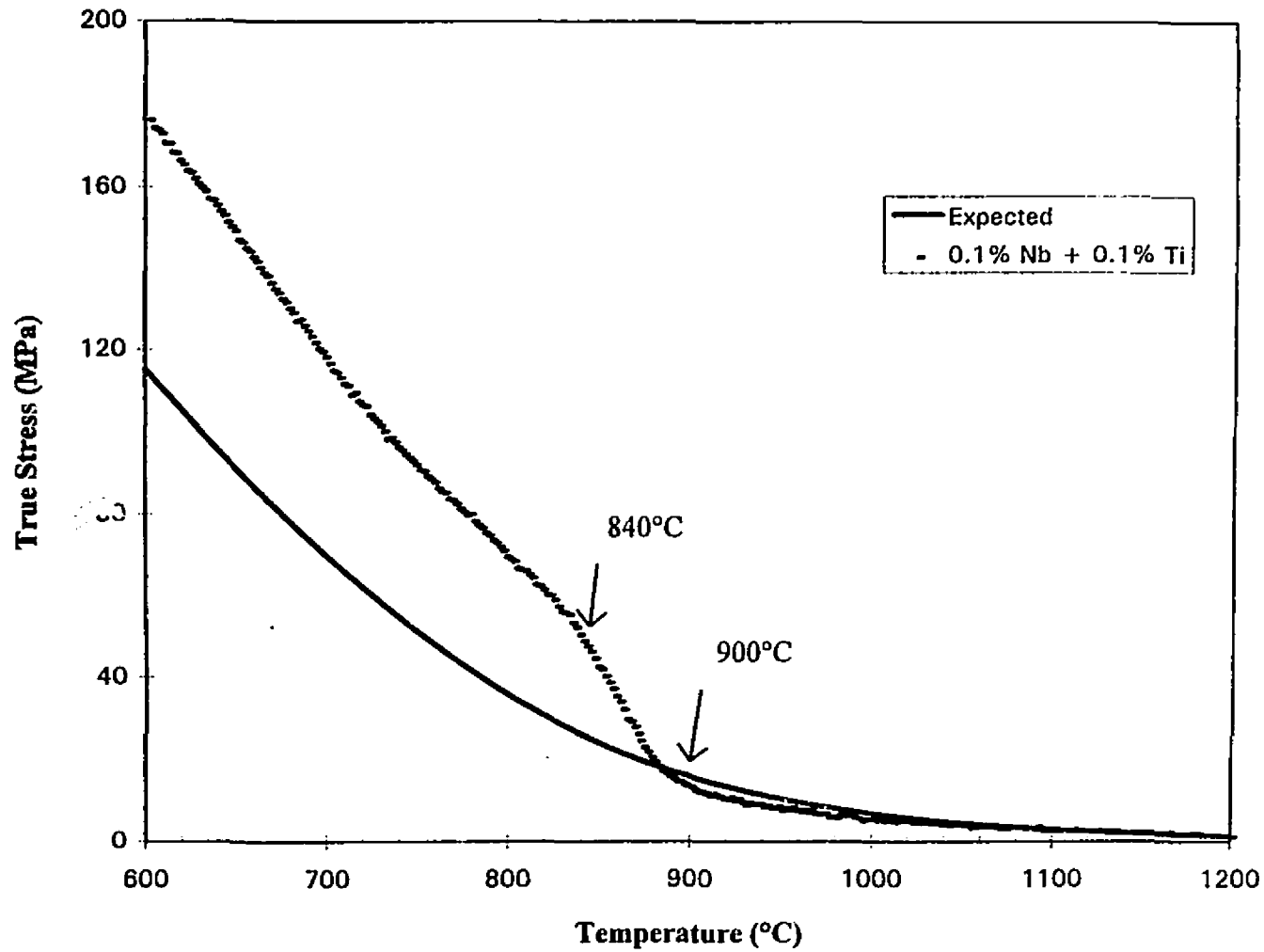


Figure IV-6: Superposition of the expected curve on the actual behaviour of the 0.1% Nb + 0.1% Ti stainless steel; with the starting flow stress of the steady state flow curve corrected to match that of the actual test.

855°C and 840°C, respectively, after which the rate of increase decreases markedly, until slopes similar to those of the other three materials are observed.

(Determination of the temperature of divergence is discussed in Chapter V, section V. 5.1.)

IV. 2.3. High temperature solutionizing schedule

IV. 2.3.1. IF Nb stabilized

A series of CCC tests was performed at higher holding temperatures (1300°C) (i.e. implementing the heating and deformation schedule shown in Figure III-8). Figure IV-7 displays the result of one of these tests for the 0.2% Nb material along with that of the standard CCC test (i.e. begun at a holding temperature of 1200°C). This figure shows that, as a result of increasing the holding temperature and time, the deviation begins at a higher temperature (950°C). Also, the 1300°C curve begins to exhibit lower flow stresses than the 1200°C test at about 860°C.

IV. 2.3.2. IF Ti stabilized

By completely replacing the niobium with titanium (steel D - IF Ti stabilized), it is possible to determine, with the aid of CCC tests, the effects of titanium additions on the high temperature flow stress. Figure IV-8 shows the expected flow curve superimposed on the flow curves of the IF Ti stabilized material obtained from tests initiated at 1200°C and 1300°C (as described in Figures III-7 and III-8). The expected curve closely approximates the two other flow curves, with no appreciable deviations except for the lower flow stresses in the 1300°C case at temperatures below 800°C. This may be due to an initially larger grain size.

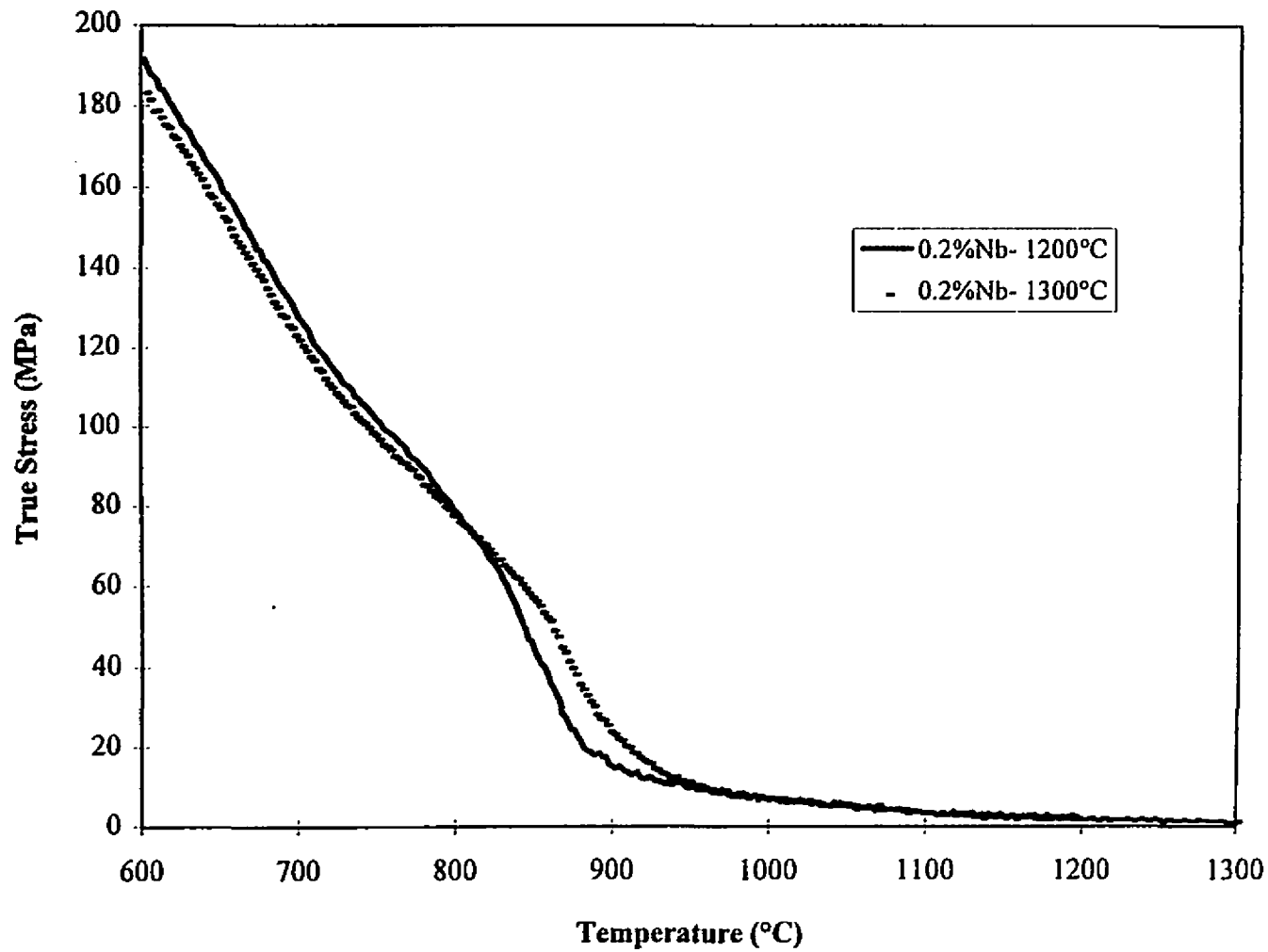


Figure IV-7: True stress vs. temperature for the 0.2% Nb material after holding at different temperatures and times.

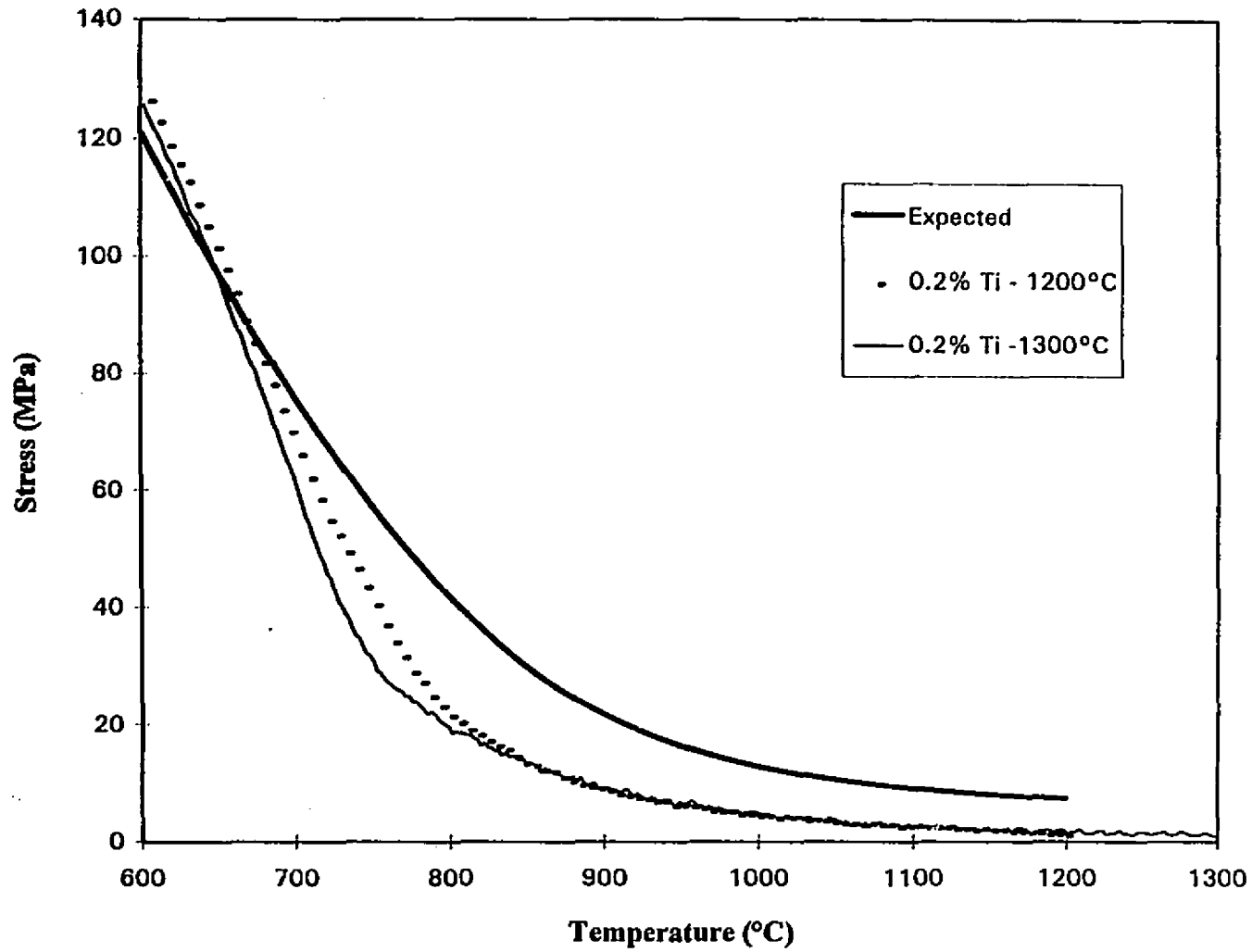


Figure IV-8: True stress vs. temperature for the IF Ti stabilized material after holding at different temperatures and times compared to the standard curve.

IV. 2.4. Low temperature and reduced time solutionizing schedule

IV. 2.4.1. IF Nb stabilized

Another method employed to diminish the amount of niobium in solution was to decrease the holding temperature and/or time. Several tests of this nature were performed with holding times of one minute at temperatures of 1200°C, 1000°C, and 950°C, as outlined in the heating and deformation schedule of Figure III-9. Figure IV-9 shows three curves obtained using this schedule and the standard CCC test (i.e. 1200°C holding temperature for 10 minutes). This figure shows that, by decreasing the holding time and/or decreasing the holding temperature, less niobium is put into solution.

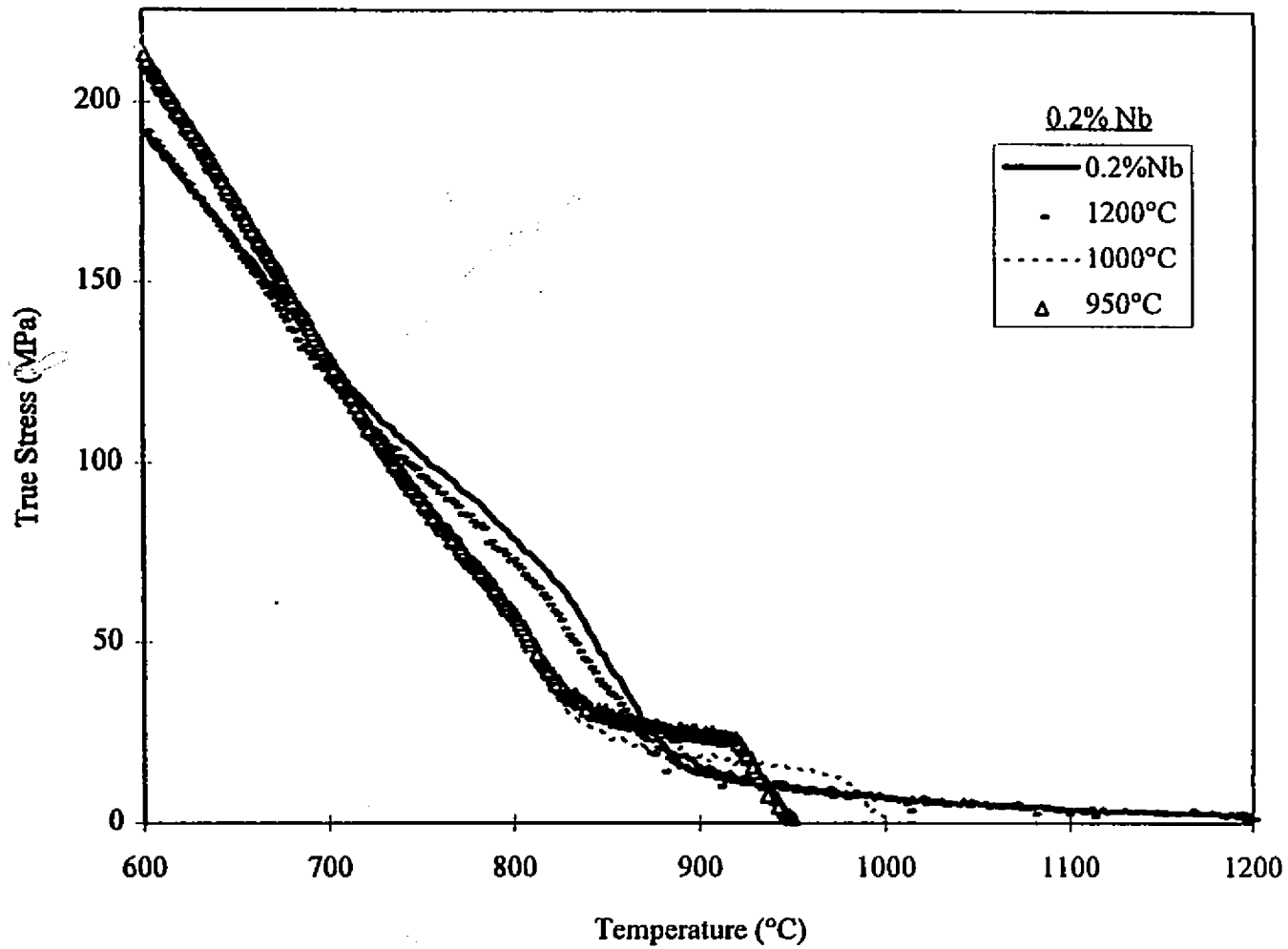


Figure IV-9: True stress vs. temperature for the 0.2% Nb material after holding at different temperatures and times.

CHAPTER V

DISCUSSION

Up to this point there has been no attempt made to explain the flow curve behaviour during CCC testing. More specifically, the inflections or deviations in these curves are of interest here. There are three possible explanations for these deviations: 1) solute drag, 2) phase transformation, and 3) precipitation. The following sections will show why the first two are not responsible and the third one, precipitation, is causing the deviations in the flow curve. Then, the remaining sections describe and show how to produce a continuous cooling precipitation (CCP) diagram. Herein the vast power of this test is illuminated.

V. 1. Solute drag

Alloy additions, such as Nb, Ti and Mo, can inhibit grain growth, and retard recovery and recrystallization during or after hot rolling. Solute drag has also been shown to be an important retarding mechanism. However, there is still some controversy about whether solutes are simply precipitates that are too small to be detected [46, 100]. Solute drag could be dealt with as very very small particles, but there are two main differences based on the effects of diffusion:

- i) Segregation can take place, usually to grain boundaries or dislocations; therefore, small amounts of solute can produce much larger effects.

- ii) Atoms move with the interface:

Chapter V - Discussion

- At low velocities of the interface, atoms can readily keep up with the interface (i.e. they are able to move in this way because of diffusion). Therefore, there is no drag force exerted by these solutes.
- At high velocities, the drag force is again low because the concentration of segregated atoms is low; this is because in this case the grain boundaries are able to move away or escape from the segregated atoms.

However, there is an intermediate speed, which is a function of the interaction energy and the diffusivity, at which solute drag effects are optimized. This is shown in Figure V-1 below. Here, the drag force versus velocity profiles are plotted for various elements in γ -iron [100]. This shows that at low velocities the drag force is minimal; it increases to a maximum with increasing velocity, then starts to decrease once again with further increases in velocity.

In Figure IV-5, it may seem as though the deviations in the flow curves are due to solute drag. If we look at the niobium bearing material, as shown in Figure V-2b, one can suggest that the following is occurring: The first divergence in the flow curve (920°C) is due to the solute drag effect of niobium on the dislocations of the deforming stainless steel. As the strain increases, the temperature decreases, resulting in a decrease in the diffusivity of the niobium in solution. Consequently the solute drag effect is lowered at around 855°C. Thus far, this argument seems valid; however, this hypothesis breaks down when one examines Figure V-2. This figure shows the effect of slowly replacing niobium with an equivalent amount of titanium. Here, there is no obvious "solute drag effect" in the titanium bearing material. However, Figure V-1 above shows that titanium and niobium have similar solute drag effects. Thus an apparent contradiction exists. Therefore, it seems reasonable to conclude that solute drag is not the prevalent mechanism affecting the behaviour observed in these tests.

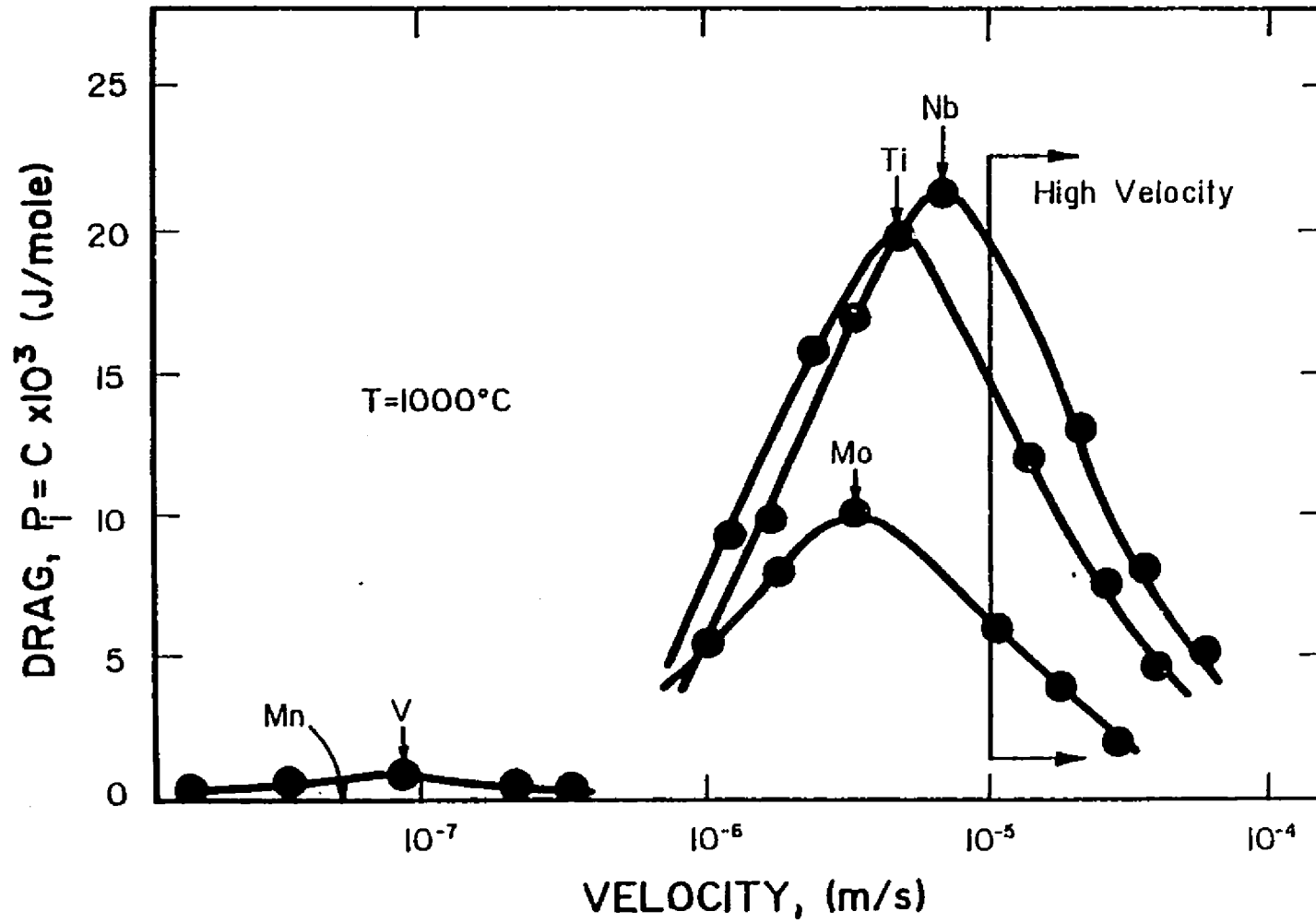


Figure V-1: Drag force vs. velocity profiles for various elements in γ -iron [100].

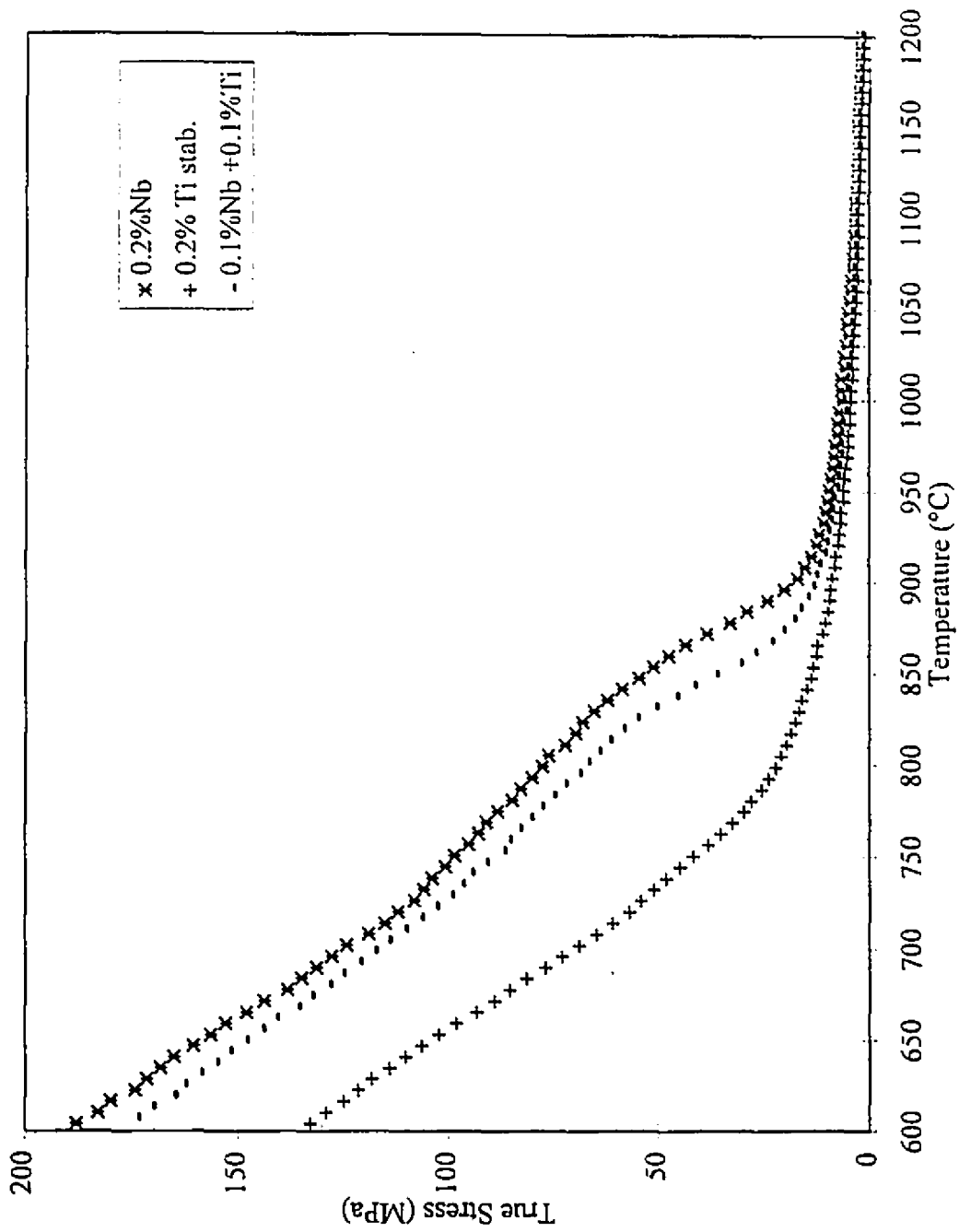


Figure V-2: True stress vs. temperature for the 0.2% Nb, 0.1% Nb + 0.1% Ti, and 0.2% Ti steels, 1200-600°C ($\dot{\epsilon} = 1.8 \times 10^{-1}$).

V.2. Phase transformations

Figure II-1 describes the iron-chromium phase diagram and shows the γ -loop. As explained in the literature review, this γ -loop is the region where austenite or austenite and ferrite are stable. The α to $(\alpha+\gamma)$ binary phase boundary is located in the interval from 13% Cr down to about 10% Cr in the temperature range of interest here. Since, all the steels examined have chromium contents of approximately 11.1%, it would seem possible that, during testing from 1200°C- 600°C, the material could undergo phase transformations. For example, in Figure IV-2b, the first deviation (at 920°C) displayed by the 0.2% Nb material could be caused by the formation of a harder austenite phase, and then upon further cooling this austenite could transform back into ferrite. This could cause a decrease in the flow curve - much like that observed at 855°C.

Before any interpretation based on the chromium content can be made, one must first take into account the chromium equivalent of the other elements. The chromium equivalent (equation 5.1) has been empirically determined using the most common ferrite-forming elements:

$$\text{Cr equivalent} = (\text{Cr}) + 2(\text{Si}) + 1.5(\text{Mo}) + 5.5(\text{Al}) + 1.75(\text{Nb}) + 1.5(\text{Ti}) + 0.75(\text{W}) \quad (5.1)$$

Using this equation, the chromium equivalents of the 0.2% Nb, 0.2% Ti, and the reference material were calculated and determined to be 12.6%, 12.6% and 12.3%, respectively. This means that it is more likely for the reference material than for the other two grades to undergo a phase transformation. The problem now arises when looking at Figure IV-5. Here only the niobium bearing materials show marked deviations in the flow curve, whereas the reference and titanium materials do not appear to undergo any phase transformations. Also, for the 0.2% Nb material, specimens were quenched after each inflection and micrographs of the microstructure were prepared and examined (see Figures V-3, V-4, V-5 and V-6). These micrographs show no evidence of a separate

phase. Therefore, phase transformations are judged not to be responsible for the 'humps and bumps' observed in the flow curves produced by CCC testing.

V.3. Precipitation effects

In stress relaxation [101] and creep [102] tests, the first perceptible divergence from the general flow behaviour has been identified with the beginning of carbonitride precipitation. Similarly, the point at which the flow behaviour returns to the general trend is identified with the completion of precipitation and the start of Ostwald ripening [103]. With this interpretation as a base, all of the flow curves generated can be rationalized. For instance, the first divergence in the flow curve of the 0.2% Nb material (Figure IV-2b - @ 920°C) can be attributed to the nucleation and growth of niobium carbonitrides. These precipitates continue to grow and the nucleation of fresh precipitates also continues between 920°C and 855°C. After cooling below 855°C, Ostwald ripening dominates, resulting in an overall decrease in the rate of increasing flow stress. The same rationale holds for the titanium stabilized material, except here (see Figure IV-8) the nucleation, growth and coarsening of the precipitates occurs at temperatures above 1100°C. Therefore, the precipitates, in their coarsened form, have relatively little or no effect on the flow stress (i.e. the flow stress behaviour is smooth, similar to the 'expected' flow curve).

The ability of precipitates to pin dislocations increases with the precipitate density. In addition, the flux of solute atoms that enables Ostwald ripening (coarsening) to take place increases with the concentration of the species in solution. The above interpretations are confirmed by the careful examination of Figures IV-7 and IV-9. Figure IV-7 shows how increasing the solution temperature and time affects the amount and rate of precipitation and coarsening. Precipitation begins sooner because more niobium is put into solution, which results in a larger driving force for precipitation; this in turn causes precipitation to begin at higher temperatures (i.e. at 950°C instead of

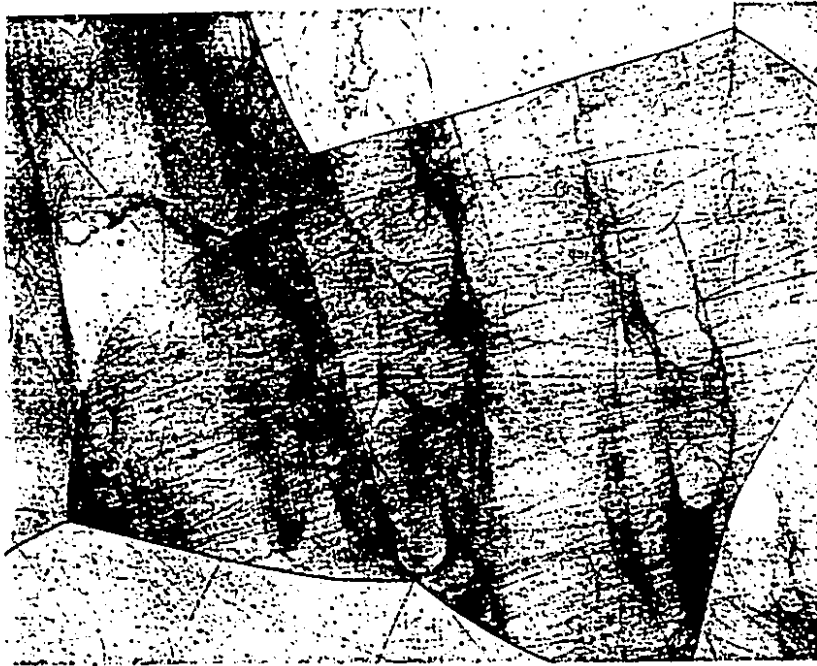


Figure V-3: Microstructure of the 0.2% Nb material after a strain of 0.112 (100X).

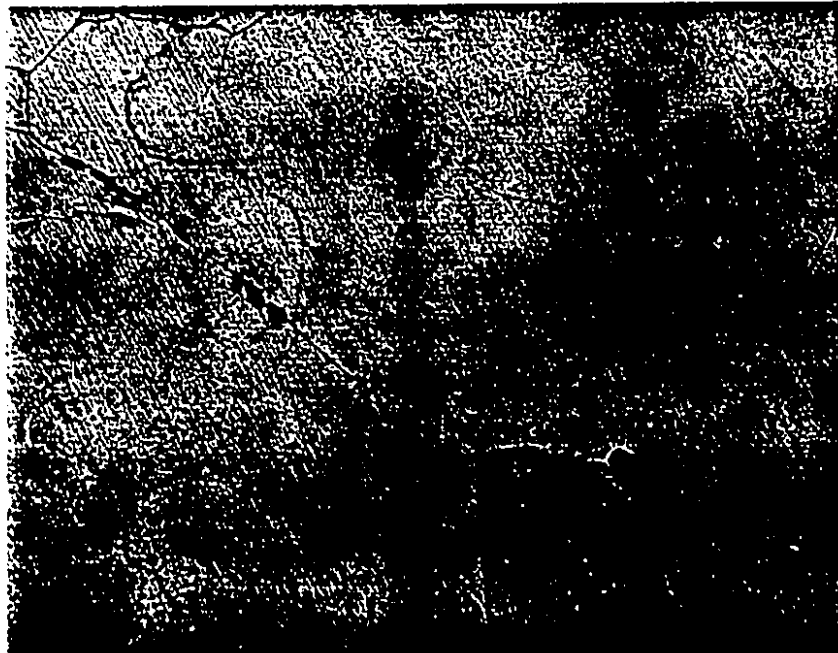


Figure V-4: Microstructure of the 0.2% Nb material after a strain of 0.135 (100X).



Figure V-5: Microstructure of the 0.2% Nb material after a strain of 0.150 (100X).



Figure V-6: Microstructure of the 0.2% Nb material after a strain of 0.185 (100X).

920°C). Note that the 1300°C curve displays lower flow stresses than the 1200°C curve starting at approximately 800°C. This may be due more coarsening of the precipitates. Figure IV-9 was explained in the Results section; two interesting conclusions can now be drawn from this figure in the light of precipitation effects. First, a decrease in only the holding time decreases the amount of niobium put into solution, as shown by the lower precipitation start temperature (900°C) in the 1200°C case when the sample is held for one minute instead of ten. Secondly, a decrease in holding temperature also diminishes the amount of niobium put into solution, again leading to precipitation at much lower temperatures (i.e. 840°C and 835°C for the 1000°C and 950°C tests, respectively).

V. 4. TEM examination

There are two more important procedures that must be performed before one can be unequivocally certain that precipitation is actually occurring and that these precipitates are the cause of the flow hardening; they are: 1) the precipitates must be found, and 2) their size and abundance must be reasonably consistent with the flow hardening observed.

V. 4.1. Thin foils

In order to find the precipitates, specimens had to be quenched at what seemed to be the beginning of precipitation. That is, CCC tests were carried out down to 920°C, after which the specimens were quenched, for both the 0.2% Nb and 0.2% Ti bearing grades of stainless. This enabled the size of the precipitates to be determined and a comparison to be made between the behaviours of the two steels. It should be recalled that the mechanical evidence indicates that the titanium precipitates should be coarse at these temperatures (i.e. 920°C), because the precipitates are nucleated, grow, and coarsen at higher temperatures, and consequently are expected to have little influence on the flow stress.

Thin foils of both materials were prepared, as described in the Experimental Chapter, section III. 4.3. These foils were then examined using a TEM. The results of this examination are shown in Figures V-7 and V-8 below for the 0.2% Nb and 0.2% Ti materials, respectively. These figures are 'bright field images', which are essentially made up of the transmitted beams in the absence of the diffracted beams (i.e. they constitute a direct view of the specimen). The black dots in Figure V-7 are of the precipitates. Careful examination of this and other similar photographs reveals that the particles range in size from a maximum of 10 to 15 nm to as small as 4 nm in diameter. However, there are far more of the finer precipitates. This range of sizes is expected, since nucleation and growth proceed concurrently at this stage. The situation is not quite the same for the 0.2% Ti material, shown in Figure V-8. Here, the larger black dot is representative of the precipitates seen under the TEM. The diameters of these fall between 50 and 70 nm. These precipitates are quite scarce because they are large (i.e. coarsened) and the total volume fraction is small (this is demonstrated in the following section). The results shown here are consistent with the description of the precipitation behaviour presented above.

V. 4.2. Estimation of precipitation strengthening

Up to this point, the precipitates have been identified and considered to be the cause of the flow strengthening. The maximum difference in flow strength between the 0.2% Nb and 0.2% Ti material is approximately 50 MPa. By using the approximate sizes of the precipitates, the chemical compositions of the two grades of stainless and equation (2.9), shown in section II. 5.2. of the Literature Review (and reproduced below for purposes of calculation), the flow strengthening effect of these precipitates can be estimated. The following shows how the volume fraction of the precipitates was calculated.

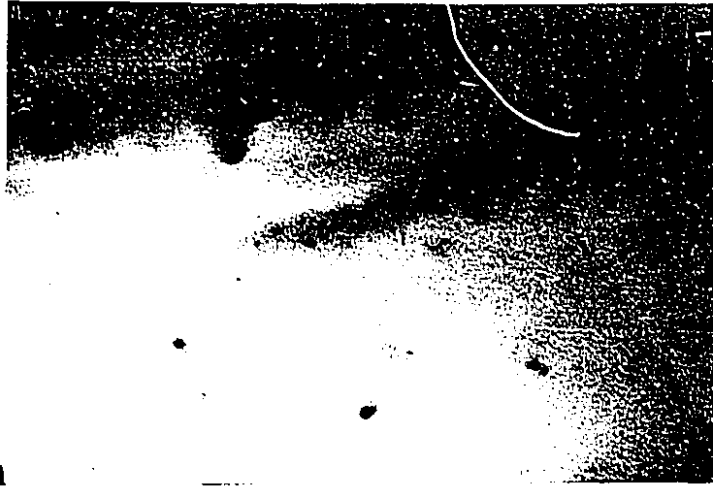


Figure V-7: Bright field image of precipitates in the 0.2% Nb material, quenched at 920°C (100,000 X).

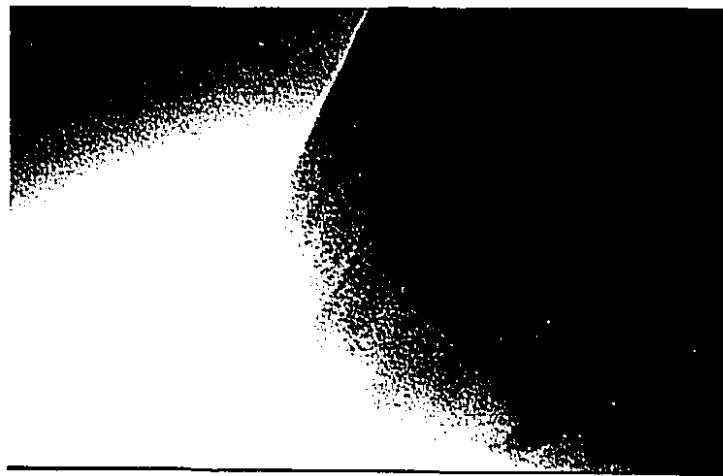


Figure V-8: Bright field image of precipitates in the 0.2% Ti material, quenched at 920°C (100,000 X).

It has been shown that niobium and titanium carbonitrides are both of the fcc NaCl crystal type, with lattice parameters within 2-3% of each other, and 20-25% greater than that of austenite [104]. The lattice parameter of austenite is 0.351 nm, and the volume of one unit cell of a particle is therefore about 0.0795 nm^3 (i.e. $[0.351 \text{ nm} \times 1.225]^3$). There are eight atoms in each cell, four of either Nb or Ti and four of either C or N. Therefore, there is one cell for every four carbon or nitrogen atoms.

In 1000 grams of the niobium containing material (0.003 wt% C and 0.005 wt% N), there are approximately 3.654×10^{21} atoms of carbon plus nitrogen. Assuming all the carbon and nitrogen precipitate, then there will be a total of 9.134×10^{20} unit cells, with a total volume of $7.262 \times 10^{19} \text{ nm}^3$ (i.e., $9.134 \times 10^{20} \times 0.0795 \text{ nm}^3$). Now, the volume of one unit cell of ferrite is 0.0235 nm^3 . Therefore, in 1000 grams of material, there are approximately 1.0783×10^{25} atoms, with 2 atoms per cell, which yields 5.392×10^{24} unit cells. This adds up to a total volume of ferrite equal to $1.267 \times 10^{23} \text{ nm}^3$. By dividing the total volume of precipitates by the total volume of ferrite, and assuming that the total volume of ferrite is approximately equal to the total volume of stainless steel, the volume fraction of precipitates is found. This calculation yields a precipitate volume fraction of 0.00057. Note, this volume fraction is approximately the same as that for the titanium material.

Now equation (2.9) can be solved for various particle sizes. Table V-1 below shows the theoretical strengthening effects of the precipitates. Here we see that the strengthening attributed to fine precipitates (0.2% Nb material) is about 62 MPa greater than that caused by coarse ones (0.2% Ti material), see Table V-1. This difference of 62 MPa is in good agreement with the flow stress difference observed in the CCC tests (i.e. approximately 50 MPa).

$$\sigma(\text{MPa}) = \frac{5.9f_v^{1/2}}{\bar{L}} \ln\left(\frac{\bar{L}}{2.5 \times 10^{-4}}\right) \quad (2.9)$$

Table V-1: Theoretical flow strength increase due to the presence of precipitates.

material	\bar{L} (nm)	σ (MPa)
Nb	4	98
Nb	10	52
Nb	ave. 75 MPa	
Ti	50	15
Ti	70	11
Ti	ave. 13 MPa	

V.5. Continuous Cooling Precipitation (CCP) Curves

From the above results, it appears that the beginning and end of precipitation in the Nb containing grades can be followed by means of CCC testing. As the cooling rate was known precisely in this study (0.5°C/sec), the temperatures associated with the start and maximum extent of divergence can be converted into precipitation start and finish times, respectively. Such times can then be used to construct continuous-cooling-precipitation (CCP) curves, as will be demonstrated in more detail below.

V. 5.1. P_s and P_f determination

First, a criterion must be established for the determination of the precipitation start and finish temperatures. Since the flow curve cannot be precisely expressed by the expected flow curve (as described in the Results, section IV. 2.1.), an alternative standard is proposed here. First, the flow curve is plotted as the log of the true stress versus the temperature (°C). Then linear regressions are performed along the following temperature intervals: 1) the starting temperature (usually 1200°C) and just before the first perceptible point of divergence, 2) the point at which the rate of flow stress increase is constant up to the first indication of flow softening, and finally, 3) between the point at which the rate of flow stress increase is once again constant to the final stress value (i.e. end of test, usually 600°C). The second linear regression line will intersect both the first and third regression lines. The points of intersection are considered to be the precipitation start temperature

(P_s) and precipitation finish temperature (P_f), respectively. Figure V-9 displays the flow curve of the 0.2% Nb material between 1200°C and 600°C with linear regression lines revealing the P_s and P_f times, as described above.

The values obtained from Figure V-9 are used to indicate the P_s and P_f temperatures on the flow curve of true stress versus temperature, as shown in Figure V-10. By comparing the positions of the P_s and P_f temperatures on the flow curves of Figures V-9 (semi-log) and V-10 (linear-linear), it is evident that their positions appear to be shifted to the right. That is, the P_s temperature seems to occur at the first perceptible point of divergence in Figure V-10. The same is true for the P_f temperature. This seems reasonable, inasmuch as precipitation, especially nucleation, is well under way before the flow curve has been noticeably affected. Therefore, it can be concluded that the method described above is reasonably accurate.

V. 5.2. Varying cooling rate schedule for the Nb bearing stainless steels

The second requirement for the construction of a CCP diagram is the availability of further curves, similar to those of Figures IV-3 and IV-4, but determined at other (faster and slower) cooling rates. Examples of such curves, obtained using the heating and deformation schedules shown in Figure III-10, are presented in Figure V-11 for the 0.2% Nb material. The results obtained at 2°C/sec, 1°C/sec and 0.25°C/sec are illustrated here, along with that for the 0.5°C/sec cooling rate. Equivalent results for the 0.1% Nb + 0.1% Ti steel are presented in Figure V-12. For the production of these higher cooling rate flow curves, it was necessary to use slightly higher strain rates in order to counter the effects of contraction (see section IV. 1.2.). However, the effective strain rates are more or less equivalent.

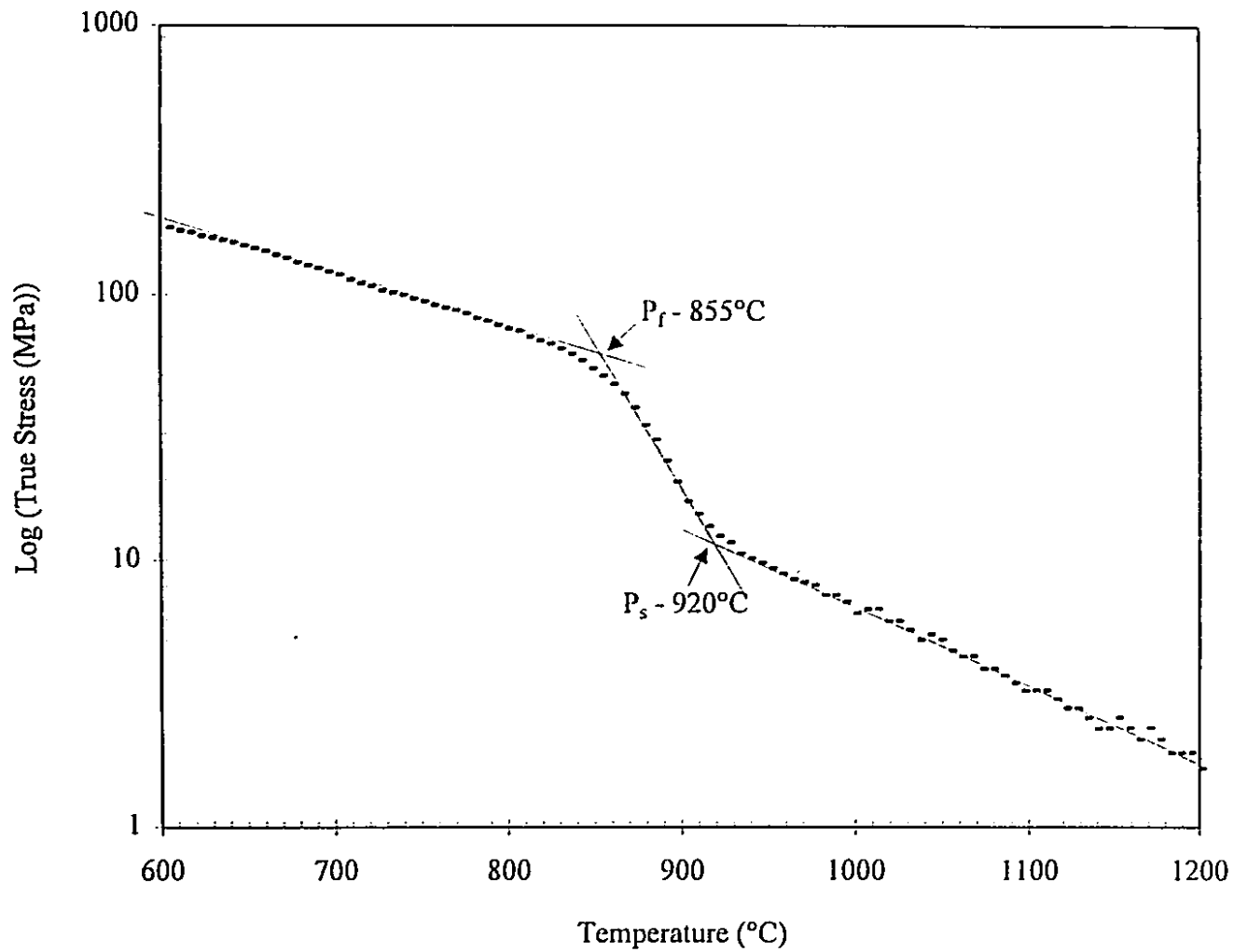


Figure V-9: Log of true stress vs. temperature for the 0.2% Nb stainless steel, with the P_s and P_f temperatures indicated by the present selection criterion ($1200^{\circ}\text{C}-600^{\circ}\text{C}$, $\dot{\epsilon} = 1.8 \times 10^{-4}$).

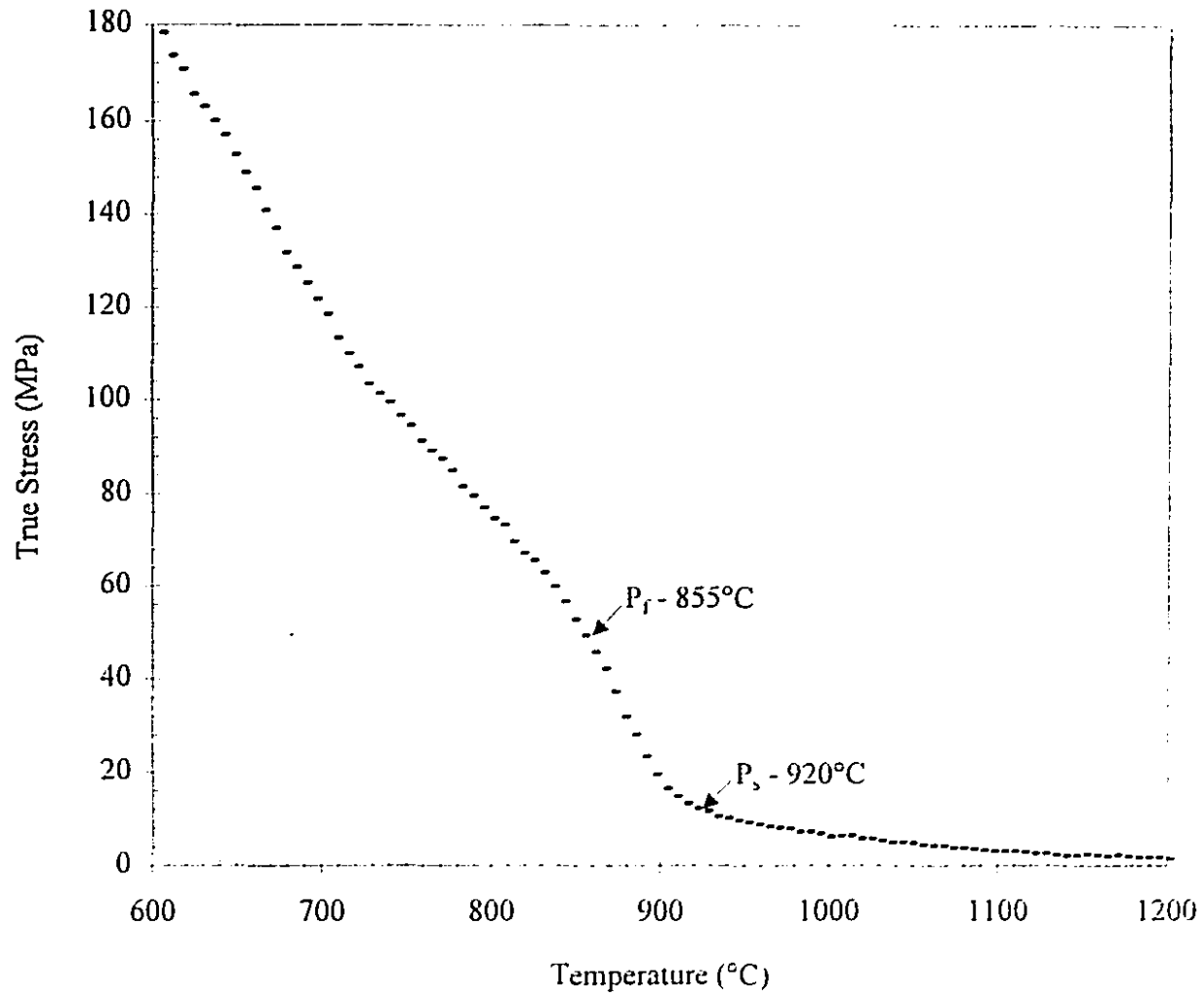


Figure V-10: True stress vs. temperature for the 0.2% Nb material with the P_s and P_f temperatures determined from Figure V-9.

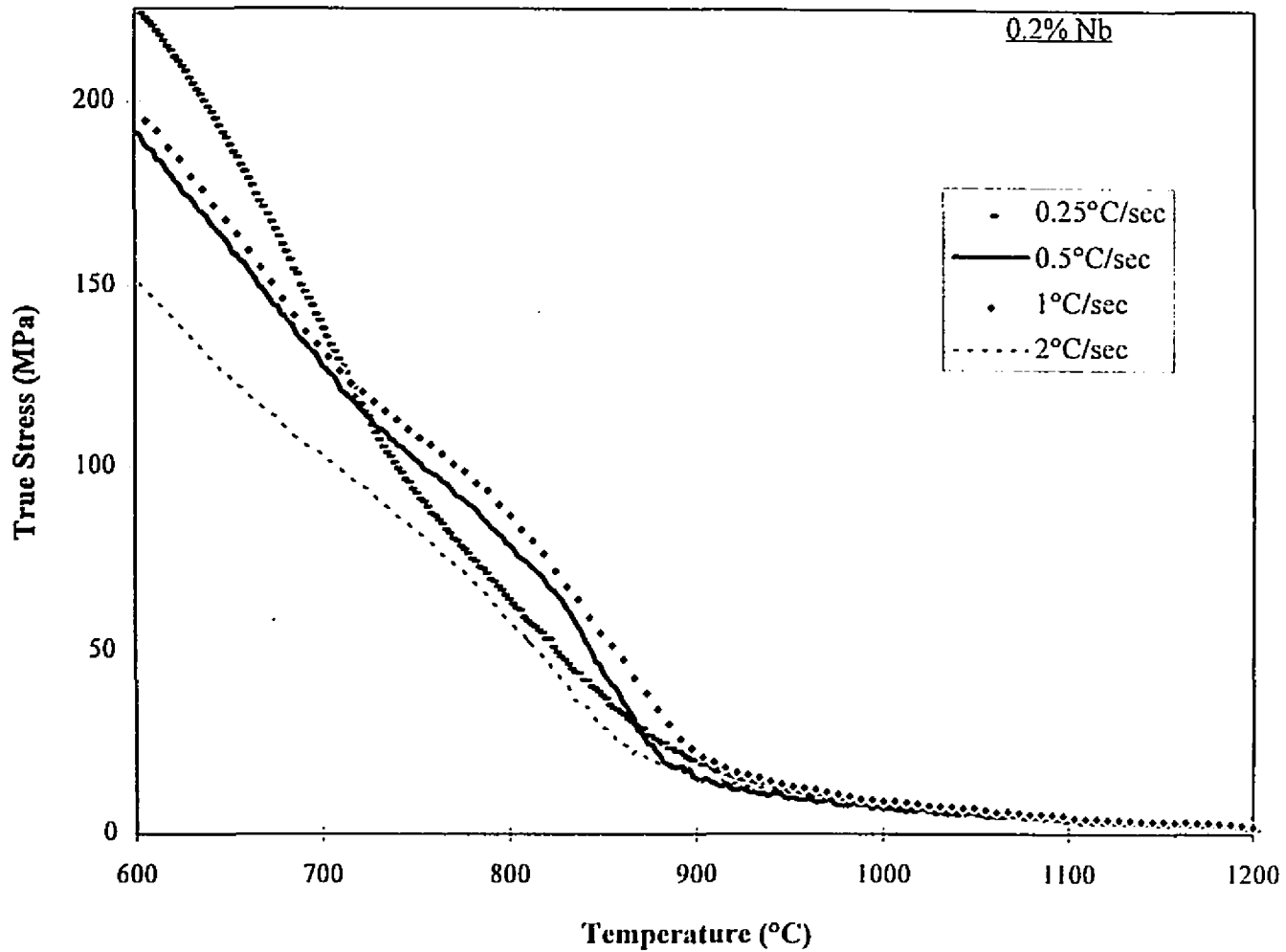


Figure V-11: True stress vs. temperature curves for the 0.2% Nb steel determined using different cooling rates (for 0.25 & 0.5°C/sec, $\dot{\epsilon} = 3 \times 10^{-4}$; for 1 & 2°C/sec, $\dot{\epsilon} = 6 \times 10^{-4}$). Note: after correcting for contraction, all strain rates were approximately 1.8×10^{-4} .

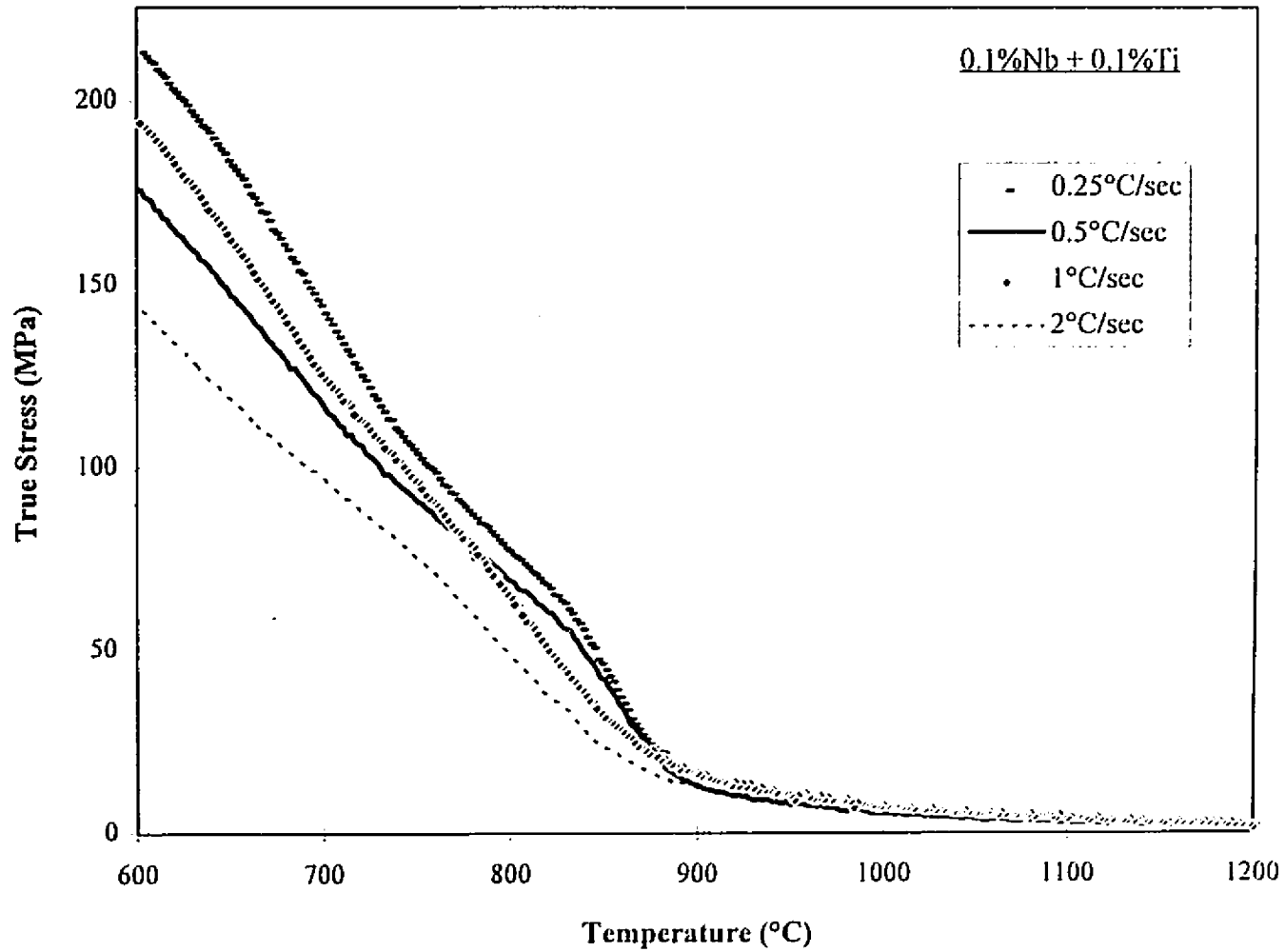


Figure V-12: True stress vs. temperature curves for the 0.1% Nb + 0.1% Ti steel determined using different cooling rates (for 0.25 & 0.5°C/sec, $\dot{\epsilon} = 3 \times 10^{-4}$; for 1 & 2°C/sec, $\dot{\epsilon} = 6 \times 10^{-4}$). Note: after correcting for contraction, all strain rates were approximately 1.8×10^{-4} .

There are several interesting features in both Figures V-11 and V-12; they are:

- 1) The order of the flow curves is not sequential with respect to their cooling rates; in fact, depending on the temperature of interest, the order changes. In Figure V-11 there are three different orders; above approximately 875°C, between 875°C and 740°C, and below 740°C. Similarly, in Figure V-12 there are also three different orders; above 880°C, between 880°C and 790°C, and below 790°C. This is significant inasmuch as it shows that the effect of precipitation is strongest in Figure V-11 (0.2% Nb material) for the flow curves carried out using intermediate cooling rates (0.5°C/sec and 1°C/sec), and it is strongest when employing the slowest cooling rate for the 0.1%Nb + 0.1% Ti material (i.e. Figure V-12), because this condition corresponds to the steepest increase in flow hardening after precipitation.

- 2) Even though, in Figure V-11, precipitation starts earlier in the 0.25°C/sec case, the effects are not as significant. The reason for this is that, at the slowest cooling rate, the material is held for longer periods of time at all temperatures. This translates into the occurrence of more growth and coarsening of the precipitates at the higher temperatures, thereby significantly reducing the strengthening effects of these precipitates. It can be argued that, at this cooling rate, it is impossible to use mathematical methods (such as those described in the previous section) to determine the P_f temperature. Here, this flow curve does not have the same characteristic inflections and deviations that are seen, as a result of the effects of precipitation and coarsening, on the other flow curves. Therefore, it is assumed that the increase in flow stress, for the 0.25°C/sec cooling rate curve, is mainly due to work hardening and the continuous decrease in temperature, as described by the 'expected' flow curve in Figure IV-1. However, some of the primary strengthening is also caused by the initial nucleation and growth of the precipitates. It is for this reason that the P_s temperature can be determined, as will be shown later in this section.

- 3) In Figure V-12, it is apparent that the slowest cooling rate flow curve is, to a large extent, affected by the precipitates. Here, there is a significant decrease in the amount of solute niobium, especially after precipitation is well under way. Thus, it is possible that most of the niobium is in the form of precipitates. Therefore, only at the lower temperatures is the driving force for Ostwald ripening strong enough to actually coarsen the precipitates. Hence, for this flow curve, it is possible to determine the P_f temperature.

- 4) For the 0.2% Nb material, the flow stresses seen for the $1^\circ\text{C}/\text{sec}$ cooling rate are higher than those of the $0.5^\circ\text{C}/\text{sec}$ cooling rate curve, throughout the temperature range. However, above approximately 790°C for the 0.1% Nb + 0.1% Ti material, the flow stresses for the slower cooling rate (0.5°C) are higher than those of the faster $1^\circ\text{C}/\text{sec}$ cooling rate case (see Figure V-12). Below 790°C the flow curves cross, and their behaviour is similar to that seen in Figure V-11. The reason for the initially lower flow stresses can be due to a decrease in the amount of precipitates, because of the lower niobium content. Therefore coarsening is not as severe, with respect to flow stress, when compared to the slower cooling rate of $0.5^\circ\text{C}/\text{sec}$.

- 5) Finally, there is a large difference in stress value between the fastest and slowest cooling rates for both materials. This difference is almost equal in both materials, and it amounts to roughly 100 MPa (see the stress values at 600°C in Figures V-11 and V-12). This can be attributed to the higher accumulated strains developed during the compression test with the slowest cooling rate; it is about 8 times greater (i.e. for the $0.25^\circ\text{C}/\text{sec}$ cooling rate the total strain is ≈ 0.43 , whereas for the fastest cooling rate ($2^\circ\text{C}/\text{sec}$) the total strain is only ≈ 0.06).

The P_s and P_f temperatures for the curves in Figures V-11 and V-12 were determined using the method described in the previous section, and they are given in Table V-2. These P_s and P_f temperatures indicate that, generally, as the cooling rate increases the P_s temperature decreases and the P_f temperature also decreases. This is consistent with the theory of precipitation. That is, as the cooling rate increases, the amount of time spent at any given temperature decreases, thus, effectively causing a supercooling effect. Therefore, precipitation will begin at lower temperatures. This also results in lower Ostwald ripening temperatures.

Table V-2: P_s and P_f temperatures and times, determined from the flow curves of the 0.2% Nb and 0.1% Nb + 0.1% Ti materials, at various cooling rates.

Material	cooling rate (°C/sec)	P_s temperature (°C)	P_f temperature (°C)	P_s time (sec)	P_f time (sec)
0.2% Nb	0.25	930	-*	1080	-*
0.2% Nb	0.50	920	855	560	690
0.2% Nb	1.00	910	835	290	365
0.2% Nb	2.00	885	795	158	203
0.1% Nb + 0.1% Ti	0.25	895	840	1220	1440
0.1% Nb + 0.1% Ti	0.50	900	840	600	720
0.1% Nb + 0.1% Ti	1.00	905	790	295	410
0.1% Nb + 0.1% Ti	2.00	890	780	155	210

* These values could not be determined by the method employed.

As indicated earlier, the respective cooling rates can be employed to convert the P_s and P_f temperatures into P_s and P_f times. These times were calculated by determining the difference between the starting temperature and the temperature of interest (i.e. the P_s or P_f temperature) and then dividing this by the cooling rate. The results are given in Table V-2 for the Nb bearing materials. These times will be used to construct the CCP diagrams for both grades of stainless.

Ultimately, before a CCP curve can be constructed for a specific carbonitride, the solution temperature of the relevant species must be known. This is because the time scale on the diagram only begins when the temperature has dropped below the solution value, so that a driving force for precipitation is generated. This is why the P_s and P_f

times are employed instead of using the P_s and P_f temperatures directly. Unfortunately, the solution temperatures pertaining to the present two Nb - stabilized steels are not known; instead, it is assumed in the construction of the diagram presented below that the same temperature applies to both steels and that this temperature is 1150°C, which is about 100°C above the solution temperature reported for austenite [95].

The P_s and P_f times in Table V-2 have to be corrected, since the first 50°C of these CCC tests are not directly used in the construction of CCP curves. This means that for the 0.25°C/sec cooling rate, the P_s and P_f times are reduced by 200 seconds (i.e. 50°C ÷ 0.25°C/sec), and similar reductions were calculated for the higher cooling rates. Table V-3 below, shows the actual P_s and P_f times used for the construction of CCP curves.

Table V-3: Corrected P_s and P_f times, used for the construction of CCP curves.

Material	cooling rate (°C/sec)	P_s time (sec)	P_f time (sec)
0.2% Nb	0.25	880	-*
0.2% Nb	0.50	460	590
0.2% Nb	1.00	240	315
0.2% Nb	2.00	133	178
0.1% Nb + 0.1% Ti	0.25	1020	1240
0.1% Nb + 0.1% Ti	0.50	500	620
0.1% Nb + 0.1% Ti	1.00	245	360
0.1% Nb + 0.1% Ti	2.00	130	185

* This value could not be determined by the method employed.

The P_s and P_f times obtained in this way were used to construct the CCP diagram of Figure V-13. The curves for the 0.2% Nb and 0.1% Nb + 0.1% Ti materials are of conventional shape, although clearly more points are required to define the locations of the noses of the curves. As a result, only the approximate positions and shapes of the CCC - curves are known for these cases. However, since the points for the 0.1% Nb + 0.1% Ti material are lower than those for the 0.2% Nb material, in agreement with the lower Nb levels, they help to verify the interpretation of the CCC results.

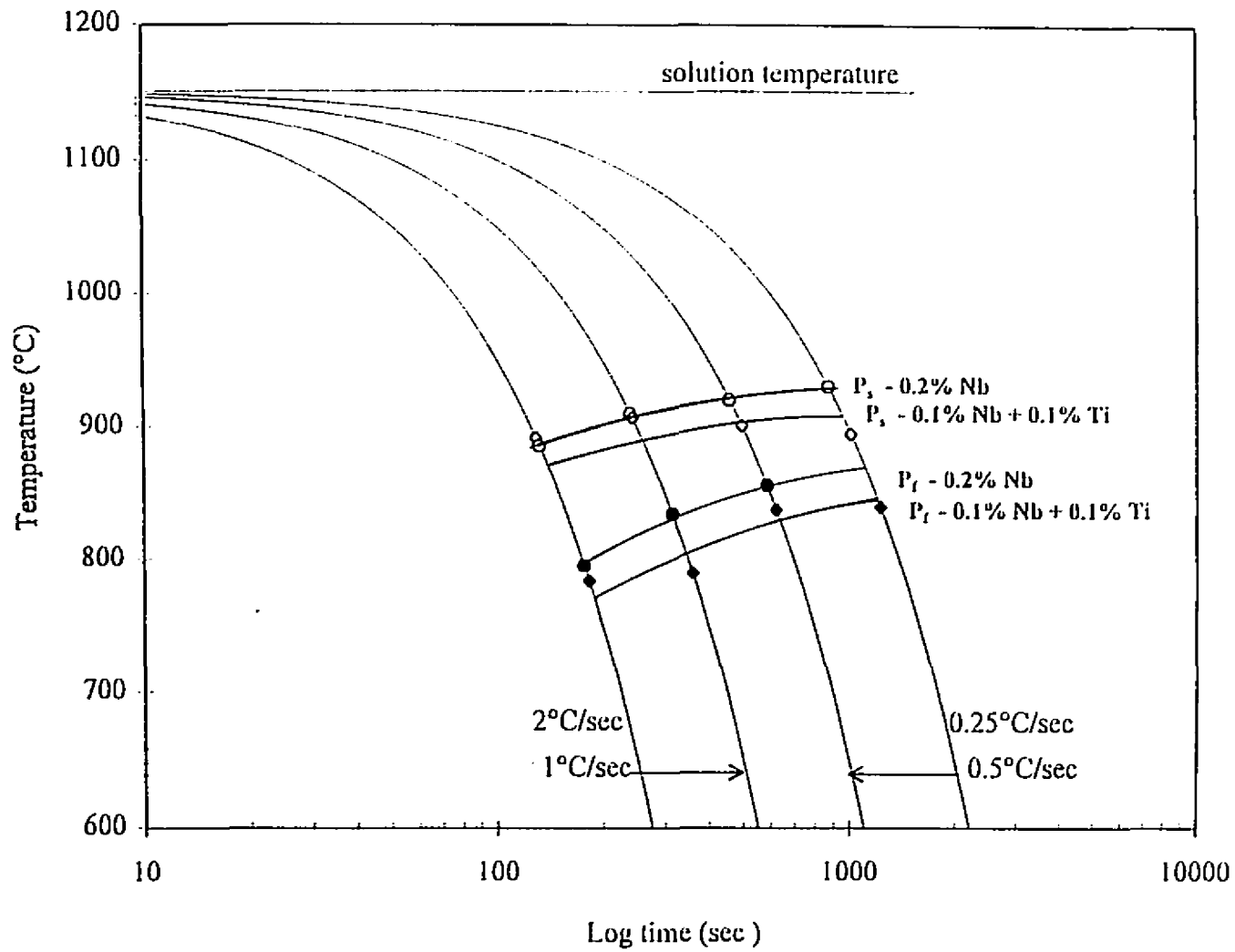


Figure V-13: CCP curves for the 0.2% Nb and 0.1% Nb + 0.1% Ti stainless steels.

CHAPTER VI

CONCLUSIONS

The work presented in this thesis illustrates that strain induced precipitation can be detected in 409 ferritic IF stainless steels under continuous cooling conditions by means of the newly developed continuous cooling compression (CCC) technique. The following conclusions can be drawn from the results presented in this research study:

1. Solute drag, from either niobium or titanium, is not the prevalent mechanism affecting the behaviour observed in these CCC tests. Similarly, phase transformations are not responsible for the 'humps and bumps' observed in the flow curves. These conclusions are supported by the observation that the behaviour of the titanium bearing material diverges from that of the niobium bearing material over the present range.
2. Deviations from the 'expected' flow behaviour in continuous-cooling-compression (CCC) curves can be used to indicate the precipitation start (P_s) and finish (P_f) temperatures. These temperatures can in turn be converted into precipitation start (P_s) and finish (P_f) times.
3. Increasing the solution temperature and time directly affects the amount and rate of precipitation and coarsening. Precipitation begins sooner because more niobium is put into solution, resulting in a larger driving force for precipitation. Also, the precipitates are coarsened to a greater extent.
4. A decrease in holding time decreases the amount of niobium put into solution. This is shown by the lower precipitation start temperature (i.e. 900°C instead of 920°C).

Chapter VI - Conclusions

Similarly, a decrease in holding temperature also diminishes the amount of niobium put into solution, which leads to the initiation of precipitation at much lower temperatures (i.e. 835°C instead of 900°C, for the same holding time).

5. The flow curves for the 0.25%Ti material show no indication of precipitation. However, the TEM results for this material reveal the presence of coarsened precipitates. It therefore appears that the nucleation, growth and coarsening of these particles occur at elevated temperatures (above 1100°C), which is why they have no effect on the flow stress.
6. The precipitates detected by means of TEM examination in the 0.2% Nb stainless steel were small enough to account for the observed increase in flow stress, as calculated from the strengthening effect of the precipitates on the CCC flow stress.
7. The P_s times, for the 0.2% Nb and 0.1% Nb + 0.1% Ti stainless steels, increase with decreasing cooling rate. The same trend applies to the P_f times in these materials.
8. Continuous-cooling-precipitation (CCP) curves can be constructed with the aid of the precipitation start and finish times determined by CCC testing at a series of cooling rates.
9. Niobium, as a stabilizing element in ferritic stainless steels, has a stronger influence on increasing the flow stress than an equivalent amount of titanium.

REFERENCES

- [1] R.A. Lula, "Stainless Steel," ASM, Metals Park, Ohio, 1986.
- [2] R.A. Lula, "Source Book on the Ferritic Stainless Steels," ASM, Metals Park, Ohio, 1982, pp. ix-xii.
- [3] J.J. Demo, "Structure, Constitution, and General Characteristics of Wrought Ferritic Stainless Steels," ASTM STP 619, 1977.
- [4] E.B. Lecken, W.A. Fischer and K. Lorenz, *Stahl und Eisen*, Vol. 81, No. 12, 1961, pp. 768-778.
- [5] L. Colombier and J. Hochmann, "Stainless and Heat-Resisting Steels," Edward Arnold Ltd. Publishers, London, England, 1967.
- [6] A.E. Nehrenberg and P. Lillys, *Transactions, ASM*, Vol. 18, No. 46, 1954, pp. 1177-1213.
- [7] H.D. Newell, *Metal Progress*, Vol. 8, April 1947, pp. 617-626.
- [8] H. Thielsch, *Welding Journal, Research Supplement*, Vol. 30, 1951, pp. 41-47.
- [9] A.J. Cook and F.W. Jones, *Journal of the Iron and Steel Institute*, No. 148, 1943, pp. 217-223.
- [10] P. Chevenard, "Travaux et Memoires Du Bureau International Des Poids et Mesures," Vol. 17, 1927, p. 90.
- [11] E.C. Bain and W.E. Griffiths, *Transactions of the American Institute of Mining and Metallurgical Engineering*, Vol. 75, 1927, pp. 166-213.
- [12] A.G.H. Anderson and E.R. Jette, *Transactions, ASM*, Vol. 24, 1936, pp. 375-419.
- [13] E.R. Jette and F. Foote, "Metals and Alloys," Vol. 7, 1936, pp. 207-210.
- [14] F.J. Shortslee and M.E. Nicholson, *Transactions, ASM*, Vol. 43, 1951, pp. 142-156.
- [15] J.J. Heger, *Metal Progress*, Vol. 49, 1946, p. 976B.
- [16] Z.E. Olzak, "The Effects of Alloy Composition on Sigma Phase Precipitation in 27% Chromium-Iron Catalyst Tubes, First Step Dehydrogenation, Plains Plant," Report No. PR-4-2, The Babcock and Wilcox Tube Co., 25 Aug. 1944.
- [17] J.J. Heger, "Symposium on the Nature, Occurrence, and Effects of Sigma Phase," ASTM STP 110, 1951, pp. 75-78.
- [18] J.J. Gilman, *Transactions, ASM*, 1951, pp. 101-187.

- References -

- [19] C.A. Zapffe and C.O. Worden, *Welding Journal*, Research Supplement, Vol. 30, 1951, pp. 47s-54s.
- [20] H.D. Newell, *Metal Progress*, Vol. 12, May 1946, pp. 977-1028.
- [21] R.M. Fisher, E.J. Dulis and K.G. Carroll, *Transactions, American Institute of Mining, Metallurgical, and Petroleum Engineers*, No. 185, 1957, pp. 358-374.
- [22] R.O. Williams, *Transactions, Metallurgical Society of the American Institute of Mining, Metallurgical, and Petroleum Engineers*, No. 212, 1958, pp. 497-502.
- [23] F.M. Becket, *Transactions, American Institute of Mining, Metallurgical, and Petroleum Engineers*, No. 131, 1938, pp. 15-36.
- [24] G. Bandel and W. Tofaute, *Archiv fur das Eisenhüttenwesen*, Vol. 15, No. 7, 1941-1942, pp. 307-319.
- [25] J.J. Heger, *Metal Progress*, Vol. 8, Aug. 1951, pp. 55-61.
- [26] P.J. Grobner, *Metallurgical Transactions*, Vol. 4, 1973, pp. 251-260.
- [27] J.J. Demo, "Effects of High Temperature Exposure on the Corrosion Resistance and Ductility of AISI 446 Stainless Steel," *NACE Preprint No. 23*, 1968 Conference, Cleveland, National Association of Corrosion Engineers, 1968.
- [28] M. Semchyshen, A.P. Bond and H.J. Dundas, "Toward Improved Ductility and Toughness," Kyoto, Japan, 1971, pp. 239-253.
- [29] A. Plumtree and R. Gullberg, *Journal of Testing and Evaluation*, Vol. 2, No. 5, 1974, pp. 331-336.
- [30] P.A., Bond, *Transactions, Metallurgical Society of the American Institute of Mining, Metallurgical, and Petroleum Engineers*, No. 245, 1969, pp. 2127-2134.
- [31] J.J. Demo, *Transactions, Metallurgical Society of the American Institute of Mining, Metallurgical, and Petroleum Engineers*, Vol. 5, 1974, pp. 2253-2256.
- [32] J. Hochmann, *Comptes Rendus*, Vol. 31, No. 226, 1948, pp. 2150-2151.
- [33] R.J. Hodges, *Corrosion*, Vol. 27, 1971, pp. 164-167.
- [34] R.J. Hodges, *Corrosion*, Vol. 27, 1971, pp. 19-127.
- [35] M.A. Streicher, *Corrosion*, Vol. 29, 1973, pp. 337-360.
- [36] W.O. Binder and H.R. Spindelow, *Transactions, ASM*, Vol. 43, 1951, pp. 759-777.
- [37] A. Baumel, *Stahl und Eisen*, Vol. 84, 1964, pp. 798-802.
- [38] A.P. Bond and E.A. Lizlove, *Journal of the Electrochemical Society*, Vol. 38, No. 116, 1969, pp. 1305-1311.

- References -

- [39] J.J. Demo, "Ferritic Iron-Chromium Alloys," Canadian Patent No. 939,936, 15 Jan. 1974.
- [40] J.J. Demo, "Ductile Chromium-Containing Ferritic Alloy," Canadian Patent No. 952.741, 13 Aug. 1974; patent applied for in the United States.
- [41] R.A. Lula, A.J. Lena and G.C. Kiefer, Transactions, ASM, Vol. 46, 1954, pp. 197-230.
- [42] G. Hersleb, Werkstoffe und Korrosion, Vol. 50, Oct. 1971, pp. 434s-440s.
- [43] R.D. Cowling and H.E. Hintermann, Journal of the Electrochemical Society, Vol. 117, No. 11, 1970, pp. 1447-1449.
- [44] R.N. Wright, Welding Journal, Research Supplement, Vol. 50, Oct. 1971, pp. 434s-440s.
- [45] D.J. Sipos, R.F. Steigerwald and N.E. Whitcomb, "Ductile Corrosion-Resistant Ferrous Alloys Containing Chromium," U.S. Patent No. 3 672 876, 27 June 1972.
- [46] I. Tamura, C. Ouchi, T. Tanaka and H. Sekine, "Thermomechanical Processing of High Strength Low Alloy Steels," Butterworth & Co., 1988.
- [47] W.P. Sun, M. Militzer, D.Q. Bai and J.J. Jonas, "Effects of Interpass Time on Austenite Recrystallization in Nb-Containing HSLA Steels," Recrystallization '92, International Conference on Recrystallization and Related Phenomena, San Sebastian, Spain, September 1992, Material Science Forum, 113-115, (1993), pp. 533-538.
- [48] W.P. Sun, M. Militzer, D.Q. Bai and J.J. Jonas, "Measurement and Modelling of the Effects of Precipitation on Recrystallization under Multipass Deformation Conditions," Pergamon Press Ltd., Acta metall. mater. Vol. 41, No. 12, 1993 pp. 3595-3604.
- [49] W.P. Sun, M. Militzer, J.J. Jonas and E.B. Hawbolt, "Influence of Cooling Rate on Recrystallization and Precipitation during Hot Rolling," 35th Mechanical Working and Steel Making Conference, Pittsburgh, PA, Oct 1993.
- [50] W.J. Liu and J.J. Jonas, "Ti(CN) Precipitation in Microalloyed Austenite during Stress Relaxation," Metallurgical Transactions, Vol. 19A, June 1988, pp. 1415-1424.
- [51] J.J. Jonas, "Dynamic Recrystallization - Scientific Curiosity or Industrial Tool?" Cape Town, 1994, Material Science and engineering, in press.
- [52] C. J. Novak, "Structure and Constitution of Wrought Austenitic Stainless Steels," McGraw Hill, 1977.

- References -

- [53] H.J. McQueen and J.J. Jonas. "Recovery and Recrystallization during High Temperature Deformation," Academic Press Inc., New York, Vol. 6, 1975, pp. 394-457.
- [54] H. Thielsch. "Physical and Welding Metallurgy of Chromium Stainless Steels," American Welding Society, May 1951, pp. 209s-250s.
- [55] A. Najafi-Zadeh, J.J. Jonas and S. Yue, Metallurgical Transactions, 22A, 1991, pp. 2947.
- [56] J.W. Christian, "The Theory of Transformations in Metals and Alloys," Van Nostrand Reinhold (UK), Co. Ltd, 1981, pp.263.
- [57] D.A. Porter and K.E. Easterling, "Phase Transformations in Metals and Alloys," Van Nostrand Reinhold (UK), Co. Ltd, 1983, pp.263.
- [58] R.E. Reed-Hill, "Physical Metallurgy Principles," PWS-KENT, Boston, Massachusetts, 1973.
- [59] G.A. Chadwick, "Metallography of Phase Transformations," Butterworth & Co Ltd., 1972.
- [60] W.P. Sun, M. Militzer and J.J. Jonas, " Diffusion-Controlled Growth and Coarsening of MnS during Hot Deformation," Metall. Trans., Vol. 23A, Nov. 1992, pp. 3013-3023.
- [61] W.P. Sun, M. Militzer and J.J. Jonas, "Strain-Induced Nucleation of MnS in Electrical Steels," Metall. Trans., Vol. 23A, March 1992, pp. 821-830.
- [62] W.P. Sun, J.J. Jonas, E.B. Hawbolt, I.V. Samarasekera, J. K. Brimacombe and S. Yue, " Mechanical and Microstructural Analyses of Precipitation and Recrystallization during the Hot Forming of Steels," (Review Paper) Proc. TMS Symposium on "Advances in Hot Deformation Textures and Microstructures", the Minerals, Metals & Materials Society, 1994, eds. J.J. Jonas, T.R. Bieler and K.J. Bowman, Oct 1993, Pittsburgh, PA, pp. 1-26.
- [63] T. Gladman, D. Dulicu and I.D. McIvor, "Microalloying 75," ed. M. Korchynski, Union Carbide Corp., New York, 1977, p. 32.
- [64] I.M. Lifshitz and V.V. Slyozov, J. Phys. Chem. Solids, Vol. 19, 1961, pp. 35-50.
- [65] Y. F. Han, P. Dep and M.C. Chaturvedi, Met. Sci., Vol, 19, 1982, pp. 555-561.
- [66] H.O.K. Kirchner, Metallurgical Transactions, Vol, 2, 1971, pp. 2861-2864.
- [67] I. Pontikakos and H. Jones, Met. Sci., Vol. 16, 1982, pp. 27-30.
- [68] A.J. Ardell, Acta Metall., Vol. 20, 1972, pp. 601-609.
- [69] M. Kreye, Z. Metallkd., Vol. 61, 1970, p. 108.

- References -

- [70] M.G. Akben, I. Weiss and J.J. Jonas, *Acta Metall.*, 29, 1981, p. 111.
- [71] I. Weiss and J.J. Jonas, *Metall. Trans.*, Vol. 10A, 1979, p. 831.
- [72] B. Dutta and C.M. Sellars, *Mater. Sci. Tech.*, Vol. 3, 1987, p. 197.
- [73] A. Le Bon, J. Rofes-Vernis and C. Rossard, *Met. Sci.*, 1975, p. 36.
- [74] C.M. Sellars, "Creep Strength in Steel and High Temperature Alloys," *Conf. Proc.*, University of Sheffield, Sept. 1972, p. 20.
- [75] W.J. Liu, Ph.D Thesis, McGill University, Montreal, 1987.
- [76] W.P. Sun, Ph.D Thesis, McGill University, Montreal, 1991.
- [77] W.P. Sun, M. Militzer and J.J. Jonas, *Canadian Metall. Q.*, 1993.
- [78] J.J. Jonas and I. Weiss, *Met. Sci.*, Vol. 13, 1979, p. 238.
- [79] S. Yamamoto, C. Ouchi and T. Osuka, "Thermomechanical Processing of Microalloyed Austenite," *AIME*, Warrendale Pa., 1982, p. 613.
- [80] J.J. Jonas and M.G. Akben, *Metals Forum*, Vol. 4, 1981, p. 92.
- [81] H. Watanabe, Y.E. Smith and R.D. Pehlke, "The Hot Deformation of Austenite," *AIME*, New York, 1977, p. 140.
- [82] M.G. Akben, T. Chandra, P. Plassiard and J.J. Jonas, *Acta Metall.*, Vol. 32, 1984, p. 591.
- [83] B. Bacroix, M.G. Akben and J.J. Jonas, "Thermomechanical Processing of Microalloyed Austenite," *AIME*, Warrendale Pa., 1982, p. 293.
- [84] G.L. Wang and M.G. Akben, "HSLA Steels," *TMS*, Warrendale, Pa., 1988, p. 79.
- [85] W.J. Liu and J.J. Jonas, *Metall. Trans.*, Vol. 20A, 1989, p. 689.
- [86] S.H. Park, Ph.D Thesis, McGill University, May 1991.
- [87] K.C. Russell, "Advances in Colloid And Interface Science," 1980, p. 205.
- [88] E. Scheil, *Arch. Eisenhüttenwes.*, Vol. 12, 1935, p.565.
- [89] M. Umemoto, K. Horiuchi and I. Tamura, *Iron Steel Inst. Jpn.*, Vol 22, 1982, 854.
- [90] M. Umemoto, N. Nishioka and I. Tamura, *Iron Steel Inst. Jpn.*, Vol 22, 1982, 629.
- [91] M. Umemoto, K. Horiuchi and I. Tamura, *Iron Steel Inst. Jpn.*, Vol 23, 1982, 690.
- [92] M. Umemoto, N. Nishioka and I. Tamura, 3rd Int. Cong. on Heat Treatment of Mater., *TMS*, Shanghai, 1983, p. 5.35.
- [93] M. Umemoto, Z.H. Guo and I. Tamura, *Mater. Sci. Technol.*, Vol. 3, 1987, p. 249.

- References -

- [94] H. Ohtsuka, M. Umemoto and I. Tamura, *Tetsu-to-Hagané*, Vol. 73, 1987, p. 144.
- [95] A. Rohatgi, Master of Engineering Thesis, McGill University, Montreal, Canada, 1992.
- [96] A. Zarei Hanzaki, R. Pandi, P.D. Hodgson, and S. Yue, "Continuous Cooling Deformation of Steels," *Metall. Trans.*, Vol 24A, 1993, pp. 2657-2665.
- [97] V. Voort, "Metallography Principles and Practice," McGraw-Hill Book Company, 1984, pp. 647-649.
- [98] G.E. Dieter, "Mechanical Metallurgy," Third Edition, McGraw Hill Book Company, 1986, 306.
- [99] E. Evangelista, P. Mengucci, J. Bowels and H.J. McQueen, "Grain and Subgrain Structures Developed by Hot Working in As-Cast 434 Stainless Steel," The Strength of Metals and Alloys, Haifa, Isreal, 1991.
- [100] L.T. Mavropoulos and J.J. Jonas, "Retardation of Austenite Recrystallization by the Strain induced Segregation of Boron," Canadian Metallurgical Quarterly, Vol. 28, No. 2, 1989, pp. 159-169.
- [101] W.J. Liu and J.J. Jonas, "A Stress Relaxation Method for Following Carbonitride Precipitation in Austenite at Hot Working Temperatures," Metall. Trans., Vol 19A, 1988, 1403-1413.
- [102] W.P. Sun, W.J. Liu and J.J. Jonas, "A Creep Technique for Monitoring MnS Precipitation in Si Steels," Metall. Trans., Vol 20A, 1989, 1989-2707.
- [103] W.J. Liu and J.J. Jonas (1988), "Ti(CN) Precipitation in Microalloyed Austenite During Stress Relaxation," Metall. Trans., Vol 19A, 1988, 1415 - 1424.
- [104] R.W.K. Honeycombe, "Steels: Microstructure and Properties," Edward Arnold (Publishers) Ltd., 1982, pp. 211-235.